Interaction of the H_2 molecule with carbon nanostructures: A DFT study

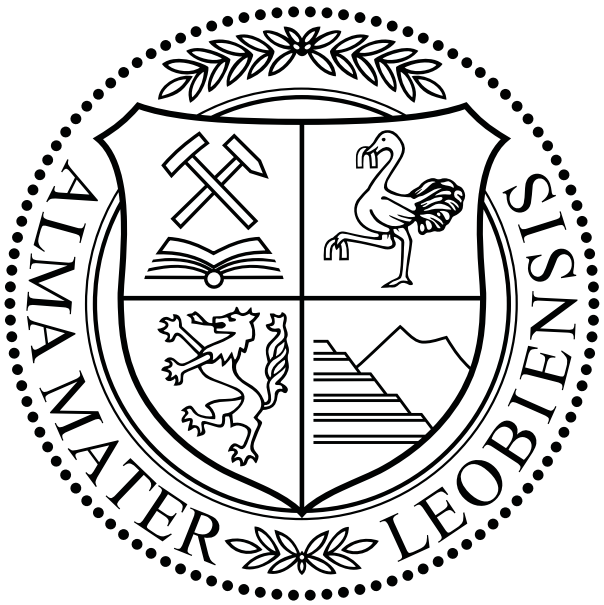

MASTER THESIS

submitted by

Dominik Nöger

under supervision of
Priv.-Doz. Mgr. David Holec, PhD

at the

Department for Physical Metallurgy and Materials Testing
of the
Montanuniversität Leoben

December 2018

Affidavit

I declare in lieu of oath, that I wrote this thesis and performed the associated research myself, using only literature cited in this volume.

Eidesstattliche Erklärung

Ich erkläre an Eides statt, dass ich diese Arbeit selbstständig verfasst, andere als die anegebenen Quellen und Hilfsmittel nicht benutzt und mich auch sonst keiner unerlaubten Hilfsmittel bedient habe.

Leoben, December 2018

Dominik Nöger

Acknowledgments

I want to thank all people who accompanied and supported me during my studies. I want the express my special thank to some of them.

First and foremost I want to thank my parents, my mother Sonja my father Franz. With their support, both emotionally and financially, throughout my whole life they made it possible for me to make it to this point in life. I am therefore immeasurably grateful.

Secondly, I would like to scincerely thank my supervisor Priv.-Doz. Mgr. David Holec, PhD, for the patient guidance, encouragement and advice he has provided throughout my time as his student. I have been extremely lucky to have a supervisor who cared so much about my work, and who had always an open ear for my concerns also outside of work. Threfore I am really looking forward to my PhD studies.

Finally I want to express my special gratitude to my wonderful fiancée Sabrina, who always supported me also in difficult hours. I love you.

Furthermore I also gratefully acknowledge the financial support under the scope of the COMET program within the K2 Center "Integrated Computational Material, Process and Product Engineering (IC-MPPE)" (Project No. 859480). This program is supported by the Austrian Federal Ministries for Transport, Innovation and Technology (BMVIT) and for Digital and Economic Affairs (BMDW), represented by the Austrian research funding association (FFG), and the federal states of Styria, Upper Austria and Tyrol.

The computational results presented have been achieved (in part) using the Vienna Scientific Cluster 3 (VSC-3).

Abstract

On a long path of finding appropriate materials to store hydrogen, graphene and carbon nanotubes have drawn a lot of attention as potential storage materials. Their advantages lie at hand since those materials provide a large surface area (which can be used for physisorption), are cheap compared to metal hydrides, are abundant nearly everywhere, and most importantly, can increase safety to existing storage solutions. Therefore, a great variety of theoretical studies were employed to study those materials.

After a benchmark study of different van-der-Waals corrections to Generalized Gradient Approximation (GGA), the present Density Functional Theory (DFT) study employs Tkatchenko-Schäffler (TS) correction to study the influence of vacancy and Stone-Wales defects in graphene on the physisorption of the hydrogen molecule. Finally, the impact of different carbon nanotube diameters and geometries (zigzag & armchair confguration) on physisorption energetics and behavior is presented.

Kurzfassung

Während der langen Suche nach Materialien für die Speicherung von Wasserstoff, haben sich besonders Graphen und Kohlenstoffnanoröhrchen als potentielle Kandidaten hervorgetan. Die Vorteile dieser Materialien liegen auf der Hand. Zum ersten eine große spezifische Oberfläche auf der Wasserstoff adsorbiert werden kannn, niedrige Preise im Vergleich zu Metallhydraten, sowie weltweite Vorkommen, um nur einige Vorteile zu nennen. Zum zweiten kann die Sicherheit im Gegensatz zu existierenden Lösungen erhöht werden. Aus diesen Gründen wurden bereits viele theoretische und experimentelle Studien durchgeführt. Nach einer Benchmark-Studie von verschiedenen van-der-Waals Korrekturen für Generalized Gradient Approximation (GGA) Funktionale, setzt die hier präsentierte Dichtefunktionaltheorie- (DFT) Studie eine Korrektur nach Tkatchenko-Schäffler (TS) ein, um den Einfluss von Leerstellen und Stone-Wales Defekten in Graphen auf das Physisorptionsverhalten von Wasserstoff zu untersuchen. Weiters wird der Einfluss des Durchmessers von Kohlenstoffnanoröhrchen, sowie deren Geometrie (*zigzag* & *armchair*) auf die Wechselwirkungsenergien mit dem H_2 Molekül präsentiert.

Contents

Chapter 1

Introduction

Hydrogen storage

Storing hydrogen in a cheap and effective way is one of the biggest challenges when it comes finding sustainable energy solutions. Consequently, researchers all over the world approached this problem from many different fields and came up with many solutions, however, without achieving a breakthrough. Basically one can distinguish between two forms of hydrogen storage, namely physical-based and material-based. Physical-based storage is the technologically most advanced form, where the hydrogen is stored as a gas or liquid e.g. in pressurized gas tanks. Storing hydrogen in tanks however, implies either pressures as high as 700 bar or "low" (< 150 K) temperatures, neither of which is easily implemented for automotive applications. Material-based applications can be further divided into systems where hydrogen is either physically stored on materials or chemically bonded to materials or molecules. Since the last decades the a of effort has been put into finding material-based solutions to avoid non-ambient conditions, to increase saftey and decrease costs. The U.S Department of Energy (DOE) defined goals for the hydrogen uptake (9 wt.% in 2015) which are being raced for by many research groups. A few recent achievements are given here to illustrate the interdisciplinarity of this problem.

- In 2007 biochemical scientists at the Oak Ridge National Laboratory (ORNL) found a way to use starch and water as a hydrogen carrier and claimed an uptake of 14 wt.% (*1*).
- In 2009 an uptake of 10 wt.% could be achieved by employing metal organic framework by researchers of the University of Nottingham (*2*).

- Recently, Australian researchers even managed to power a car with ammonium by literally undoing the HABER-BOSCH synthesis (*3*).

Also carbon nanostructures such as carbon nanotubes (CNTs) or graphene were under heavy consideration as storage materials. It was the discoverer of graphene himself, GEIM, who showed that the novel 2D material could store hydrogen easily and release it again at higher temperatures (*4*). Nevertheless graphene is up to now a very expensive material and it is not possible to produce it in vast amounts. The main focus of the researches examining carbon structures however shifted away from CNTs since their uptake is too small to meet the DOE criterions, especially at room temperature. Recent studies have tried to employ extremely cheap activated carbon with tailored porosity size and extremely high porosities to meet the desired uptake goals (*5–7*).

The presented thesis provides a benchmark calculation for different van-der-Waals correction schemes, to study the interaction between the H_2 molecule and carbon nanostructures. The first part of the results deals with the adsorption behaviour of perfect graphene. Next the influence of vacancy and STONE-WALES defects in graphene on the adsorption is presented. Finally, the third part investigates the adsorption of the H_2 molecule on the outer wall of single-walled carbon nanotubes (SWCNT). This study is a part of larger project aiming on building a multi-method package for multi-scale modelling of interaction between H and structurally complex (e.g., nanoporous) carbon structures.

Chapter 2

Theoretical background

2.1 Carbon nanostructures

Although a large variety of carbon nanostructures, so-called fullerenes, proved experimentally existent already in the 1970s (*8*, *9*), the research on hydrogen storage materials deals mostly with bulk nanoporous carbon. For the sake of easiness, the present thesis focuses on graphene and carbon nanotubes, as representatives of well defined carbon nanostructures, which still contain different bonding as well as geometrical environments.

2.1.1 Graphene

In the 1960s theoretical studies led to the Mermin-Wagner theorem (*10*), postulating that 2D materials would not be stable for finite temperatures. Nevertheless, further theoretical investigations (*11*) stated that certain materials could violate the theorem. So does graphene. When it was discovered to be the first true 2D crystal by Geim and Novosolev (*12*) its extraordinary properties made it one of the most intensively studied material. The hexagonal crystal lattice of sp^2 bonded carbon atoms with a bond length of 1.42 Åis created by three in-plane σ bonds. The π orbital is aligned perpendicular to the plane. Since the sp^2 bond is one of the strongest known, graphene shows remarkable mechanical properties (*13*). Similarly, the electronic structure is very special due to the fact that the valence and conduction bands meet at the K point in the reciprocal space (so-called Dirac points), electrons move as if they had no mass (band curvature is zero) leading to extremely high electron mobility (*4*). Consequently, the electric resistivity is the lowest known up to now (*14*). Graphene and graphene-like materials are also serious candidates for hydrogen storage due to their huge specific area (2630 m^2/g). Experimental (*15*) and lots of theoretical studies (*16–18*) with

different approaches like DFT or MD have already been carried out to study the interaction with hydrogen. Also in this thesis graphene is one of the main topics.

2.1.2 Carbon nanotubes

After KROTO *et al.* found fullerenes in 1985 (*9*), the existence of carbon nanotubes was speculated until finally in 1991 IIJIMA found them in experiments (*19*). A single-walled carbon Nanotubes (SWCNTs) is simply a rolled up sheet of graphene. Although in reality also multi-walled carbon nanotubes (MWCNTs) are observed, they are not considered here. As well as graphene CNTs also show remarkable properties. Depending on the way (under which angle) one cuts out the CNT from the graphene plane, metallic or semiconducting behaviour can be observed. Similarly to graphene CNTs show extraordinary mechanical (stiffness ≈ 1 TPa), electronic and heat conduction properties. CNTs already found real-world applications such as reinforcement fibers for polymers or transistors. Since they possibly could trap hydrogen inside the tube, they are also thoroughly studied by research groups worldwide as potential candidates for hydrogen storage materials (*20–24*).

2.1.2.1 Structure of carbon nanotubes

As mentioned before a CNT is a rolled-up sheet of graphene. To model this and generate CNT unit cells, a short excursion to the mathematical description of the structure of CNTs is given here.

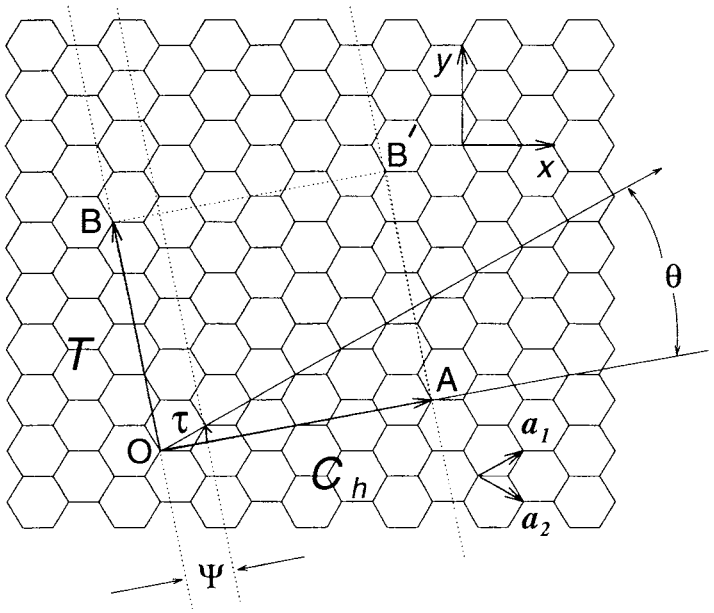

Figure 2.1: Schematic unit cell of a chiral $n = 4$, $m = 2$ nanotube. $\vec{C}_h$ denotes the chiral vector (*25*) and $\vec{T}$ the tubule translation vector. ψ and τ correspond to the symmetry operation

2.1.2.2 Tubule lattice vectors

Consider a graphene plane with lattice parameters $\vec{a}_1 = \left(\frac{3}{2}a_{C-C},\ \frac{\sqrt{3}}{2}a_{C-C}\right)$ and $\vec{a}_2 = \left(\frac{3}{2}a_{C-C},\ -\frac{\sqrt{3}}{2}a_{C-C}\right)$, where a_{C-C} denotes the carbon-carbon bondlength, as it is illustrated in Fig. 2.1. A SWCNT is fully defined by two *chirality* parameters n and m, which define at which angle the unit cell is cut from the graphene plane. Both parameters compose the *chirality vector* $\vec{C}_h$ as

$$\vec{C}_h = n\vec{a}_1 + m\vec{a}_2 \tag{2.1}$$

along which the tube is rolled up (*26*). Thus the tube diameter is given by

$$d_t = \frac{||\vec{C}_h||}{\pi} = \frac{\sqrt{3}a_{C-C}\sqrt{n^2 + nm + m^2}}{\pi} \tag{2.2}$$

The *chiral angle* Θ as illustrated in Fig. 2.1 is given by

$$\Theta = \arctan\left(\frac{\sqrt{3}m}{2n + m}\right) \tag{2.3}$$

The *tube translation vector* $\vec{T}$ is introduced orthogonal to the chiral vector $\vec{C}_h$ and defines the length of the unit cell in the tube axis direction and is defined as

$$\vec{T} = \frac{2m+n}{d_R}\vec{a}_1 + \frac{2n+m}{d_R}\vec{a}_2 \tag{2.4}$$

with d_R being given as

$$\begin{aligned} d &= \gcd(m,n) \\ d_R &= \begin{cases} d & \text{if } (n-m) \text{ is not a multiple of } 3d \\ 3d & \text{if } (n-m) \text{ is a multiple of } 3d \end{cases} \end{aligned} \tag{2.5}$$

where $\gcd(n,m)$ is the greatest common divisor of the two chirality parameters n and m. The number of hexagons in the unit cell can be calculated using the formula

$$N = \frac{2\left(m^2+n^2+nm\right)}{d_R} \tag{2.6}$$

which will be needed later on to calculate the atomic positions.

2.1.3 Atomic coordinates

The basic space group symmetry operation of a general (chiral) nanotube is composed of a rotation ψ and a translation τ which is represented with a *symmetry vector* $\vec{R}$ such that $\psi = \vec{R}\cdot\vec{C}_h$ and $\tau = \vec{R}\cdot\vec{T}$ holds true (*25*). The symmetry vector is defined as

$$\vec{R} = p\vec{a}_1 + q\vec{a}_2 \tag{2.7}$$

$$\psi = \vec{R}\cdot\vec{C}_h = \frac{2\pi}{N} \tag{2.8}$$

$$\tau = \vec{R}\cdot\vec{T} = \frac{(mp-nq)||\vec{T}||}{N} \tag{2.9}$$

The integer pair (p,q) can be determined by finding a solution to the diophantine equation $d = mp - nq$. (p,q) represents the coordinates of the origin after the symmetry operation $(\psi|\tau)$ acted on it, i.e. $(\psi|\tau)(0,0) = (p,q)$. (*25*). For obtaining the coordinates of the individual atoms one transforms each lattice site and adds two atoms per site since two atoms are needed to represent a honeycomb structure. The atom positions are therefore given for a lattice site i

$$\begin{aligned} \vec{x}_{i,1} &= \left[\frac{d_t}{2}\cos(i\psi),\ \frac{d_t}{2}\sin(i\psi),\ i\tau\right] \\ \vec{x}_{i,2} &= \left[\frac{d_t}{2}\cos(i\psi+\psi_0),\ \frac{d_t}{2}\sin(i\psi+\psi_0),\ i\tau+\tau_0\right] \end{aligned} \tag{2.10}$$

where t_0 and ψ_0 represent the rotation and translation between the two atoms of the basis and are given by

$$\tau_0 = a_{C-C} \sin\left(\frac{\pi}{6} - \Theta\right) \tag{2.11}$$

$$\psi_0 = \frac{a_{C-C} \sin\left(\frac{\pi}{6} - \Theta\right)}{2\pi ||\vec{C}_h||} \tag{2.12}$$

Using all these equations, a *Python* script for generating SWCNTs was implemented, which just takes the chirality parameters n and m as input arguments and generates the nanotube unit cell. It is also possible to specify a vacuum around the CNT to avoid the interaction with its periodic image due to periodic boundary conditions. Figure 2.2 shows the structural model when rolling up the graphene sheet as illustrated in Fig. 2.1.

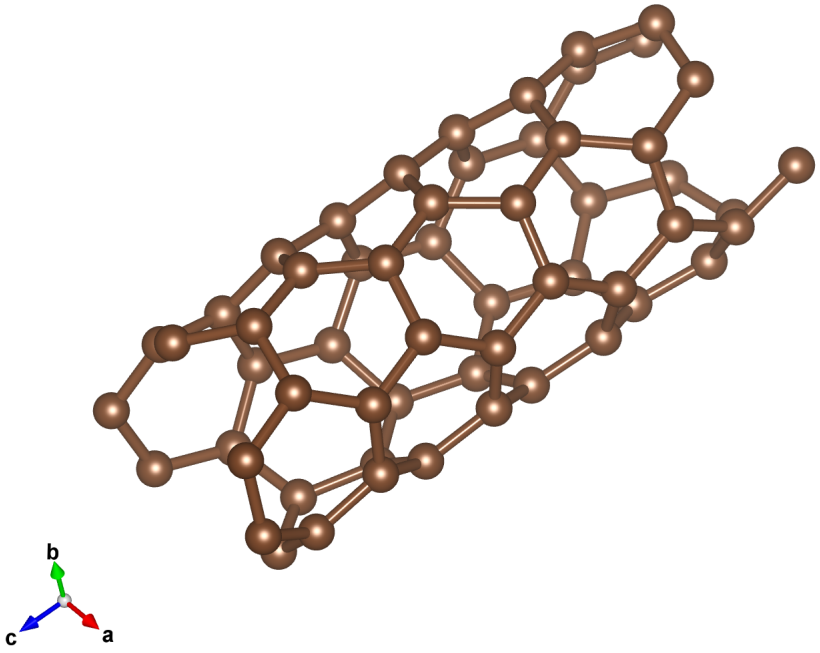

Figure 2.2: Structural model of an $n = 4, m = 2$ chiral carbon nanotube, generated with the aforementiond *Python* script

2.2 Density Functional Theory (DFT)

Since Density Functional Theory (DFT) is a very sophisticated *ab-initio* method for electronic structure calculations, this chapter aims to introduce the reader to only rough ideas about the basic theorems and principles. There are many books which describe all aspects of DFT in more detail. A freely available ABC of DFT from Burke is recommended to get a good insight (*27*).

2.2.1 Many-body Schrödinger equation

Finding solutions for the Schrödinger equation is one of the main tasks of quantum mechanics. In its time-independent version (Eq. 2.13) $\hat{\mathcal{H}}$ denotes the Hamiltonian which is the total energy operator and uniquely describes the underlying quantum-mechanical system.

$$\hat{\mathcal{H}}\Psi = E\Psi \tag{2.13}$$

Although it is easy to find a solution for one particle, the complexity increases dramatically for more particles. Therefore consider a generic system with N nuclei at positions $\vec{R}_i$ as well as n electrons at positions $\vec{r}_i$. Thus the wave-function becomes a function of the coordinates of each particle $\Psi\left(\vec{R}_1, \ldots, \vec{R}_N, \vec{r}_1, \ldots, \vec{r}_n\right)$ and is therefore a function of $3 \times (N+n)$ variables. If more than one particle is under consideration also their mutual interactions have to be taken into account, yielding a Hamiltonian of the form of Eq. 2.14 which describes the aforementioned system properly. The operators $\hat{T}_N$ and $\hat{T}_e$ denote the kinetic energy operators of the nuclei and electrons. $\hat{V}_{N\leftrightarrow e}$, $\hat{V}_{N\leftrightarrow N}$ and $\hat{V}_{e\leftrightarrow e}$ therefore represent the operators to obtain the potential energy of nucleus-electron, nucleus-nucleus, and electron-electron Coulomb interactions. It turns out that it is not possible to to find an analytical solution to the Schrödinger equation with the Hamiltonian from Eq. 2.14 for more than a few particles because of its extraordinary difficulty.

$$\begin{aligned}\hat{H} = &\overbrace{-\frac{\hbar^2}{2}\sum_i^N \frac{\nabla^2_{\vec{R}_i}}{M_i}}^{\hat{T}_N} - \overbrace{\frac{\hbar^2}{2}\sum_i^n \frac{\nabla^2_{\vec{r}_i}}{m_e}}^{\hat{T}_e} - \overbrace{\frac{1}{4\pi\epsilon_0}\sum_i^N\sum_j^n \frac{e^2 Z_i}{\left|\vec{R}_i - \vec{r}_j\right|}}^{\hat{V}_{N\leftrightarrow e}} \\ &+ \underbrace{\frac{1}{8\pi\epsilon_0}\sum_i^N\sum_j^N \frac{e^2 Z_i Z_j}{\left|\vec{R}_i - \vec{R}_j\right|}}_{\hat{V}_{N\leftrightarrow N}} + \underbrace{\frac{1}{8\pi\epsilon_0}\sum_i^n\sum_j^n \frac{e^2}{|\vec{r}_i - \vec{r}_j|}}_{\hat{V}_{e\leftrightarrow e}}\end{aligned} \tag{2.14}$$

2.2.1.1 Born-Oppenheimer approximation

It is obvious that the many-body problem has to be simplified in some meaningful way. In 1927, Born and Oppenheimer (*28*) suggested neglecting the motion of the nuclei since they are much heavier and slower than the electrons. From the perspective of a moving electron, the nucleus appears as a fixed point since it is $M\frac{m_p}{m_e}$ (M denotes the atomic mass number, $m_p \approx m_n$) times heavier and consequently reacts to external forces much slower. This obvious and intuitive simplification has however a great impact on the Hamiltonian. First of all, the wave function's complexity is dramatically reduced and becomes a function of the electron positions only $\Psi(\vec{r}_1, \ldots, \vec{r}_n)$. Secondly, since the velocity of the nuclei is small $\nabla\vec{R}_i < \nabla\vec{r}_i$ as well $\nabla^2\vec{R}_i \ll \nabla^2\vec{r}_i$ holds true. Further, the approximation imposes that $\hat{V}_{N\leftrightarrow N}$ becomes a constant and $\hat{V}_{N\leftrightarrow e}$ becomes just an ordinary external potential. Finally, the many-body Hamiltonian can be reduced to

$$\begin{aligned}\hat{H} &= \hat{T}_e + \hat{V}_{e\leftrightarrow e} + \hat{V}_{ext} \\ &= \underbrace{-\frac{\hbar^2}{2}\sum_i^n \frac{\nabla^2_{\vec{r}_i}}{m_e}}_{\hat{T}_e} + \underbrace{\frac{1}{8\pi\epsilon_0}\sum_i^n\sum_j^n \frac{e^2}{|\vec{r}_i - \vec{r}_j|}}_{\hat{V}_{e\leftrightarrow e}} + \underbrace{\hat{V}_{ext}}_{\hat{V}_{N\leftrightarrow N}+\hat{V}_{N\leftrightarrow e}}\end{aligned} \tag{2.15}$$

Although this simplification reduces the complexity a lot, the problem is still not tractable at least not for real solids. However, the Ritz-Rayleigh variational principle (*29*) provides a method to find the lowest eigenvalue E_0 of this problem and therefore a way to find a solution. Nevertheless, this still proves difficult in reality. The principle states if the Hamiltonian acts on a family of test vectors Ψ constructed from an orthonormal basis set, the vector with the lowest energy represents the ground state, while all others will give a higher energy states. However, the basis set is not obligated to have finite dimensions which is indeed the case for the wave functions in the Hilbert space.

$$E_0 \leq \frac{\langle\Psi|\hat{H}|\Psi\rangle}{\langle\Psi|\Psi\rangle} \tag{2.16}$$

2.2.2 Hohenberg-Kohn theorems

Since methods which find an approximate solutions to the wavefunction itself such as e.g the Hartree-Fock (*30*) approach, are very limited in terms of system size, other researchers tried to employ the charge density $\rho(\vec{r})$ as Thomas and Fermi did already in 1927 (*31*).

Despite those early steps, it took until the 1960s when HOHENBERG and KOHN proved that a system can be fully described by its charge density (*32*). These two theorems represent a real breakthrough since if one is able to describe a system with only the charge density instead of the many-body wave function, the problem is reduced to searching for a function of only three variables. As a consequence, the problem can be treated much easier and many more particles can be handled in practice. The charge density itself is an observable of the problem, and therefore can be obtained by applying the single-particle density operator on the many-body wavefunction. Again, consider a system with n electrons. Then the charge density can be written as

$$\begin{aligned}\rho(\vec{r}) = \langle\Psi|\hat{\rho}|\Psi\rangle &= \sum_i^n \int \delta(\vec{r}-\vec{r}_i)|\Psi\left(\vec{r}_1,\ldots,\vec{r}_n\right)|^2 \mathrm{d}\vec{r}_1\cdots\mathrm{d}\vec{r}_n \\ &= \int |\Psi\left(\vec{r},\vec{r}_2,\ldots,\vec{r}_n\right)|^2 \mathrm{d}\vec{r}_2\mathrm{d}\vec{r}_3\cdots\mathrm{d}\vec{r}_n + \int |\Psi\left(\vec{r}_1,\vec{r},\ldots,\vec{r}_n\right)|^2 \mathrm{d}\vec{r}_1\mathrm{d}\vec{r}_3\cdots\mathrm{d}\vec{r}_n + \ldots \\ &= n\int |\Psi\left(\vec{r},\ldots,\vec{r}_n\right)|^2 \mathrm{d}\vec{r}_2\cdots\mathrm{d}\vec{r}_n\end{aligned} \tag{2.17}$$

Since the following two theorems are fundamental for the density functional theory, a short proof will be presented (*33*).

Theorem 1. *For any system of interacting particles in an external potential $V_{ext}(\vec{r})$, the density is uniquely determined.*

Proof. Let $\hat{H}^a = \hat{T}_e + \hat{V}_{e\leftrightarrow e} + V^a_{ext}(\vec{r})$ and $\hat{H}^b = \hat{T}_e + \hat{V}_{e\leftrightarrow e} + V^b_{ext}(\vec{r})$ be two distinct Hamiltonians. The external potentials differ by more than a constant $V^a_{ext}(\vec{r}) - V^b_{ext}(\vec{r}) \neq const.$ $V^a_{ext}(\vec{r})$ and $V^b_{ext}(\vec{r})$ correspond to the same ground state electron density $\rho_0(\vec{r})$, thus $\hat{H}^a$ and $\hat{H}^b$ give rise to two different wave functions Ψ^a and Ψ^b

From the variational principle from Eq. 2.16 we know that no wave function can yield a lower energy than Ψ^a if $\hat{H}^a$ acts on it, thus

$$E^a_0 = \langle\Psi^a|\hat{H}^a|\Psi^a\rangle < \langle\Psi^b|\hat{H}^a|\Psi^b\rangle \tag{2.18}$$

must hold true. Since both Hamiltonians have the same ground state density it is easy to rewrite the expectation value from Eq. 2.18 to

$$\langle\Psi^b|\hat{H}^a|\Psi^b\rangle = \overbrace{\langle\Psi^b|\hat{H}^b|\Psi^b\rangle}^{E^b_0} + \int \left[V^a_{ext}(\vec{r}) - V^b_{ext}(\vec{r})\right]\rho_0(\vec{r})\mathrm{d}\vec{r} \tag{2.19}$$

Analogously one ends up with

$$\langle \Psi^a | \hat{H}^b | \Psi^a \rangle = \overbrace{\langle \Psi^a | \hat{H}^a | \Psi^a \rangle}^{E_0^a} + \int \left[V_{ext}^b(\vec{r}) - V_{ext}^a(\vec{r}) \right] \rho_0(\vec{r}) \mathrm{d}\vec{r} \tag{2.20}$$

Adding up Eq. 2.19 and Eq 2.24 leads to a simple contradiction.

$$E_0^a + E_0^b < E_0^b + E_0^a \tag{2.21}$$

Therefore the theorem has been proven by a very simple *reductio ad absurdum* □

Since it was shown that the external potential uniquely determines the electron density and vice versa, the ground state wavefunction, therefore, is also determined. Furthermore, this implies that all the observables such as kinetic energy or momentum are uniquely determined which therefore automatically leads to the second theorem of Hohenberg and Kohn.

Theorem 2. *Since all observables are uniquely determined for a given charge density, one can reformulate the energy as a functional of the charge density $\rho_(\vec{r})$ (Eq. 2.22). For all electronic structure problems a universial functional $E[\rho]$ can be formulated such that the ground state energy is the global minimum value of the functional $E[\rho]$.*

Proof. Again let $\hat{H} = \hat{T}_e + \hat{V}_{e\leftrightarrow e} + V_{ext}(\vec{r})$ and $\psi[\rho]$ be the minimizing wave-function. The energy can then be written as the following functional

$$\begin{aligned} E[\rho] &= \langle \Psi[\rho] | \hat{H} | \Psi[\rho] \rangle = \langle \Psi[\rho] | \hat{T}_e + \hat{V}_{e\leftrightarrow e} | \Psi[\rho] \rangle + \int V_{ext}(\vec{r}) \rho(\vec{r}) \mathrm{d}\vec{r} \\ &= T_e[\rho] + V_{e\leftrightarrow e}[\rho] + \int V_{ext}(\vec{r}) \rho(\vec{r}) \mathrm{d}\vec{r} \end{aligned} \tag{2.22}$$

From the first theorem it is known that only one charge density $\rho^a(\vec{r})$ yields the ground state energy

$$E_0^a = E[\rho^a] = T[\rho^a] + V_{e\leftrightarrow e}[\rho^a] + \int V_{ext}(\vec{r}) \rho^a(\vec{r}) \mathrm{d}\vec{r} \tag{2.23}$$

From the variational principle (Eq. 2.16), a different charge density $\rho^b(\vec{r})$ yields a higher energy if fed into Eq. 2.22.

$$E_0^a = \langle \Psi^a | \hat{H}^a | \Psi^a \rangle < \langle \Psi^b | \hat{H}^a | \Psi^b \rangle = E_0^b \tag{2.24}$$

□

By finding the minimum of this functional $\frac{\delta E[\rho(\vec{r})]}{\delta\rho(\vec{r})} = 0$ the total energy of the ground state can be obtained. However, for certain contributions to the total energy no functional representation has been found yet. Although those theorems changed the way how electronic structure problems were approached, they still provide (only) a variational principle approach but no direct recipe how to solve the many-body problem. Only a year later, KOHN together with SHAM (*34*) provides such recipie, based on the theorems above.

2.2.3 Kohn-Sham method

The major idea behind this method is to represent the physical system by a set of fictitious non-interacting particles, which themselves are influenced by an external effective potential V_{eff}. However, these fictitious particles give rise to the same charge density as the real physical system. Therefore the problem is transformed into an eigenvalue one-particle problem of the form

$$\left\{-\frac{\hbar^2}{2m}\nabla^2 + V_{\text{eff}}(\vec{r})\right\}\phi_i(\vec{r}) = \epsilon_i\phi_i(\vec{r}) \tag{2.25}$$

with

$$\rho(\vec{r}) = \sum_i^N |\phi_i(\vec{r})|^2. \tag{2.26}$$

Here, $\phi_i(\vec{r})$ denote the so-called KOHN-SHAM (KS) orbitals and ϵ_i the corresponding eigenvalues. It lies at hand that the eigenvalues of the system obtained from Eq. 2.25 do not represent the single electron energies. However, it has been shown that the KS-orbitals can give a very decent description of real electronic band structures (*35*). The KOHN-SHAM wave function (in the following $\Phi(\vec{r})$) is then expressed as the SLATER determinant of the single particle KS orbitals (*36*). Anyway, a set of non-interacting particles does neglect two fundamental principles of quantum mechanics and therefore will yield a different energy if the contributions are not considered in the effective potential term V_{eff}. The neglected effects are

- the exchange energy originating from the PAULI repulsion
- the correlation energy which one can think of the electron-electron repulsion

Consequently the effective potential V_{eff} includes a non-classical term V_{XC} which takes into account PAULI exchange interactions as well as correlations (correction of the single-particle treatment)

Thefore, the energy functional as introduced by the second HOHENBERG-KOHN (Eq. 2.22) becomes

$$\begin{aligned} E[\rho(\vec{r})] &= T_s[\rho(\vec{r})] + \int V_{\text{eff}}(\vec{r})\rho(\vec{r})\mathrm{d}\vec{r} \\ &= T_s[\rho(\vec{r})] + \int V_{e\leftrightarrow e}(\vec{r})\rho(\vec{r})\mathrm{d}\vec{r} + \int V_{\text{ext}}(\vec{r})\rho(\vec{r})\mathrm{d}\vec{r} + \underbrace{\int V_{XC}(\vec{r})\rho(\vec{r})\mathrm{d}\vec{r}}_{E_{XC}} \end{aligned} \tag{2.27}$$

where $\hat{T}_s$ is the single particle kinetic energy operator therefore neglecting the correlation energy such that $T[\rho] = T_s[\rho]+T_c[\rho]$ holds true. The missing part of the kinetic energy $T_c[\rho]$ is included in the $E_{XC}[\rho(\vec{r})]$ term which represents the exchange-correlation energy functional. The $E_{XC}[\rho(\vec{r})]$ term of this equation is very crucial, because it has to be approximated. The kinetic energy can be writte in functional representation as

$$T_s[\rho(\vec{r})] = -\frac{\hbar^2}{2m}\sum_i^N \langle\phi_i|\nabla^2|\phi_i\rangle \tag{2.28}$$

With all these definitions one can rewrite the effective potential as V_{eff}

$$\begin{aligned} V_{\text{eff}}(\vec{r}) &= \frac{\delta}{\delta\rho(\vec{r})}\left\{ \underbrace{\langle\Phi|\hat{V}_{\text{ext}}|\Phi\rangle}_{\hat{V}_{N\leftrightarrow N}+\hat{V}_{N\leftrightarrow e}} + \langle\Phi|\hat{V}_{e\leftrightarrow e}|\Phi\rangle + E_{XC}[\rho(\vec{r}),\nabla\rho(\vec{r}),\ldots] \right\} \\ &= \frac{\delta}{\delta\rho(\vec{r})}\int V_{ext}(\vec{r})\underbrace{|\Phi(\vec{r})|^2}_{\rho(\vec{r})}\mathrm{d}\vec{r} + \frac{\delta}{\delta\rho(\vec{r})}\underbrace{\left\{\frac{1}{8\pi\varepsilon_0}\int\int\frac{\rho(\vec{r})\rho(\vec{r})}{|\vec{r}-\vec{r}'|}\mathrm{d}\vec{r}'\mathrm{d}\vec{r}\right\}}_{E_{\text{Hartree}}} + \frac{\delta E_{XC}[\rho(\vec{r}),\nabla\rho(\vec{r}),\ldots]}{\delta\rho(\vec{r})} \\ &= V_{\text{ext}}(\vec{r}) + \underbrace{\frac{1}{4\pi\varepsilon_0}\int\frac{\rho(\vec{r}')}{|\vec{r}-\vec{r}'|}\mathrm{d}\vec{r}'}_{V_{e\leftrightarrow e}} + V_{XC}(\rho(\vec{r}),\nabla\rho(\vec{r}),\ldots) \end{aligned} \tag{2.29}$$

Because of the first HOHENBERG-KOHN theorem, the potential in Eq. 2.29 is unique. The KOHN-SHAM equations (Eqs. 2.25 , 2.27) provide an exact theory and yield the correct charge density for any system if the exchange-correlation functional is known. There is

nothing approximative in KS theory apart from the Born-Oppenheimer approximation. However the $E_{XC}[\rho(\vec{r}), \nabla\rho(\vec{r}), \ldots]$ term is unknown and has to be approximated. In return the KS equations are a set of single particle equations and thus can be handled much easier than any explicit many-body treatment.

2.2.4 LDA and GGA

The quality of an DFT calculation depends mostly on how well the XC-functional is able to mimic the behaviour of the system under consideration. The two simpliest but most widely spread approximations are described below.

2.2.4.1 Local Density Approximation

The first approximation of the $E_{XC}[\rho(\vec{r}), \nabla\rho(\vec{r}), \ldots]$ functional was suggested already by Hohenberg and Kohn themselves in the original paper (*34*). Their idea was to approximate the exchange-correlation energy by that of a uniform electronic gas. Thus $E_{XC}[\rho(\vec{r}), \nabla\rho(\vec{r}), \ldots]$ becomes only a functional of the density itself

$$E_{XC}^{\mathrm{LDA}}[\rho(\vec{r})] = \int \rho(\vec{r})\varepsilon_{XC}^{\mathrm{hom}}[\rho(\vec{r})]\mathrm{d}\vec{r} \tag{2.30}$$

where $\varepsilon_{XC}^{\mathrm{hom}}[\rho(\vec{r}]$ is the exchange-correlation energy density of a homogeneous electron gas. The $E_{XC}[\rho(\vec{r})]$ is assembled by two contributions, the exchange energy functional $E_X^{\mathrm{hom}}[\rho(\vec{r})]$ and the correlation functional $E_C^{\mathrm{hom}}[\rho(\vec{r})]$. Only a few years after the Thomas-Fermi theory was published, Dirac already in 1930 (*37*) found an approximation to the exchange term of the homogeneous electron gas

$$V_X^{\mathrm{hom}}[\rho(\vec{r})] = -\frac{3}{4}\left(\frac{3}{\pi}\right)^{\frac{1}{3}} \int \rho(\vec{r})^{\frac{4}{3}}\mathrm{d}\vec{r}. \tag{2.31}$$

The correlation $E_C^{\mathrm{hom}}[\rho(\vec{r})]$ is somewhat more difficult to handle. Although Wigner could find an approximation for low electron densities (*38*) and Gell-Mann *et al.* a limit form for high densities (*39*), a general approximation was not found. Instead, an interpolation formula is used to interpolate between those known limits (*40*). Perdew and Zunger suggested calculating the coefficients of this interpolation function from quantum Monte-Carlo data (*41*). Although LDA is a very simple and crude approximation, it turned out to be a real success due to the cancellation of errors, since LDA tends to overestimate E_X and underestimate E_C. However, for systems like metals where fluctuations in the electron density are usually small, LDA yields good results.

2.2.4.2 Generalized Gradient Approximation

It was already KOHN and SHAM themselves which predicted that higher order approximations (including the gradient) would be necessary to get a better estimate of the exchange-correlation energy. Despite the first implementation of an approximation using the density gradient failed, based on the work of PERDEW (*42*) *et al.* the Generalized Gradient Approximation (GGA) became a real breakthrough. Although PERDEW's method is a rather crude approach as well, the GGA could drastically reduce the effect of LDA tending to overbind solids and molecules. The general form of GGA can be written as

$$E_{XC}^{\mathrm{GGA}}[\rho(\vec{r}), \nabla\rho(\vec{r})] = \int \rho(\vec{r})\varepsilon_{XC}^{\mathrm{hom}}(\rho(\vec{r}))F_{XC}(\rho(\vec{r}), \nabla\rho(\vec{r}))\mathrm{d}\vec{r} \tag{2.32}$$

where $F_{XC}(\rho(\vec{r}), \nabla\rho(\vec{r}))$ is an analytic function, usually named the GGA enhancement factor, and is often written as a function of the reduced spin density gradient s.

$$s(\vec{r}) = \frac{|\nabla\rho(\vec{r})|}{2\underbrace{(3\pi^2\rho(\vec{r}))^{\frac{1}{3}}}_{\vec{k}_F}\rho(\vec{r})} \tag{2.33}$$

In 1991 PERDEW and WANG came up with a fully non-empirical functional for F_{XC} (`PW91`) (*42*, *43*) which extended BECKE's `B88` functional (*44*). Perhaps the most used functional today is the `PBE` parameterization of the F_{XC} enhancement factor as proposed by PERDEW, BURKE, and ERNZERHOF (*45*, *46*).

2.3 Van der Waals correction to exchange-correlation functionals

When KOHN and SHAM proposed the LDA approximation for the E_{XC} functional, it enabled the boom of quantum mechanical calculations. Nevertheless, various GGA types proved to be the optimum between the accuracy and the computational effort. Despite their robustness and general accuracy, GGA functionals fail in describing long-range VAN-DER WAALS interactions. Therefore the following sections provide an overview of how this problem is currently approached in the DFT.

2.3.1 DFT-D

One of the most intuitive yet powerful approaches was suggested by GRIMME (*47*), which provides a semi-empirical correction to the total energy, in a form

$$E_{DFT-D} = E_{DFT} + E_{disp} \tag{2.34}$$

holds true. E_{DFT} denotes just the total energy obtained from the system by solving the KS equations. E_{disp} provides the semi-empirical correction originating from the vdW interactions. From the physical point of view, the dispersion energy is negative, since vdW interactions involve the correlated movement of electrons which are actually relatively far away and therefore the total energy is lowered. In general, within the DFT-D method the dispersion energy E_{disp} is calculated as the sum of all pair LONDON atom-atom interaction energies (*48*) multiplied by a correction term, the so-called damping function f_{damp}. GRIMME states however that there is no direct physical meaning of E_{disp} because it is a model dependent quantity (*47*). Since the publication of the DFT-D method in 2004 a lot of different damping functions have been proposed. It seems that the choice of the damping function however has only a minor influence on the result (*49*, *50*).

2.3.2 DFT-D2 method

The DFT-D2 method was also suggested by GRIMME (*51*) and provides a semiempirical term for the dispersion energy in Eq. 2.34 as the sum of pair atom-atom interactions. As LONDON already found in the last century, the dispersion energy between two atoms A and B can be approximated as

$$E_{disp}^{AB} \approx \overbrace{-\frac{3I_A I_B \alpha_A \alpha_B}{2(I_A + I_B)}}^{constant=C_6^{AB}} \frac{1}{r_{AB}^6} \tag{2.35}$$

where I_A and I_B correspond to the atoms first ionization potentials and α_A and α_B represent the dipole polarizabilities of the atoms A and B respectively. r_{AB} is the interatomic distance. Thus GRIMME defines the dispersion correction for a system with N atoms as the sum over all atom-atom LONDON pair interactions of the system

$$E_{disp} = -s_6 \sum_{i}^{N-1} \sum_{j>i}^{N} \frac{C_6^{ij}}{r_{ij}^6} f_{damp}(r_{ij}) \tag{2.36}$$

where s_6 is a global scaling factor. Since Eq. 2.35 is just an approximation, and therefore provides a good description for limited values of r_{ij} one needs to provide a correction term.

Thus $f_{damp}(r_{ij})$ is a damping function to correct the LONDON formula to avoid singularities for small r_{ij} and double-counting effects at intermediate distances. The damping function suggested by GRIMME is a FERMI-type one given as

$$f_{damp} = \frac{1}{1 + e^{-d\left(\frac{r_{ij}}{r_{w,i}+r_{w,j}}-1\right)}} \tag{2.37}$$

with d as design parameter for the sharpness of the FERMI edge lying at $r_{w,i} + r_{w,j}$, where $r_{w,i}$ and $r_{w,j}$ correspond to the vdW radii of the atomic species. Thus if the hard spheres with vdW radii $r_{w,j}$ and $r_{w,j}$ of the atoms touch each other exatly the damping factor will be exactly 0.5, and is much smaller for $r_{ij} < r_{w,i} + r_{w,j}$. The parameter C_6^{ij} should describe the interaction between atoms i and j, and therefore has to be approximated for a real system. This is because Eq. 2.35 does not consider the local chemical neighborhood and is therefore valid only for isolated atoms. Nevertheless, by doing a lot of calculations and testing, GRIMME found that the relationship

$$C_6^{ij} = \sqrt{C_6^i C_6^j} \tag{2.38}$$

leads to the best results (*51*). Furthermore, they showed that taking higher order correction terms into account does not significantly improve the accuracy.

2.3.3 DFT-D3 method

DFT-D3 method is an enhanced version of the DFT-D2 method. In addition to more accurate results, the E_{disp} term also considers an eighth order correction, with a different damping function f_{damp} which proved to be numerically stable for higher order corrections as well (*52*). The modified versions of Eq. 2.59 and Eq. 2.37 read (*53*)

$$E_{disp} = \sum_{i}^{N-1} \sum_{j>i}^{N} \left\{ \frac{C_6^{ij}}{r_{ij}^6} f_{damp,6}(r_{ij}) + \frac{C_8^{ij}}{r_{ij}^8} f_{damp,8}(r_{ij}) \right\} \tag{2.39}$$

$$f_{damp,n}(r_{ij}) = \frac{s_n}{1 + 6\left(\frac{r_{ij}}{s_{R,n} R_0^{ij}}\right)^{-\alpha_n}} \tag{2.40}$$

where R_0^{ij} denotes a cutoff radius and $s_{R,n}$ its order dependent scaling factor. Therefore, to fully describe Eq. 2.39 one needs to provide the steepness parameters α_6 and α_8, the scaling factors for the cutoff radii $s_{R,6}$ and $s_{R,8}$ as well as the global scaling parameters

s_6 and s_8. Although DFT packages (may) provide sensible default values, note that these values depend on the used XC functional, therefore, most of them allow to set one or more of those parameters manually to handle the XC functional influence. However, GRIMME provides sensible values for many different functionals on his webpage for zero[1] and BECKE-JOHNSON (BJ) damping[2]. There also exists a small programm written in Fortran named `dftd3`[3] which takes structure files and an XC-functional name as inputs and estimates the parameters needed for the D3 correction.

Nevertheless, the biggest differences to the DFT-D2 method are that the dispersion coefficients C_n^{ij} are also dependent on the local geometry and therefore are computed during the calculation instead of being tabulated and a three-body correction term to the dispersion energy has been added. The three body energy term is given by the sum over all triplet dispersion energies

$$E_{disp}^3 = \sum_{ijk} f_{d,3}(\bar{r}_{ijk}) \underbrace{\frac{C_9^{ijk}(3\cos(\theta_i)\cos(\theta_j)\cos(\theta_k)+1}{(r_{ij}r_{jk}r_{ik})^3}}_{E_{ijk}} \tag{2.41}$$

where E_{ijk} is the AXILROD-TELLER-MUTO dispersion energy and is obtained from third order perturbation theory (*54*, *55*). θ_i, θ_j and θ_k are the angles of the triangle formed by atoms i, j and k, while r_{ij}, r_{jk} and r_{ik} represent the interatomic distances. A very decent guess for the three body dispersion coefficient C_9^{ijk} can be calculated from the pair dispersion coefficient as (*53*)

$$C_9^{ijk} = -\sqrt{C_6^{ij}C_6^{jk}C_6^{ik}} \tag{2.42}$$

The path how to obtain the dispersion coefficients C_n^{ij} is rather complex and was suggested by Lein *et al.* (*56*) and is therefore not given here. (See: (*57*, *58*)). For the sake of completeness, it should be mentioned that the three body correction term is not implemented in VASP as it is stated in the original paper (*53*).

2.3.4 Tkatchenko-Schäffler method

Although the DFT-D3 method reduces empiricism in the van-der-Waals correction term, TKATCHENKO and SCHÄFFLER proposed a method (*59*) where the dispersion coefficients

[1] https://www.chemie.uni-bonn.de/pctc/mulliken-center/software/dft-d3/functionals

[2] https://www.chemie.uni-bonn.de/pctc/mulliken-center/software/dft-d3/functionalsbj

[3] https://www.chemie.uni-bonn.de/pctc/mulliken-center/software/dft-d3/get-the-current-version-of-dft-d3

between atoms A and B, C_6^{AB}, are calculated from the KS charge density instead of being tabulated for each atom. As seen in Eq. 2.35 the dispersion coefficient C_6^{AB} is a function of the polarizability of the two atoms. Therefore CASIMIR and POLDER found the exact relation for the dispersion coefficients (*60*)

$$C_6^{ij} = \frac{3}{\pi} \int \alpha_i(i\omega)\alpha_j(i\omega)\mathrm{d}\omega \tag{2.43}$$

as the integral over all imaginary frequencies. Now the polarizabilities are expanded as a PADÉ series where only the first term is kept and therefore they can be rewritten as

$$\alpha_i^1(\omega) = \frac{\alpha_i^0}{1 - \left(\frac{\omega}{\eta_i}\right)^2} \tag{2.44}$$

where α_i^0 represents the static polarizability of an atom i. η_i denotes an effective frequency. Inserting the truncated PADE series α_i^1 and α_j^1 into the CASIMIR-POLDER equation (Eq. 2.43) yields the LONDON's formula

$$C_6^{ij} = \frac{3}{2}\frac{\eta_i\eta_j}{\eta_i + \eta_j}\alpha_i^0\alpha_j^0 \tag{2.45}$$

For two atoms of the same type $\eta_i = \eta_j$ and $\alpha_i^0 = \alpha_j^0$ the effective frequency for homonuclear dispersion calculates to

$$\eta_i = \frac{4C_6^{ii}}{3(\alpha_i^0)^2}. \tag{2.46}$$

Now one can find a formula for the dispersion coefficient C_6^{ij} which is only a function of the homonuclear dispersion coefficients C_6^{ii} and C_6^{jj} and the static polarizabilities α_i^0 and α_j^0 which can be found in databases (*61*).

$$C_6^{ij} = \frac{2C_6^{ii}C_6^{jj}}{\frac{\alpha_j^0}{\alpha_i^0}C_6^{ii} + \frac{\alpha_i^0}{\alpha_j^0}C_6^{jj}} \tag{2.47}$$

However, it should be mentioned that the derivation (Eqs. 2.43-2.45) of the formula for the dispersion coefficient Eq. 2.45 merely applies to free isolated atoms, thus a relation has to be found between the dispersion coefficient of a free atom $C_{6,\mathrm{iso}}^{ii}$ and an atom in a solid $C_{6,\mathrm{sol}}^{ii}$. To do so, one can employ the direct proportionality between polarizability α and volume of an atom proposed by BRINCK *et al.* (*62*) $V = k\alpha$ where k denotes the proportionality constant between the quantities. This immediately yields the relation

$$\frac{k^i_{\text{sol}}\alpha^i_{\text{sol}}}{k^i_{\text{iso}}\alpha^i_{\text{iso}}} = \frac{V^i_{\text{sol}}}{V^i_{\text{iso}}} \tag{2.48}$$

between the polarizabilities of an atom i in a solid and as an isolated atom. However to compute the effective volume of an atom in a solid (V^i_{sol} e. g. for an atom i), one has to know the charge density of the atom in a solid $\rho^i_{\text{sol}}(\vec{r})$. Now let $\rho^i_{\text{iso}}(\vec{r})$ denote the charge density of an isolated atom of the same species as atom i. Thus the isolated volume V^i_{iso} can be written as

$$V^i_{\text{iso}} = \int \vec{r}^3 \rho^i_{\text{iso}}(\vec{r})\mathrm{d}\vec{r} \tag{2.49}$$

$$V^i_{\text{sol}} = \int \vec{r}^3 \rho^i_{\text{sol}}(\vec{r})\mathrm{d}\vec{r} \tag{2.50}$$

Although it is trivial to calculate V^i_{iso}, it is not so for V^i_{sol} since ρ^i_{sol} is not known.

2.3.4.1 Hirshfeld partitioning

As the KS theory yields the charge density $\rho(\vec{r})$ for the whole system, Hirshfeld (*63*) came up with a method to dissect the charge density into atomic contributions, such that

$$\rho(\vec{r}) = \sum_i^N \rho^i_{\text{sol}}(\vec{r}) \tag{2.51}$$

where N is the number of atoms in the system under consideration. Employing Hirshfeld's method consequently provides the atomic charge density contributions $\rho^i_{\text{sol}}(\vec{r})$ which are necessary for computing the effective volumes V^i_{sol}, and further on the effective dispersion coefficients, $C^{ii}_{6,\text{sol}}$.

To obtain the atomic charge densities $\rho^i_{\text{sol}}(\vec{r})$ consider again a system with N atoms and charge density $\rho(\vec{r})$ as well as a fictions system (Hirshfeld named this fictitious system the *promolecule* or *procrystal*) with a charge density described by the sum of the charge densities of N isolated atoms at the same positions.

$$\rho_{\text{iso}}(\vec{r}) = \sum_i^N \rho^i_{\text{iso}}(\vec{r}) \tag{2.52}$$

As the next step a sharing function $w(\vec{r})$ for each atom is introduced in the form of

$$w_i(\vec{r}) = \frac{\rho^i_{\text{iso}}(\vec{r})}{\rho_{\text{iso}}(\vec{r})} \tag{2.53}$$

and consequently describes the relative share of the charge density of an atom i in the *promolecule/procrystal* charge density $\rho_{\text{iso}}(\vec{r})$. Then HIRSHFELD simply suggests to define the charge density of an atom i in a bonded state in a solid as

$$\rho^i_{\text{sol}}(\vec{r}) = w_i(\vec{r})\rho(\vec{r}) \tag{2.54}$$

and thus dissects the charge density system into overlapping and continuous atom distributions such that Eq. 2.51 holds true.

By employing HIRSHFELD partitioning Eq. 2.48 can be rewritten to (*59*)

$$\frac{k^i_{\text{sol}}\alpha^i_{\text{sol}}}{k^i_{\text{iso}}\alpha^i_{\text{iso}}} = \frac{V^i_{\text{sol}}}{V^i_{\text{iso}}} = \frac{\int \vec{r}^3 w_i(\vec{r})\rho(\vec{r})\mathrm{d}\vec{r}}{\int \vec{r}^3 \rho_{\text{iso}}(\vec{r})\mathrm{d}\vec{r}} \tag{2.55}$$

and therefore yields a relation between the charge density and polarizability, where $w_i(\vec{r})$ denotes the HIRSHFELD weighting function (Eq. 2.53), $\rho(\vec{r})$ the actual charge density as obtained from the KS-DFT and $\rho_{iso}(\vec{r})$ the charge density of the *promolecule/procrystal* as defined in Eq. 2.52. Finally, by combining all previously derived relations from Eqs. 2.45, 2.46 and 2.55, TKATCHENKO and SCHÄFFLER arrive at the final relation between tabulated homonuclear dispersion coefficients for isolated atoms $C^{ii}_{6,\text{iso}}$ and the corresponding effective coefficients $C^{ii}_{6,\text{eff}}$ as

$$C^{ii}_{6,\text{eff}} = \underbrace{\frac{\eta^i_{\text{sol}}}{\eta^i_{\text{iso}}}\left(\frac{k^i_{\text{iso}}}{k^i_{\text{sol}}}\right)^2}_{\approx 1}\left(\frac{V^i_{\text{sol}}}{V^i_{\text{iso}}}\right)^2 C^{ii}_{6,\text{iso}} = \left(\frac{\int \vec{r}^3 w_i(\vec{r})\rho(\vec{r})\mathrm{d}\vec{r}}{\int \vec{r}^3 \rho_{\text{iso}}(\vec{r})\mathrm{d}\vec{r}}\right)^2 C^{ii}_{6,\text{iso}} \tag{2.56}$$

Furthermore, they prove empirically that the approximation $\frac{\eta^i_{\text{sol}}}{\eta^i_{\text{iso}}}\left(\frac{k^i_{\text{iso}}}{k^i_{\text{sol}}}\right)^2 \approx 1$ holds true for a large variety of molecules except for very small ones, e.g, the hydrogen molecule. In summary it can be stated that the TKATCHENKO-SCHÄFFLER method is formally identical to the DFT-D2 method since it considers only pair interactions for the correction of the KS total energy. Nevertheless, it drastically reduces empiricism at the cost that the approximation for the dispersion coefficient (Eq. 2.56) yields relatively big errors (up to 44% for the H_2 molecule) (*59*) for small molecules. Furthermore, when it comes to describing the structures

and energetics of ionic solids, the theory fails too. However, Bučko *et al.* could show that by employing a modified version of HIRSHFELD partitioning one can solve this problem (*64*, *65*).

2.3.5 Tkatchenko-Schäffler method with Self-consistent screening

Although TKATCHENKO-SCHÄFFLER van der Waals (TS-vdW) correction provides a clean ab-initio method, there are still some phenomena which are not taken into account in this method. At first long-range electrostatic screening effects beyond the range of atomic charge densities are not considered. Secondly, if an atom is built in a large molecule or a solid its dipole fluctuations differ drastically from those of an isolated free atom. The reason for this is that dipole fluctuations are not only influenced by the local environment but also by the electrostatic interaction of distant dipoles. (*66*). Therefore Tkatchenko *et al.* proposed a method where classical electrodynamics is employed to extend TS-vdW (*66*). Starting from the self-consistent screening equation (see App. A sec. A.1)

$$\alpha_i^{SCS}(\omega) = \alpha_i(\omega) - \alpha_i(\omega) \sum_{j \neq i} \mathcal{T}_{ij} \alpha_i^{SCS}(\omega) \tag{2.57}$$

where $\mathcal{T}_{ij}$ is the dipole-dipole interaction tensor (see Sec. A.1.4) and $\alpha_i(\omega)$ the approximated frequency-dependent polarizability as defined in Eq. 2.44. After obtaining $\alpha_i^{SCS}(\omega)$ from Eq. 2.57 the dispersion coefficients $C_{6,SCS}^{ii}$ are evaluated by plugging $\alpha_i^{SCS}(\omega)$ into the CASIMIR-POLDER integral (Eq. 2.43). The characteristic excitation frequency is again the same as in simple TS-vdW method (Eq. 2.46). The method works the same as TS-vdW just with the modified parameters $C_{6,SCS}^{ii}$, $\alpha_i^{SCS}(\omega)$ and R_{0i}^{SCS} where R_{0i}^{SCS} is then the rescaled van-der-Waals radius, which is given by

$$R_{0i}^{SCS} = \left(\frac{\alpha_i^{SCS}}{\alpha_i} \right)^{\frac{1}{3}} R_{0i}. \tag{2.58}$$

This method is still computationally efficient and useful if polarizable atoms and molecules are studied (*67*).

2.3.6 Density-dependent energy correction (dDsC) dispersion correction

Using the second order perturbation theory, BECKE and JOHNSON derived a formalism for the dispersion interaction by analyzing the position-dependent dipole moment of the

exchange hole (*68–70*). Based on this model, STEINMANN and CORMINBOEUF introduced a correction (*71*, *72*) which is formally similar to DFT-D2 (Eq. 2.59)(*67*)

$$E_{disp} = -\sum_{i}^{N-1}\sum_{j>i}^{N} \frac{C_{2n}^{ij}}{r_{ij}^{2n}} f_{damp,2n}(r_{ij} \underbrace{b(x)}_{\text{Eq. 2.61}}). \tag{2.59}$$

However, it uses a different damping function $f_{damp,2n}(r_{ij}b)$ in a form proposed by TANG(*73*)

$$f_{damp,2n}(x)1 - e^{x}\sum_{k=0}^{2n}\frac{x^k}{k!} \tag{2.60}$$

where $2n$ is the correction order (6, 8 or 10). All physical quantities are contained in the damping factor $b(x)$ which is given as

$$b(x) = \frac{2b_{ij,asym}}{e^{a_0 \cdot x} + 1} \tag{2.61}$$

where a_0 is a fitted parameter which controls short-range behaviour of the damping function. The model parameter $b_{ij,asym}$ is estimated from the atomic polarizabilities and is computed by the rule of BÖHM and AHLRICHS (*74*) as

$$\begin{aligned} b_{ij,asym} &= 2\frac{b_{ii,asym} \times b_{jj,asym}}{b_{ii,asym} + b_{jj,asym}} \times b_{jj,asym} \\ b_{jj,asym} &= b_0\sqrt{2I_i}\underbrace{\sqrt[3]{\frac{V_{\text{iso}}^i}{V_{\text{eff}}^i}}}_{\frac{1}{\alpha^i}} \end{aligned} \tag{2.62}$$

where I_i denotes the ionization energy of the i$^{\text{th}}$ atom. As Eq. 2.62 shows the polarizability is again estimated using the linear relationship with the volume as it is done in the TKATCHENKO-SCHÄFFLER method in Eq. 2.55. Consequently, the dDsC method calculates all necessary physical properties from ab-initio data without empirical data input. The formulas for the dispersion coefficients are not stated here since more theoretical background would be necessary for a sufficient explanation. The interested reader is directed to BECKES's paper (*69*). The x parameter for $b(x)$ (Eq. 2.61) is suggested in the original paper as

$$x = \left| q_{ij} + q_{ji} - \frac{(Z_i - N_i)(Z_j - N_j)}{r_{ij}} \right| \frac{N_i + N_j}{N_i N_j} \tag{2.63}$$

where N_i is the effective HIRSHFELD charge contribution of atom i as defined in Eq. 2.54 q_{ij} is an overlap term representing folding of the HIRSHFELD the weighting functions (Eq.

2.53) of the atoms i and j

$$N_i = \int \rho^i_{\mathrm{sol}}(\vec{r})\mathrm{d}\vec{r} = \int w_i(\vec{r})\rho(\vec{r})\mathrm{d}\vec{r} \tag{2.64}$$

$$q_{ji} = \int w_j(\vec{r})\rho^i_{\mathrm{sol}}(\vec{r})\mathrm{d}\vec{r} = \int w_j(\vec{r})w_i(\vec{r})\rho(\vec{r})\mathrm{d}\vec{r} \tag{2.65}$$

As seen in the previous equations, the dDsC method is an advanced full ab-initio method which also considers the local chemical environment of an atom. All physical quantities such as charge N_i (Eq. 2.64), overlap charge q_{ji} (Eq. 2.65), dispersion coefficients $C^{ij}_{6,\mathrm{sol}}$ and polarizability α_i (Eq. 2.55) are solely functions of the charge density itself. The dDsC has been intensively studied and verified (*75*) and it has been successfully applied (*76*).

Chapter 3

Results and discussion

3.1 Calculation & Analysis

3.1.1 DFT calculation setup

All quantum-mechanical calculations were carried out with the **V**ienna **A**b-initio **S**imulation **P**ackage (VASP) (*77*, *78*). The functional used for approximating the exchange and correlation, was Perdew-Burke-Ernzerhof parametrized generalised gradient approximation (PBE-GGA) (*45*). The projector augmented wave method (PAW)(*79*) enabled pseudopotentials described electron-ion interactions. The plane-wave cutoff energy for the basis set was tested for a convergence in a combination with the Monkhorst-Pack (*80*) k-mesh of the Brillouin zone.

3.1.1.1 Convergence criteria

The general energy convergence criteria for the calculation is < 0.1 eV/atom. To ensure the accuracy throughout all calculations, convergence tests were performed by varying cutoff energy (`ENCUT` from 300 to 1200) and k-mesh density (automatic density from 30 to 90) for the unit cells of graphene and graphite. For all calculations containing only hydrogen atoms, an energy cutoff of 600 eV was found to be sufficient, whereas for all other calculations containing carbon atoms, a higher cutoff energy of 1000 eV is needed. Furthermore, as a standard convergence criterion for all calculations energy criteria of 10^{-6} eV (`EDIFF=1E-6`) for the self-consistent electronic loop and 10^{-4} eV (`EDIFFG=1E-4`) for the ionic steps used. The k-meshes for the individual structures can be found in Tab. 3.2

3.1.2 Van-der-Waals correction

To find the most appropriate van-der-Waals correction method for simulations of carbon nanostructures, a small benchmark test was performed. Unit cells of graphene, graphite and diamond structures with experimental lattice parameters were relaxed both with and without fixed unit cell volume (`ISIF = 3/4`) by additionally applying all possible van-der-Waals corrections. Tab. 3.1 shows the result of the benchmark where `ISIF=4` rows represent the calculations with fixed cell volume. The first line shows the resulting lattice parameter, the second line the relative error in % compared to the corresponding literature value. When it comes to choosing the van-der-Waals correction method the greatest focus lies on the graphite c parameter since the grahpite interplanar bonds are van-der-Waals type bonds. Examining which of the available correction methods yields results closest to the experimental parameters best, the Tkatchenko-Schäffler (DFT-TS) was chosen.

3.1.3 Preparation and evaluation

The necessary input files containig unit cell information were obtained from *materialsproject.com* (*81*) to ensure that reasonable structures are at the beginning of our studies. Further processing was done with Python scripting, by heavily using the *SciPy* (*82*) as well as the *pymatgen* (*83*) package as an interface between Python and VASP. All pictures of structural models which appear in this thesis were created with the *VESTA* software package (*84*).

3.2 Single species interaction potential

Before focusing on the adsorption of the hydrogen molecule on various carbon structures, we aimed for the single species interaction potentials of hydrogen, sp^2 bonded (graphene) and sp^3 bonded (diamond) carbon. All calculated data was fitted with common analytical forms of interaction potentials to examine if they can reasonably describe the interaction.

3.2.1 Fitting interatomic potentials

There is a big variety of analytical forms of pair potentials which describe the interaction of two isolated atoms. We focused only on the most common potentials to estimate how well they can describe hydrogen-hydrogen and carbon-carbon bonds. All fitting routines were written in *Python* by employing *SciPy*'s fitting procedures. Interatomic potentials play a vital role in MD simulations, thus the used analytic potentials are presented here

	None IVDW=0	D2 IVDW=10	D3 IVDW=11	D3-BJ IVDW=12	TS IVDW=20	TS + SCS IVDW=21	MBD IVDW=202	dDsC IVDW=4
graphite (c = 6.708 Å)								
ISIF=4	6.762 0.811	6.727 0.281	6.741 0.493	6.732 0.360	6.757 0.731	6.760 0.780	6.747 0.589	6.739 0.471
ISIF=3	7.978 18.936	6.447 3.891	6.952 3.638	6.709 0.016	6.708 0.006	6.710 0.032	6.743 0.530	6.707 0.008
graphite (a = 2.470 Å)								
ISIF=4	2.460 0.047	2.467 0.217	2.464 0.111	2.466 0.180	2.461 0.148	2.460 0.005	2.463 0.029	2.465 0.063
ISIF=3	2.467 0.218	2.463 0.067	2.466 0.194	2.466 0.179	2.460 0.248	2.460 0.057	2.461 0.048	2.455 0.024
graphene (a = 2.470 Å)								
ISIF=4	2.467 0.252	2.467 0.249	2.467 0.236	2.467 0.218	2.464 0.134	2.465 0.137	2.464 0.120	2.459 0.088
ISIF=3	2.467 0.243	2.467 0.240	2.467 0.228	2.466 0.211	2.465 0.138	2.465 0.140	2.464 0.126	2.459 0.084
diamond (a = 2.470 Å)								
ISIF=4	3.575 0.000	3.575 0.000	3.575 0.000	3.575 0.000	3.575 0.000	3.575 0.000	3.575 0.000	3.575 0.000
ISIF=3	3.572 0.065	3.564 0.300	3.564 0.288	3.558 0.473	3.553 0.591	3.554 0.579	3.560 0.421	3.552 0.618

Table 3.1: van-der-Waals correction benchmark results

3.2.1.1 Lennard-Jones potential

One of the earliest interatomic potentials was suggested by Lennard-Jones in 1924 (*85*). The Lennard-Jones potential is composed of a 12^{th} order repulsion term and a 6^{th} order attraction term which is derived from the London's formula (Eq. 2.35) and is therefore usually used to describe the interactions between noble-gas atoms. Two parameters, namely ε which denotes the depth of the potential well, and σ representing the root ($V_{\text{LJ}}(\sigma) = 0$) of the interaction function, parametrize the potential. From Eq. 3.1 one can obtain the equilibrium bond distance as $r_m = \sqrt[6]{2}\sigma$. The potential is usually written in the following form:

System	Structure	Cell dimensions [$\AA$]	Angles [°]	Supercell	k-mesh	mesh type
H_2		$a = b = c = 10$	$\alpha = \beta = \gamma = 90$		$1 \times 1 \times 1$	Gamma
Diamond	A4 conventional	$a = b = c = 2.323$	$\alpha = \beta = \gamma = 90$		$7 \times 7 \times 7$	Monkhorst-Pack
Graphene		$a = b = 2.47, c = 25.0$	$\alpha = \beta = 90, \gamma = 120$		$25 \times 25 \times 1$	Gamma
Graphene	vacancy	$a = b = 12.35, c = 25.0$	$\alpha = \beta = 90, \gamma = 120$	$5 \times 5 \times 1$	$5 \times 5 \times 1$	Gamma
Graphene	vacancy	$a = b = 12.35, c = 25.0$	$\alpha = \beta = 90, \gamma = 120$	$5 \times 5 \times 1$	$5 \times 5 \times 1$	Gamma
Graphene	Stone-Wales	$a = b = 12.35, c = 25.0$	$\alpha = \beta = 90, \gamma = 120$	$5 \times 5 \times 1$	$5 \times 5 \times 1$	Gamma
CNT	$n = 3, m = 3$	$a = b = 24.068, c = 2.459$	$\alpha = \beta = \gamma = 90$		$1 \times 1 \times 32$	Monkhorst-Pack
CNT	$n = 3, m = 3$	$a = b = 24.068, c = 9.838$	$\alpha = \beta = \gamma = 90$	$1 \times 1 \times 4$	$1 \times 1 \times 8$	Monkhorst-Pack
CNT	$n = 6, m = 6$	$a = b = 28.136, c = 2.459$	$\alpha = \beta = \gamma = 90$		$1 \times 1 \times 32$	Monkhorst-Pack
CNT	$n = 6, m = 6$	$a = b = 28.136, c = 9.838$	$\alpha = \beta = \gamma = 90$	$1 \times 1 \times 4$	$1 \times 1 \times 8$	Monkhorst-Pack
CNT	$n = 9, m = 9$	$a = b = 32.204, c = 2.459$	$\alpha = \beta = \gamma = 90$		$1 \times 1 \times 32$	Monkhorst-Pack
CNT	$n = 9, m = 9$	$a = b = 32.204, c = 9.838$	$\alpha = \beta = \gamma = 90$	$1 \times 1 \times 4$	$1 \times 1 \times 8$	Monkhorst-Pack
CNT	$n = 12, m = 12$	$a = b = 36.272, c = 2.459$	$\alpha = \beta = \gamma = 90$		$1 \times 1 \times 32$	Monkhorst-Pack
CNT	$n = 12, m = 12$	$a = b = 36.272, c = 9.838$	$\alpha = \beta = \gamma = 90$	$1 \times 1 \times 4$	$1 \times 1 \times 8$	Monkhorst-Pack
CNT	$n = 5, m = 0$	$a = b = 23.914, c = 4.26$	$\alpha = \beta = \gamma = 90$		$1 \times 1 \times 16$	Monkhorst-Pack
CNT	$n = 5, m = 0$	$a = b = 23.914, c = 8.52$	$\alpha = \beta = \gamma = 90$	$1 \times 1 \times 2$	$1 \times 1 \times 8$	Monkhorst-Pack
CNT	$n = 11, m = 0$	$a = b = 28.611, c = 4.26$	$\alpha = \beta = \gamma = 90$		$1 \times 1 \times 16$	Monkhorst-Pack
CNT	$n = 11, m = 0$	$a = b = 28.611, c = 8.52$	$\alpha = \beta = \gamma = 90$	$1 \times 1 \times 2$	$1 \times 1 \times 8$	Monkhorst-Pack
CNT	$n = 16, m = 0$	$a = b = 32.526, c = 4.26$	$\alpha = \beta = \gamma = 90$		$1 \times 1 \times 16$	Monkhorst-Pack
CNT	$n = 16, m = 0$	$a = b = 32.526, c = 8.52$	$\alpha = \beta = \gamma = 90$	$1 \times 1 \times 2$	$1 \times 1 \times 8$	Monkhorst-Pack
CNT	$n = 21, m = 0$	$a = b = 36.441, c = 4.26$	$\alpha = \beta = \gamma = 90$		$1 \times 1 \times 16$	Monkhorst-Pack
CNT	$n = 21, m = 0$	$a = b = 36.441, c = 8.52$	$\alpha = \beta = \gamma = 90$	$1 \times 1 \times 2$	$1 \times 1 \times 8$	Monkhorst-Pack

Table 3.2: Simulation cell lattice parameters as well as the corresponding k-meshes

$$V_{\mathrm{LJ}}(r) = 4\varepsilon \left[\left(\frac{\sigma}{r}\right)^{12} - \left(\frac{\sigma}{r}\right)^{6} \right] \tag{3.1}$$

In the following sections we use a modified LENNARD-JONES potential to fit the interaction energies, which adds an additional fitting parameter r_0 and is given by

$$V_{\mathrm{LJ}}(r) = 4\varepsilon \left[\left(\frac{\sigma}{r + r_0}\right)^{12} - \left(\frac{\sigma}{r + r_0}\right)^{6} \right]. \tag{3.2}$$

3.2.1.2 Buckingham potential

BUCKINGHAM aimed for simplifying the LENNARD-JONES potential (*86*). He therefore kept the 6^{th} order van-der-Waals attraction term, but for the PAULI repulsion he suggests an exponential term

$$V_{\mathrm{Buckingham}}(r) = \gamma \left[\exp\left(\frac{-r}{r_0}\right) - \left(\frac{r_0}{r}\right)^{6} \right] \tag{3.3}$$

where γ and r_0 represent fitting parameters.

3.2.1.3 Morse potential

The interatomic potential proposed by MORSE (*87*) already in 1929 utilizes exponential functions. The MORSE potential proved to be successful for metals MD simulations metals. The analytical form has three fitting

$$V_{\mathrm{Morse}}(r) = E_D \left(e^{-2\alpha(r-r_0)} - 2e^{-\alpha(r-r_0)} \right) \tag{3.4}$$

parameters where E_D is the dissociation energy or the depth of the potential well, r_0 is the equilibrium bond length and α is often referred to as a stiffness parameter. With increasing α the flanks of the potential well increase in steepness which consequently leads to a stiffer bond.

3.2.2 Hydrogen-hydrogen bond

3.2.2.1 Calculational setup

To ensure that the hydrogen molecules do not interact due to periodic boundary conditions, a big simulation cell of $10 \times 10 \times 10$ Å was used. The hydrogen molecule was positioned

in the middle (molecule center: [0.5, 0.5, 0.5]) of the cell whereas the molecule axis pointed into x-direction. Fig 3.1 shows a sample configuration.

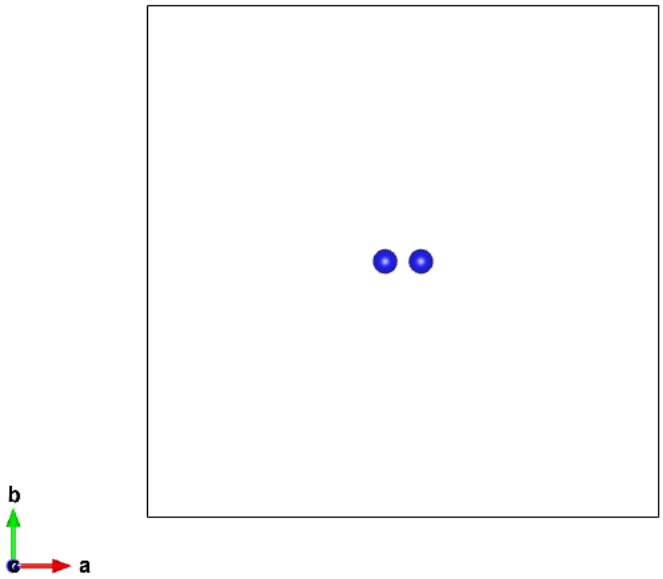

Figure 3.1: Simulation box for the hydrogen potential curve

The spacing between the two hydrogen atoms ranges from 0.1 Å to 1.4 Å. Since those calculations are relatively cheap, a dense distance sampling was employed, especially around the equilibrium distance of 0.75 eV. Around the potential minimum the distance spacing is 0.005 Å ($r = 0.7 - 0.8$ Å), 0.01 Å ($r = 0.6 - 0.8$ Å and $r = 0.8 - 0.9$ Å) and 0.02 Å for all other regimes. All the curves were calculated without van-der-Waals correction as well with DFT-D3 and DFT-TS correction method.

3.2.2.2 Results

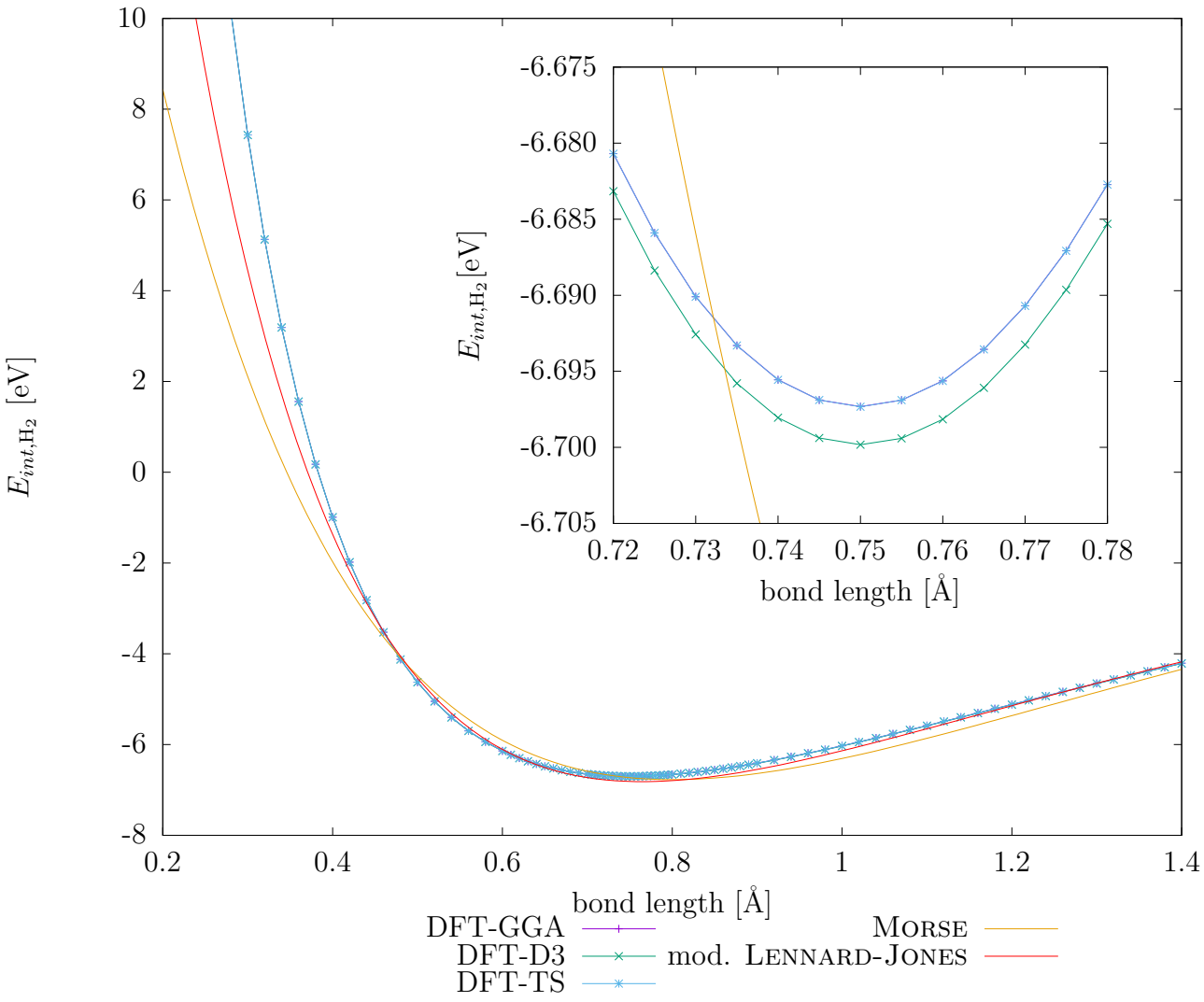

Figure 3.2: H_2 interaction potential fitted with modified Lennard-Jones (Eq. 3.2) potential ($\varepsilon = 6.818$ eV, $\sigma = 3.216$ Å, $r_0 = 2.845$ Å) and Morse potential ($E_D = 6.7732$ eV, $\alpha = 1.525$, $r_0 = 0.8005$ Å)

Figure 3.2 shows the calculated energies. The bonding energy was calculated by subtracting two times the total energy of an isolated hydrogen atom ($E_{tot,H} = -0.565$ eV) from the calculated total energy $E_{int,H_2} = E_{tot,H_2} - 2 \cdot E_{tot,H}$. $E_{tot,H}$ was obtained from a separate

calculation where a single hydrogen atom was placed in the simulation box shown in Fig. 3.1. Fitting the calculated data with a cubic spline and analysing it, yields the same bonding distances for all calculated curves ($r_{min,\text{standard}} = r_{min,\text{DFT-D3}} = r_{min,\text{DFT-TS}} = 0.749$ Å). Also, the DFT-TS and the curve without van-der-Waals corrections shows no significant difference over the whole graph. Only the DFT-D3 interaction curve ist shifted by $\approx 2.5\,\text{meV}$ at the interaction minimum. Although at the first look one can get the impression that the analytical potentials fit the interaction potential well, the minima of the modified LENNARD-JONES and the MORSE potentials lie at $r_{min,\text{mod. LJ}} = 0.764$ Å and $r_{min,\text{Morse}} = 0.8007$ Å respectively, which is relatively far away. The minima of the fits differ by $\approx 75.93\,\text{meV}$ (modified LENNARD-JONES) and $\approx 120.27\,\text{meV}$ (MORSE) from the calculated value.

3.2.3 Carbon sp^2 bond

3.2.3.1 Calculational setup

To calculate the interaction energy per bond the a and b lattice parameters of the graphene unit cell were increased step by step, resulting in a sampling of the bondlength from 0.927 Å to 5.704 Å. As in the previous subsection the densest mesh is around the miniumum. Therefore, the bondlength is given by $a_{C-C} = \dfrac{a}{2\sqrt{3}}$ where a ist the lattice parameter of the unit cell. The interaction energy per bond is therefore given as

$$E_{int,\text{sp}^2} = \frac{E_{tot,\text{graphene}} - N E_{tot,\text{C}}}{\underbrace{\frac{3}{2}N}_{\text{number of bonds}}} \tag{3.5}$$

where $E_{tot,\text{graphene}}$ is the calculate total energy of the stretched graphene cell, $E_{tot,\text{C}}$ the energy of an isolated carbon atom and N the number of carbon atoms in the simulation box. Since every atoms is bonded with three others, the factor $\frac{3}{2}$ has to be introduced in the denominator. Figure 3.3 shows the graphene unit cell which was used for the calculations. The energy cutoff was `ENCUT=1000` eV the corresponding k-mesh is tabulated in Tab. 3.2.

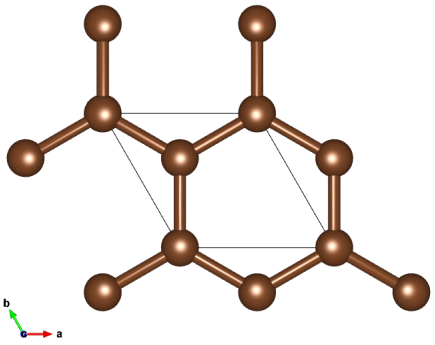

Figure 3.3: Structural model of a graphene unit cell

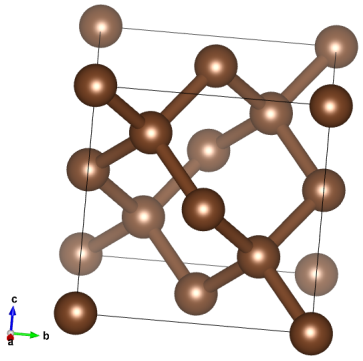

Figure 3.4: Structural model of an A4 diamond conventional unit cell

3.2.3.2 Results

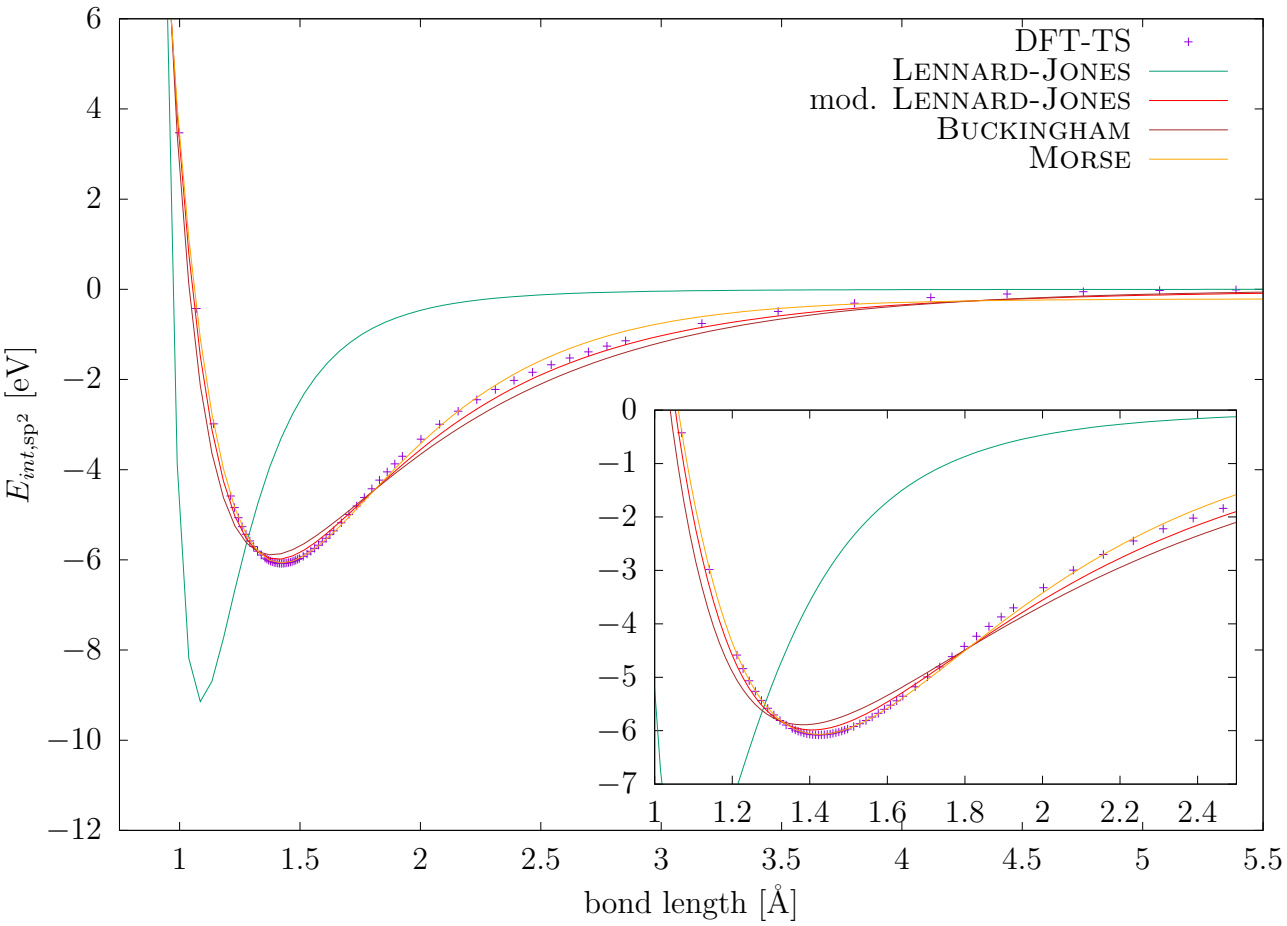

Figure 3.5: sp^2 interaction potential fitted with Lennard-Jones potential ($\varepsilon = 9.143$ eV, $\sigma = 0.969\,\text{Å}$, $r_0 = \sqrt[6]{2}\sigma = 1.088\,\text{Å}$), modified Lennard-Jones potential ($\varepsilon = 5.986$ eV, $\sigma = 2.878\,\text{Å}$, $r_0 = 1.825\,\text{Å}$), Morse potential ($E_D = 6.068$ eV, $\alpha = 1.935$, $r_0 = 1.4236\,\text{Å}$), and Buckingham potential ($\gamma = -41.298$ eV, $r_0 = 0.848$ eV)

The purple crosses in Fig. 3.5 represent the calculated sp^2 bonding energies with DFT-TS correction. Fitting a cubic spline yields a bondlength $r_{min,\text{DFT-TS}} = 1.4229\,\text{Å}$ and a bonding energy of $E_{\text{bond}} = -6.079$ eV/bond. Again, the standard analytical potentials do not describe the interaction very well as shown in Tab. 3.3 due to a shift of the minima position and value. Nevertheless the Morse potential gives the best description overall (around the minimum and for great values of the bond length). However as Fig. 3.5 shows, all fits fail to model the

regime between 2.5 and 3.5 Å. ΔE_{bond} in Tab. 3.3 and Tab. 3.4 represents the difference of the bonding energies at their minima $\Delta E_{\text{bond}} = E_{\text{bond,DFT-TS}}(r_{min,\text{DFT-TS}}) - E_{\text{bond,fit}}(r_{min,\text{fit}})$ in meV.

Potential	r_{min} [Å]	E_{bond} [eV]	ΔE_{bond} [meV]
Lennard-Jones	1.088	-9.143	3064.045
mod. Lennard-Jones	1.405	-5.987	92.355
Buckingham	1.382	-5.889	189.555
Morse	1.423	-6.068	10.619

Table 3.3: Position and value of the minima of the analytic potentials fitted to the C sp^2 interaction potential as well as their deviation from the calculated DFT data

3.2.4 Carbon sp^3 bond

3.2.4.1 Calculational setup

The methodological aprroach to calculate the interaction energy of the sp^3 bonded carbon is analogical to that of the sp^2 bonded case (Subsec. 3.2.3.1). As a starting point, A4 conventional cubic diamond cell with four atoms was used as illustrated in Fig. 3.4. However a different amount of bonds per unit cell has to be considered since each carbon atom is bonded with four neighbors. Similarly to the previous section the interaction energy thus can be computed by

$$E_{int,\text{sp}^3} = \frac{E_{tot,\text{diamond}} - N E_{tot,\text{C}}}{\underbrace{2N}_{\text{number of bonds}}} \tag{3.6}$$

where $E_{tot,\text{diamond}}$ is the calculated energy of the cell. The range of sampled bond lengths starts from 1.006 Å to 5.158 Å, with the densest grid around the minimum. The energy cutoff was set to `ENCUT=1000` eV the corresponding k-mesh is tabulated in Tab. 3.2.

3.2.4.2 Results

Analyzing a cubic spline fitted to the calculated DFT-TS interaction energy (purple crosses) in Fig. 3.6 yields the minimum at $r_{min,\text{DFT-TS}} = 1.5386$ Å with a bonding energy $E_{\text{bond}} = -4.5709$ eV/bond which is $\approx 75\%$ of the value of sp^2 bonded carbon. Tab. 3.4 shows the position and the bonding energy for the analytical potentials. Again, none of the fits describes the interaction well (Fig. 3.6), where again (as for the sp^2 bond) the Morse

potential yields the best results. The fits do not only have different values at the minimum but also shift the position of the minima as Tab. 3.4 shows.

Potential	r_{min} [Å]	E_{bond} [eV]	ΔE_{bond} [meV]
Lennard-Jones	1.182	-6.819	2248.112
mod. Lennard-Jones	1.524	-4.515	55.788
Buckingham	1.506	-4.428	143.388
Morse	1.544	-4.579	8.112

Table 3.4: Position and value of the minima of the analytical potentials fitted to the sp^3 interaction potential as well as their deviation from calculated DFT-TS data

Figure 3.6 shows the the calculated DFT-TS data (pruple crosses) as well as the fitted interatomic potentials. The detailed graph in the lower right corner of Fig. 3.6 shows nicely that the fits deviate from the calculated curve. Especially at medium ranges between 2.0 $\mathring{A}$ and 4.5 A all fitted curves fail to describe the calculated data.

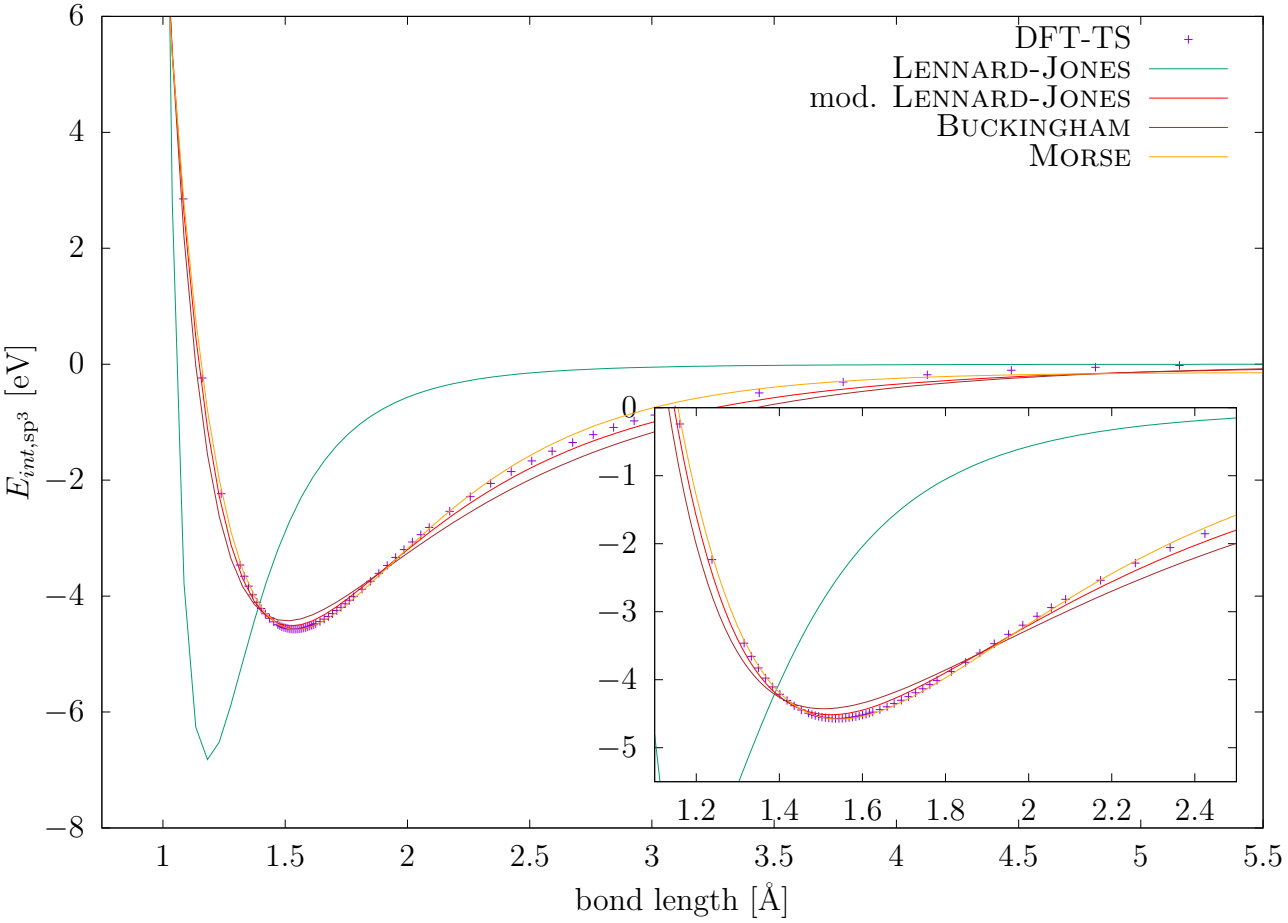

Figure 3.6: sp^3 interaction potential fitted with Lennard-Jones potential ($\varepsilon = 6.819$ eV, $\sigma = 1.053\,\text{Å}$, $r_0 = \sqrt[6]{2}\sigma = 1.182\,\text{Å}$), modified Lennard-Jones potential ($\varepsilon = 4.515$ eV, $\sigma = 3.077\,\text{Å}$, $r_0 = 1.929\,\text{Å}$), Morse potential ($E_D = 4.579$ eV, $\alpha = 1.806$, $r_0 = 1.544\,\text{Å}$), and Buckingham potential ($\gamma = -31.0457$ eV, $r_0 = 0.924\,\text{Å}$)

Figure 3.7 shows the calculated DFT-TS curves for sp^2 and sp^3 bonds. One can see that sp^2 is the stiffer bond due to a shorter bond distance and a deeper minimum, however at around 2 Å bondlength the curves begin to converge.

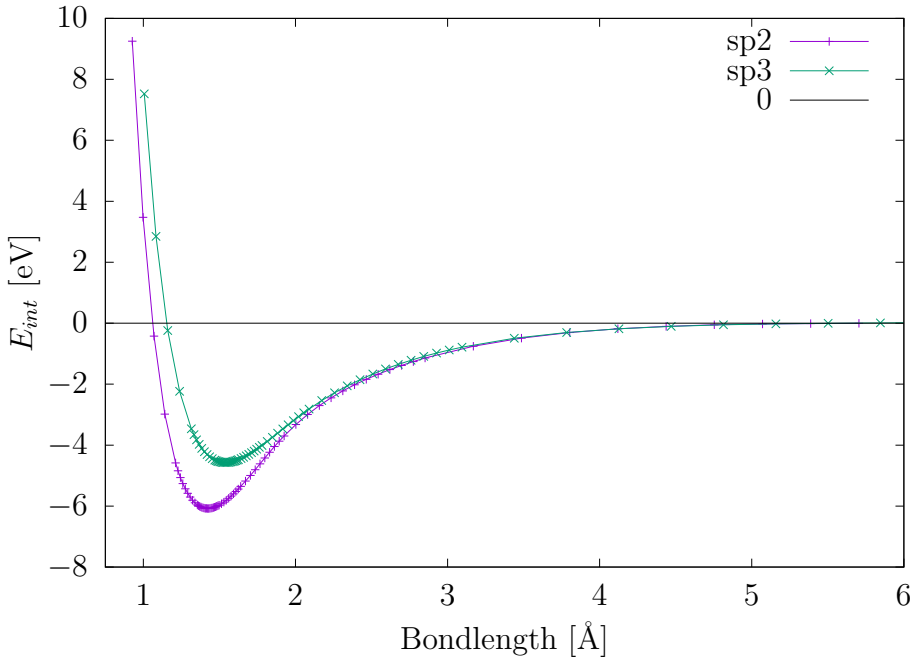

Figure 3.7: Comparison of the DFT-TS calculated sp^2 and sp^3 interaction potentials

3.3 Interaction with the hydrogen molecule

The focus of this thesis is the interaction of the hydrogen molecule with carbon nanostructures, thus the interaction with graphene, defected graphene and carbon nanotubes will be presented in this *main* result section .

3.3.1 Graphene

3.3.1.1 Calculational setup

For modelling the interaction between hydrogen molecule and a graphene plane, a $5 \times 5 \times 1$ graphene supercell (dimensions can be found in Tab. 3.2) was created to ensure the hydrogen molecule does not interact with one of its periodic images. In the c direction (spacing between periodic images of the graphene planes) a lattice parameter of 25 Å was chosen to ensure that also for big separations (> 10 Å) between the graphene plane and the hydrogen molecule no interactions with the periodic image can occur. Because the length of the cell in a and b direction as indicated in Fig. 3.8 is 12.35 Å possible interaction of the H_2 molecule with its

periodic image is minimised. The graphene unitcell was obtained from *materialsproject.com* and the ionic positions were relaxed with fixed volume (`ISIF=2`).

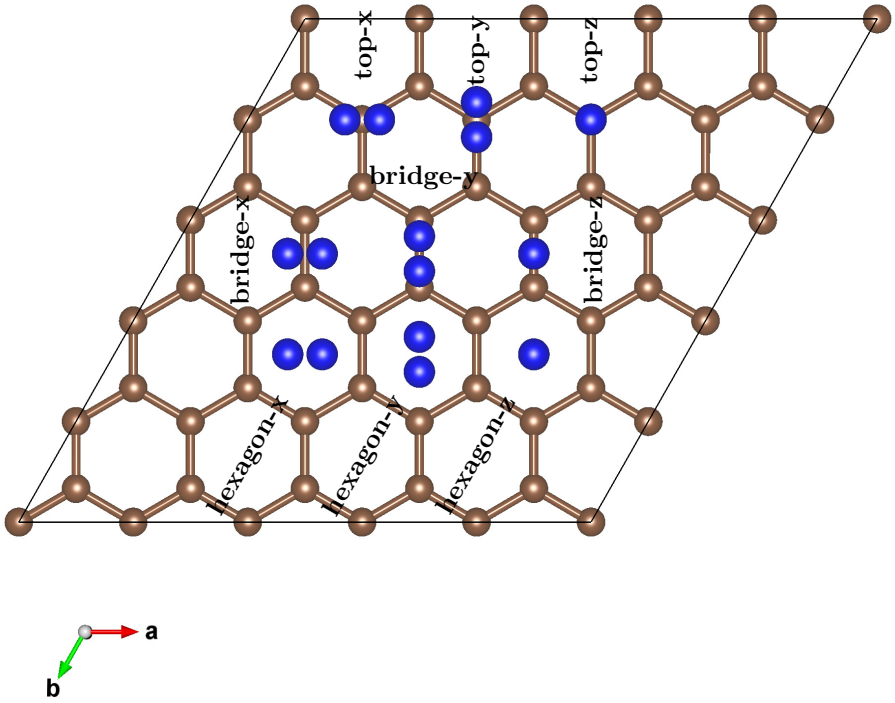

Figure 3.8: Hydrogen molecule placed on the individual adsorption sites (top, bridge, hexagon)

As Figure 3.8 illustrates there are three high symmetry sites where the hydrogen molecule can be placed. Directly above a carbon atom, hereafter referred to as *top* site, above a bond between two carbon atoms (*bridge* site) and above the center of a hexagon (*hexagon* site). Furthermore, we have considered three alignments for each site resulting in 9 configurations in total. The x direction as illustrated in Fig. 3.8 is parallel to the a lattice vector, the y direction is perpendicular to it, while the z direction is parallel to the c lattice vector of the simulation cell.

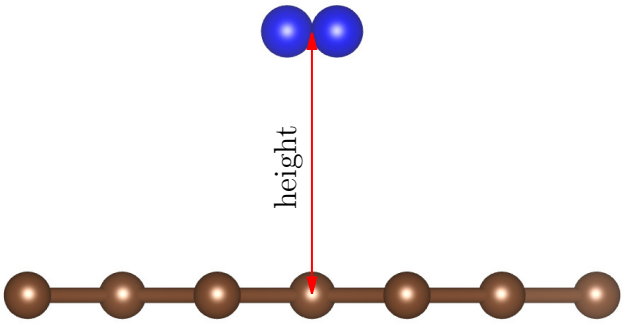

Figure 3.9: Definition of the height above the graphene plane. The height is always calculated between the graphene plane and the center of the hydrogen molecule

For each configuration shown in Fig. 3.8, a cell was set up with the hydrogen molecule 3.275 Å above the graphene plane. The height of the hydrogen molecule is calculated between its center and the graphene sheet as illustrated in Fig. 3.9. After placing the hydrogen molecule above the graphene sheet an ionic relaxation with constant cell volume and shape (`ISIF=2`) was performed to find the local asdorption minimum, such that the hydrogen atoms find their equilibrium positions, while the carbon atom positions were fixed. All calculations were again performed with the DFT-TS correction (`IVDW=20`) and a cutoff energy of `ENCUT=1000` eV.

After finishing the ionic relaxation, the hydrogen molecule was shifted along the c axis so that the height of the molecule center above the graphene plane is sampled from ≈ 2 Å to 12.5 Å (half height of the simulation cell). For each of those height steps the total energy is calculated for a fixed geometry (`NSW=0`) and used for the evaluation of the interaction energy $E_{int,\text{graphene+H}_2}$

$$E_{int,\text{graphene+H}_2} = E_{tot,\text{graphene+H}_2} - E_{tot,\text{graphene}} - E_{tot,\text{H}_2}(h_{min,\text{DFT-TS}}) \tag{3.7}$$

3.3.1.2 Results

For each adsorption curve and every hydrogen molecule arrangement the interaction energy $E_{int,\text{graphene+H}_2}$ between the hydrogen molecule and the graphene plane was calculated by using the value $E_{tot,\text{graphene}} = -463.974$ eV (The value was obtained from a separate calculation of the plain graphene plane with the same cutoff `ENCUT=1000` eV and k-mesh as shown in Tab. 3.2) and $E_{tot,\text{H}_2}(h_{min,\text{DFT-TS}} = 0.749\,\text{Å}) = -6.772$ eV for the bonded hydrogen

molecule energy. The resulting curves are plotted in Fig. 3.10. The *hexagon-x* and *hexagon-y* curves show the deepest adsorption minima and are completely indentical although the configurations are not in terms of symmetry. A cubic spline was fitted to all curve shown in Fig. 3.10 and the location and depth of the minima (adsorption energy) were evaluated and are given in Tab. 3.5. The interaction energy is approaching zero for great spacing between the molecule an the grahpene plane.

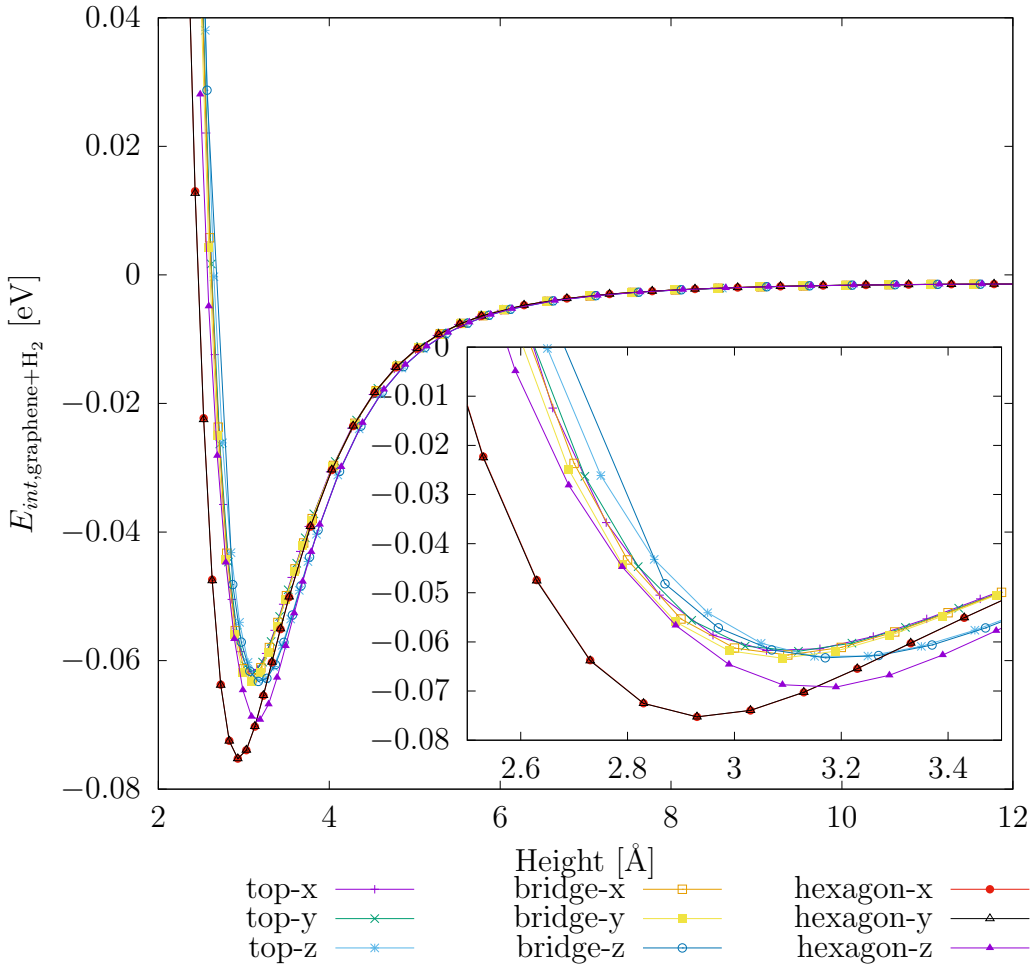

Figure 3.10: Interaction energy (Eq. 3.7) plotted for each of the hydrogen molecule arrangements (Fig. 3.8)

Site	Alignment	h_{ads} [Å]	E_{ads} [eV]	$E_{ads}(h = h_{max})$ [eV]
top	x	3.095	-0.062	-0.0014
	y	3.101	-0.062	-0.0014
	z	3.196	-0.062	-0.0014
bridge	x	3.089	-0.063	-0.0014
	y	3.084	-0.063	-0.0014
	z	3.194	-0.063	-0.0014
hexagon	x	2.941	-0.075	-0.0014
	y	2.940	-0.075	-0.0014
	z	3.153	-0.069	-0.0014

Table 3.5: Equilibrium adsorption height and adsorption energy for the individual molecule configurations as illustrated in Fig. 3.8.

Figure 3.10 and Tab. 3.5 clearly show that the strongest adsorption energy is obtained for the hydrogen molecule sitting within a hexagon. The *hexagon-x* and *hexagon-y* configurations have a slightly lower adsorption energy than the *hexagon-z* site (≈ 6 meV) which was already shown by Okamoto that x and y configuration are preferred (*88*). Previous works showed that the z alingment in energetically more favourable (*22*, *23*). The same energy difference of ≈ 6 meV can be observed between the *hexagon-z* site and all other adsorption configurations. Furthermore, it is remarkable that all *top* configurations show the same adsorption energy although the minima correspond to different adsorption heights. Similarly the same is true for all *bridge* configuration. The adsorption minimima (difference between smallest h_{ads} for *hexagon-y* and largest for *bridge-z*) lie within a range of 0.25 Å. The theoretical estimation of the adsorption energies lie within the range between $10 - 60$ meV (*89*, *90*) (since London forces are hard to etimate) which is nevertheless in good agreement with the caclulated data in Tab. 3.5. Furthermore a previous DFT study reports similar values as our calculated data (*24*) while the data in Tab. 3.5 is shifted to more negative values by ≈ 8 meV compared with the results by Krishnan *et al.* (*23*).

3.3.2 Graphene with a vacancy defect

Additionally to perfect graphene, the influence of defects on adsorption is of interest. Thus, a sampling of the adsorption height and energy was performed for the whole supercell. Furthermore, the incluence of the defect on the energy barrier when hydrogen molecule

penetrates the graphene layer was studied. From here on the main focus is set on the *hexagon* since it is energetically the preferential adsorption site.

3.3.2.1 Calculational setup

Adsorption energy and height map After determining the irreducible zone of the $5 \times 5 \times 1$ graphene supercell, which posseses a regular triangular shape, a sampling mesh was defined as illustrated in Fig. 3.11. The relation between the lattice parameters of the sampling mesh $\vec{a}_1'$ and the graphene unit cell lattice vector $\vec{a}_1$ is

$$\vec{a}_1' = \frac{\vec{a}_1}{2\sqrt{3}} \quad \text{and} \quad \vec{a}_2' = \frac{\vec{a}_2}{2\sqrt{3}} \tag{3.8}$$

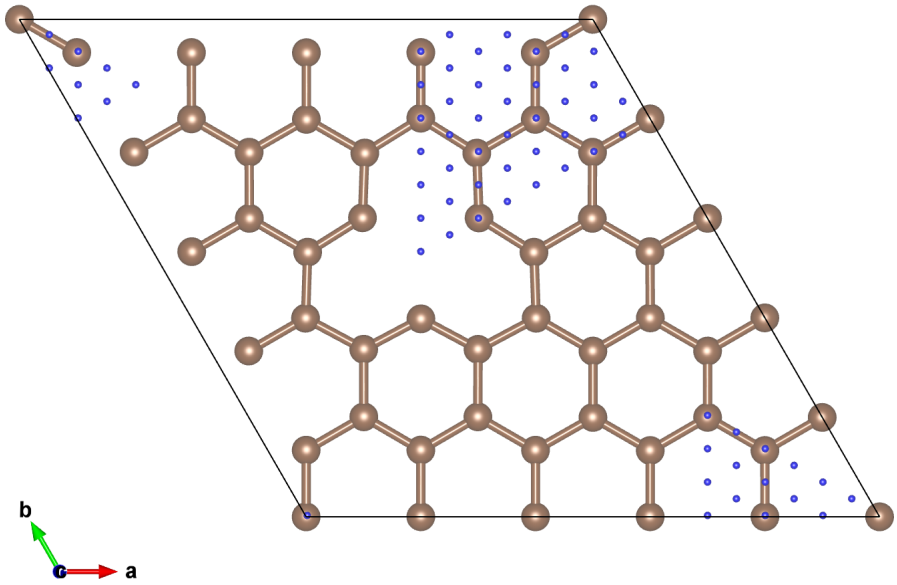

Figure 3.11: Irreducible mesh for sampling the graphene supercell with 66 points.

which yields a trinagle mesh such that along each side of the regular trianglular shaped sampling zone are eleven grid points[1]. (See Fig. 3.11). For each of those grid points described below adsorption height and energy of the hydrogen molecule was estimated.

[1] $66 = \binom{12}{2}$ is the 11^{th} triangle number.

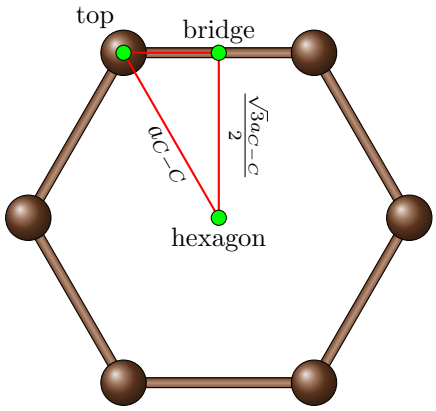

Figure 3.12: Interpolation of the equilibrium adsorption height within a graphene sheet.

First, each point on the mesh grid, the nearest *hexagon*, *bridge* and *top* site are determined, which therefore define a triangle as shown in Fig. 3.12. On this specific triangle the height is interpolated by calculating the weights of barycentric coordinates within the triangle W^{top}, W^{bridge} and W^{hexagon} (*91*) such that

$$W^{\text{top}} + W^{\text{bridge}} + W^{\text{hexagon}} = 1 \tag{3.9}$$

holds true. The estimated height is then given by the inner product of the following vectors:

$$h_{ads}^{\text{int}} = \begin{pmatrix} W^{\text{top}} \\ W^{\text{bridge}} \\ W^{\text{hexagon}} \end{pmatrix} \cdot \begin{pmatrix} h_{ads}^{\text{top}} \\ h_{ads}^{\text{bridge}} \\ h_{ads}^{\text{hexagon}} \end{pmatrix}^{T} \tag{3.10}$$

This interpolated height h_{ads}^{int} is expected to be near the real adsorption height at this grid point, thus serves as a reasonable starting guess. The hydrogen molecule was placed at heights from $h_{ads}^{\text{int}} + 0.3\,\text{Å}$ to $h_{ads}^{\text{int}} - 0.3\,\text{Å}$ with a step of 0.1 $\mathring{A}$ to sample the adsorption minimum. By fitting the energy versus molecule distance curve with a quadratic function, the real equilibrium adsorption height was determined h_{ads}^{real}, subsequently the hydrogen molecule was placed at this position to calculate the final adsorption energy. This results in 528 (66·8) calculations for this cell. The interaction energy was calculated similarly to Eq. 3.7 as

$$E_{int,\text{graphene+H}_2}^{\text{vacancy}} = E_{tot,\text{graphene+H}_2}^{\text{vacancy}} - E_{tot,\text{graphene}}^{\text{vacancy}} - E_{tot,\text{H}_2}(h_{min,\text{DFT-TS}}) \tag{3.11}$$

where $E_{tot,\text{graphene+H}_2}^{\text{vacancy}} = -446.662$ eV is the total energy of a graphene plane with a single vacancy (computed in a separate calculation) and $E_{tot,\text{H}_2}(h_{min,\text{DFT-TS}}) = -6.772$ eV the total energy of the isolated hydrogen molecule. The height shown in Fig. 3.15 is the visualization

of h_{ads}^{real} and corresponding adsorption energy (Fig. 3.16) is the minimum of the interaction energy $E_{ads} = E_{int,\text{graphene+H}_2}^{\text{vacancy}}(h_{ads}^{\text{real}})$ at each point of the grid (Fig. 3.11). All calculations were performed with the DFT-TS correction (`IVDW=20`) and a cutoff energy of `ENCUT=1000` eV in the *hexagon-z* configuration.

Push through of the hydrogen molecule Additionally to the adsorpion energy and height, the influence of the vacancy defect on the adsorption-distance curve throughout the whole cell was studied. Therefore, the hydrogen molecule was not only set in equilibrium height above the grahpene plane, but also pushed through it such that the height (as shown in Fig. 3.9) becomes zero. Furthermore this procedure was repeated for different hexagons in the supercell with increasing distance from the vacancy defect, (marked with **1** in Fig. 3.13). 60 different spacings between the graphene plane and the hydrogen molecule were used to calculate the curves. Around the adsorption minima h_{ads} a step of 0.1 Å was chosen for the range $0 < r < 1.25 h_{ads}$. 0.25 Å for the intermediate range between $\approx 4 - 6$ Å and 0.75 Å for the rest. A Python script was implemented to prepare and evaluate the calculations.

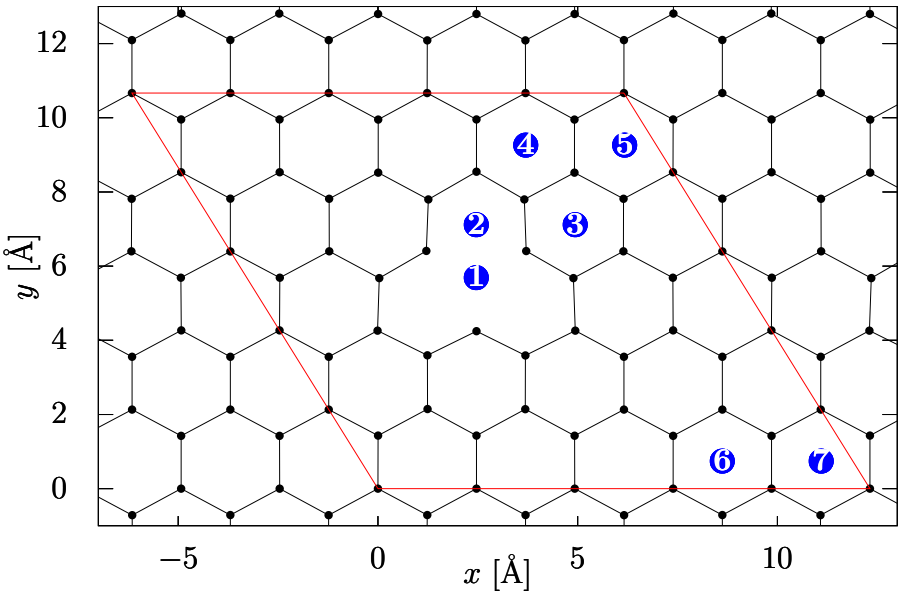

Figure 3.13: Hexagons at which the hydrogen molecule was pushed through the graphene plane. The increasing label numbers represent increasing distance from the vacancy marked with **1**

3.3.2.2 Results

Adsorption energy and height map Figures 3.15 show the location of the adsorption minima or the equilibrium adsorption height of the hydrogen molecule in the z alingment on the whole $5\times5\times1$ graphene supercell (red line). One can observe the largest distances above bonds at the border of the vacancy, which also correspond to the weakest adsorption energy as Fig. 3.16 shows. The center of the defect shows the lowest adsorption height (blue center region in Fig. 3.15) however -63 meV is not the lowest adsorption energy (6 meV higher than on perfect graphene, see Fig. 3.16). The hexagon sites neighboring the vacancy (sites **3** and **4** in Fig. 3.13) show higher adsorption energy, while with the increasing distance from the defect the energy valleys in the hexagons are getting deeper and deeper until the value reaches ≈ -69 meV (Tab. 3.5 and Fig. 3.16), the value on graphene without a defect for more distant hexagons (sites **6** and **7** in Fig. 3.13). Although the adsorption energy, when going away from the defect, reaches the value of perfect graphene, the adsorption height does

not, it remains ($\approx 0.03\,\text{Å}$) above the perfect graphene value. Both Figs. 3.15 and 3.16 clearly illustrate that the vacancy has only a short-ranged influence on the adsorption (especially at the site **3** in Fig. 3.13) while the more distant sites show graphene plane behaviour, which suggests the conclusion that the supercell size is sufficient for studying the vacancy defect.

Push through of the hydrogen molecule The interaction energy versus the molecule height above the graphene plane for all seven *hexagon-z* configurations (see Fig. 3.13) are plotted in Fig. 3.14. The curves were fitted by cubic splines and results are summarized in Tab. 3.6. As already said in the aforementioned paragraph and clearly underpinned by Tab. 3.6 and the detail graph in Fig. 3.14, there is only a weak dependence between the distance to the defect center and the depth of the adsorption minima.

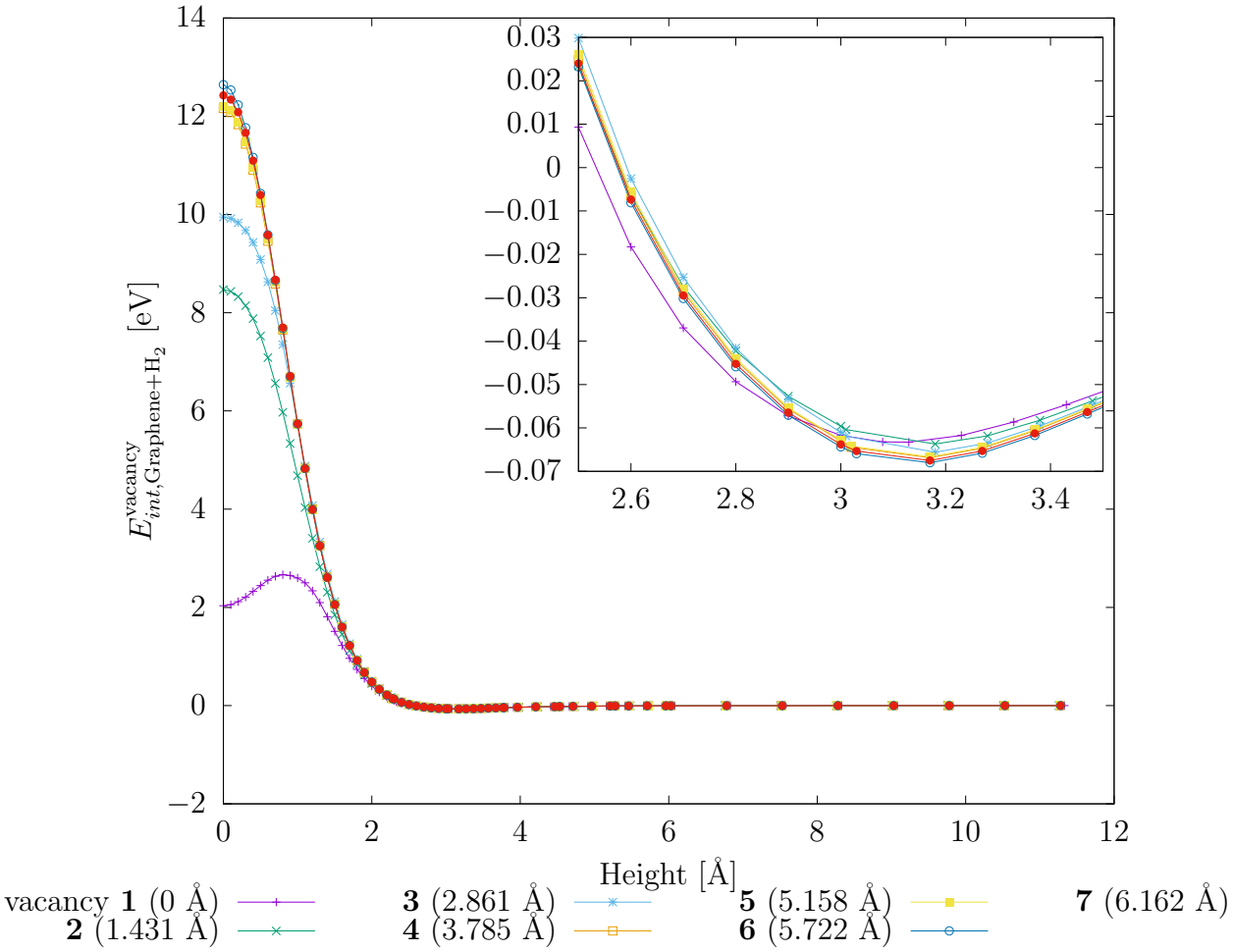

Figure 3.14: $E^{\text{vacancy}}_{int,\text{graphene+H}_2}$ versus separation between hydrogen molecule and graphene plane for seven distinct *hexagon-z* molecule alignment on the supercell as illustrated in Fig. 3.13. The numbers in the parenthesis represent the distance of the site to the vacancy defect

Furthermore Fig. 3.14 clearly shows that the sites far away from the vacancy defect (sites **4**, **5**, **6** and **7**) behave very similary, have very similar adsorption energies and energy barriers. Only sites **2** and **3** show a significant lowering of the energy barrier. However the most interesting curve is the one at the vacancy site itself. One can observe that the curve shape is different from the others and has a local minimum directly when the molecule center is on the graphene plane, with a energy barrier of 2.664 eV. Therefore the vacancy acts as a trap for the hydrogen molecule in the graphene plane.

Site	Distance from the defect [Å]	$E(h = 0)$ [eV]	h_{ads} [Å]	$E_{ads}(h = h_{ads})$ [eV]
1	0.000	2.033	3.110	-0.063
2	1.431	8.470	3.124	-0.064
3	2.861	9.946	3.130	-0.066
4	3.785	12.161	3.118	-0.067
5	5.158	12.205	3.120	-0.067
6	5.722	12.643	3.136	-0.068
7	6.162	12.425	3.139	-0.068

Table 3.6: Distance to the vacancy defect center, height of the energy barrier, position of the adsorption minimum h_{min} as well the adsorption energy E_{ads}, of all seven *hexagon-z* sites as depicted in Fig. 3.13

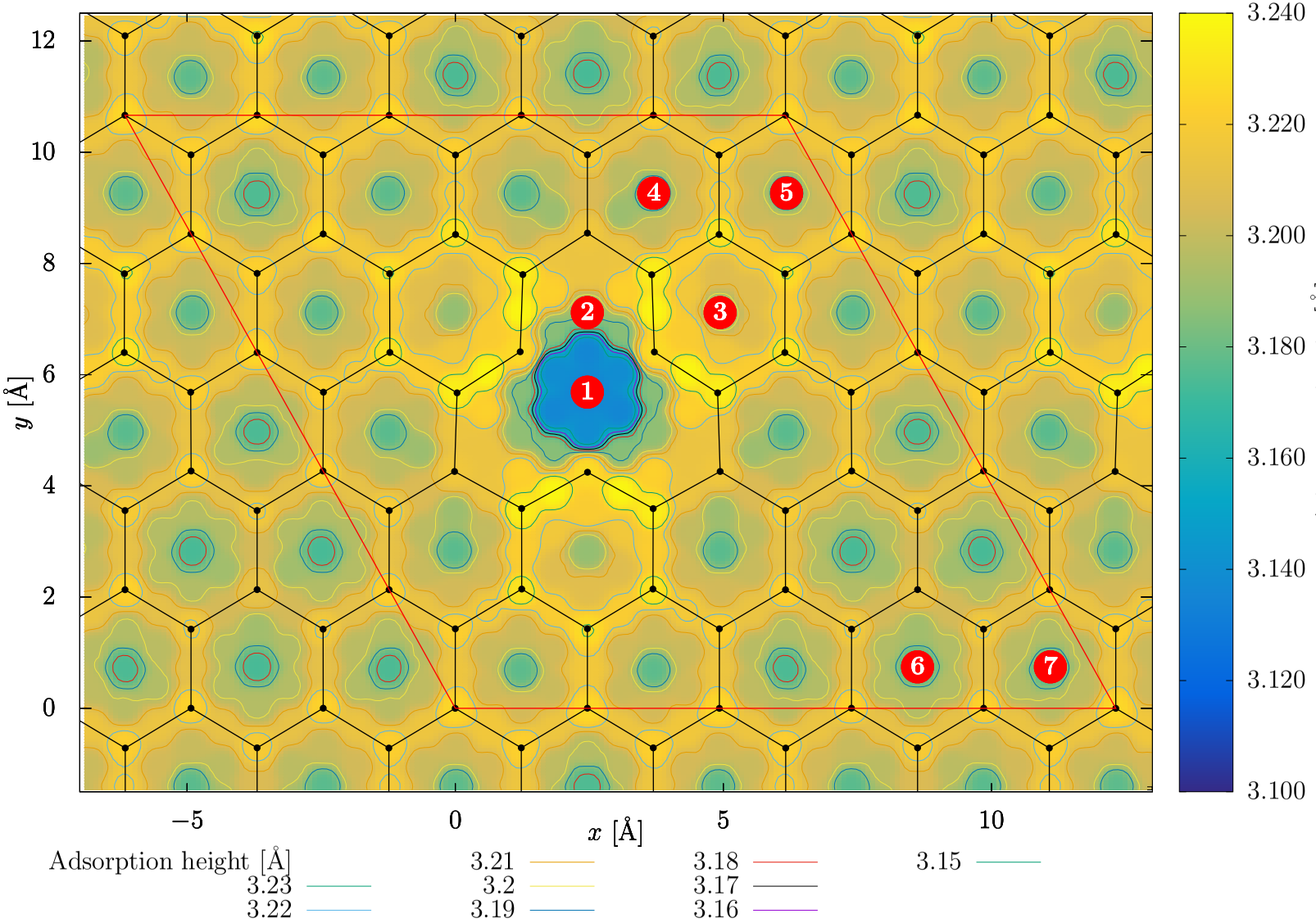

Figure 3.15: Adsoption height on $5 \times 5 \times 1$ graphene supercell with a vacancy

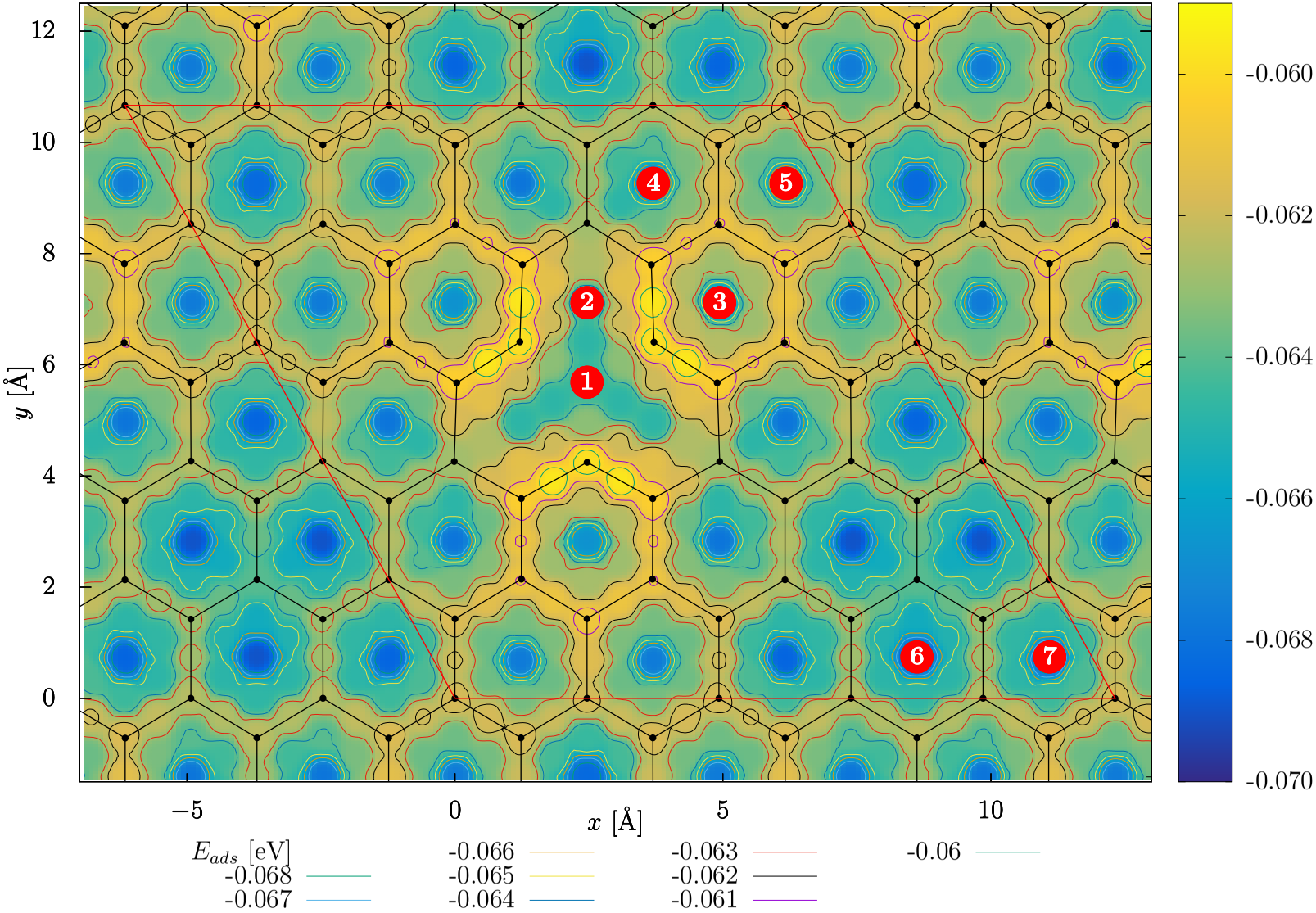

Figure 3.16: Adsoption energy on $5 \times 5 \times 1$ graphene supercell with a vacancy

3.3.3 Graphene with a Stone-Wales defect

The Stone-Wales defect was first observed in 1986 (*92*, *93*) and was described to be two carbon atoms rotated by 90° around the center of their bond. Thus four hexagons become two heptagons and two pentagons. It has also been possible to make the defect visible in experiments using high-resolution transmission electron microscopy (HRTEM) (*94*, *95*). Also the Stone-Wales defect was studied here for its capability to store a hydrogen molecule.

3.3.3.1 Calculational setup

The procedure to create the maps is the same as for the vacancy defect as described in section 3.3.2.1. However, the irreducible zone of the graphene supercell with the Stone-Wales defect is different as shown in Fig. 3.17. Consequently, 110 points were used to sample the relatively large zone.

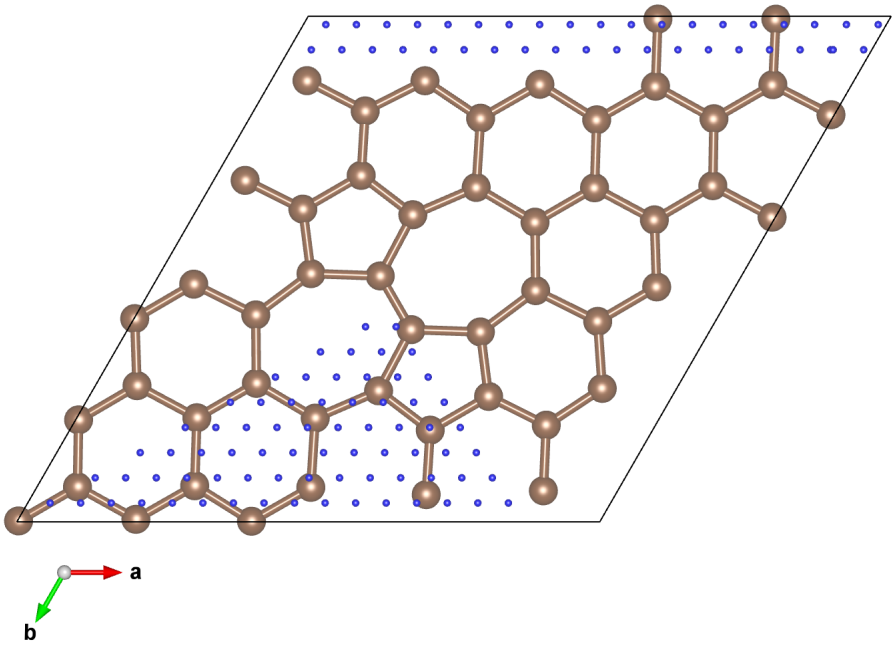

Figure 3.17: Irreducible mesh for sampling the graphene supercell with a Stone-Wales defect using 110 points.

For sampling the vacancy defect, the lattice vectors of the sampling lattice vector were scaled in length but kept parrallel to those of the graphene lattice (Eq. 3.8), whereas here a

rotation of 30° around z axis and a scaling was applied

$$\vec{a}_1' = \frac{1}{3}\tilde{\mathbf{R}}(\phi = 0, \chi = 0, \psi = \pi/6,) \cdot \vec{a}_1 \quad \text{and} \quad \vec{a}_2' = \frac{1}{3}\tilde{\mathbf{R}}(\phi = 0, \chi = 0, \psi = \pi/6,) \cdot \vec{a}_2 \tag{3.12}$$

where $\tilde{\mathbf{R}}$ is the general rotation matrix (Eq. A.29). The reason for the rotation is that also the edges of the vertices of the irreducible zone are then covered with grid points. For each of the lattice points shown in Fig. 3.17, the hydrogen molecule was placed at the calculated interpolated height as described by Eqs. 3.10 , 3.9. In the next step, the hydrogen molecule was placed at heights ranging from $h_{ads}^{\text{int}} + 0.3\,\text{Å}$ to $h_{ads}^{\text{int}} - 0.3\,\text{Å}$ with a step of 0.1 $\mathring{A}$ to sample the adsorption minimum. The interaction energy is calculated analogously to Eq. 3.11

$$E_{int,\text{graphene+H}_2}^{\text{Stone-Wales}} = E_{tot,\text{graphene+H}_2}^{\text{Stone-Wales}} - E_{tot,\text{graphene}}^{\text{Stone-Wales}} - E_{tot,\text{H}_2}(h_{min,\text{DFT-TS}}) \tag{3.13}$$

while $E_{tot,\text{graphene}}^{\text{Stone-Wales}} = -458.541$ eV and $E_{tot,\text{H}_2}(h_{min,\text{DFT-TS}})$ was calculated to -6.772 eV. Using rotation and mirroring symmetry operations, the irreducible mesh was expanded over the whole supercell. The adsorption energy E_{ads} in Tab. 3.7 is defined as the minimum of the interaction energy $E_{ads} = E_{int,\text{graphene+H}_2}^{\text{Stone-Wales}}(h_{ads}^{\text{real}})$.

Push through of the hydrogen molecule The point around which the defect bond is rotated by 90° is hereafter referred to as the center of the STONE-WALES defect. The procedure for the calculation setup is the same as for graphene with vacancy, thus the reader is referred to section 3.3.2.1 for detailed information. The sites at which the H_2 molecule was pushed through the graphene plane are shown in Fig. 3.18

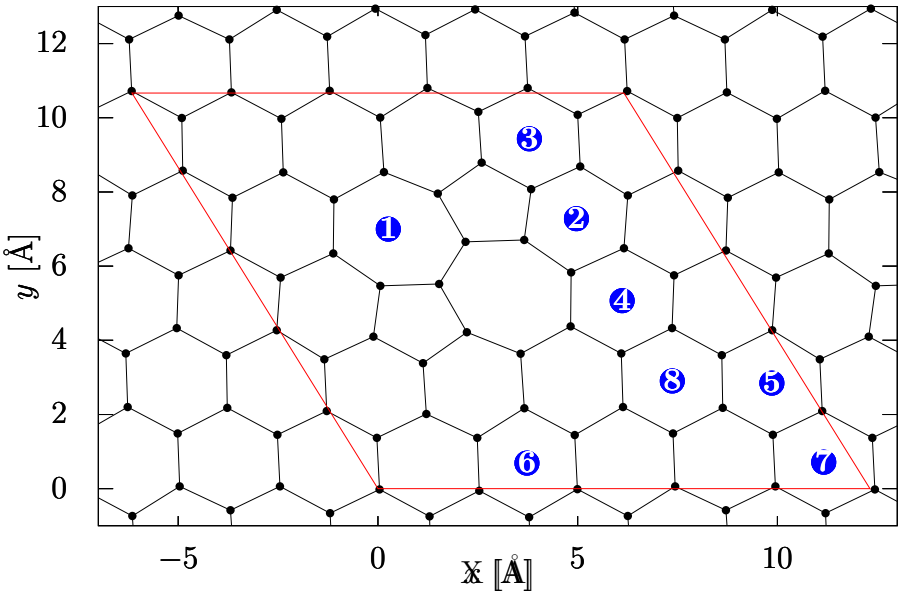

Figure 3.18: Sites at which the hydrogen molecule was put through the graphene plane with STONE-WALES defect. The increasing label numbers represent increasing distance from the Stone-Wales defect.

3.3.3.2 Results

Adsorption energy and height map A closer look to Fig. 3.21 reveals that the STONE-WALES strongly defect incluences its surroudings (hexagons **4**, **6** and **2** in Fig. 3.18) exhibit adsorption energy for the H_2 molecule at the center of the hexagons of $66-67$ meV which is in the range of perfect graphene (69 meV) yet slightly higher. Consider a vector parallel to the rotated, bond directly at the center of the defect. Along this direction, the hexagons neighboring the pentagon adjacent to the defect seem to show similar or even deeper ($69-70$ meV) minima as calculated for perfect graphene (69 meV). Furthermore the pentagons are not favored by the H_2 molecule, while the heptagons show similar adsorption energy values as the hexagons. Yet the fluctuation of the depth of the energy valleys in different interstitial adsorption sites (hexagons, heptagons) is very small $\approx 68-70$ meV over the whole supercell (see Tab. 3.7). Contrary to the vacancy defect which is avoided by the hydrogen molecule, the heptagons offer enough space for the molecule to be absorbed while the pentagons do

not. Comparing Fig. 3.16 and Fig. 3.21 suggests that the STONE-WALES is a less severe deformation since the adsorption minima and equilibrium heights differ less from perfect graphene. Comparing the height maps (Fig. 3.20 and Fig. 3.15) it becomes obvious that, especially around the vacancy defect, the adsorption separation increases more. Nevertheless, both defects seem to have only a short-ranged influence on the adsorption behaviour.

Site	Distance from defect [Å]	$E(h = 0)$ [eV]	h_{ads} [Å]	E_{ads} [eV]
1	1.844	8.319	3.082	-0.069
2	3.330	12.526	3.142	-0.070
3	3.864	12.971	3.143	-0.070
4	4.375	12.019	3.147	-0.068
5	5.465	12.869	3.144	-0.070
6	5.711	12.369	3.146	-0.069
7	6.201	12.971	3.140	-0.071
8	6.361	12.469	3.146	-0.069

Table 3.7: Distance to the STONE-WALES defect center, height of the energy barrier, position of the adsorption minimum h_{min} as well as depth of the adsorption minima E_{ads}, of all eight *hexagon-z* sites as depicted in Fig. 3.18

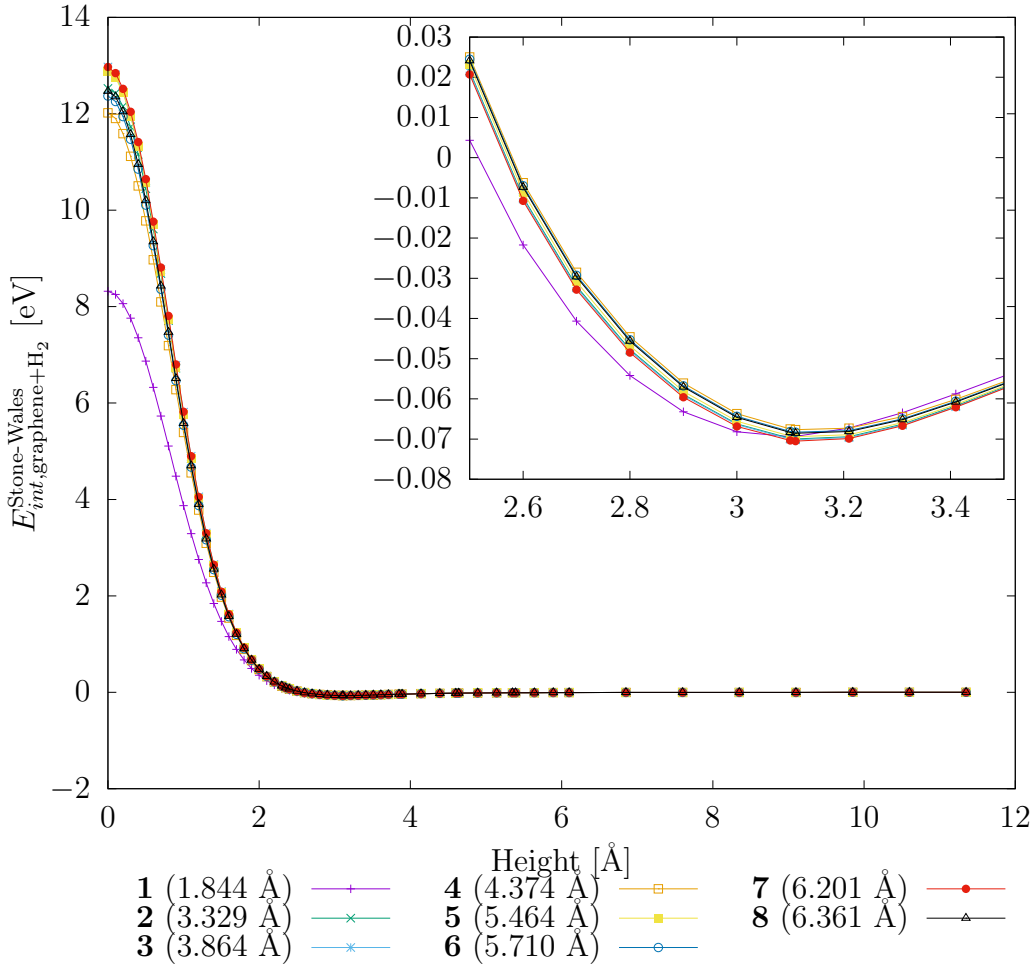

Figure 3.19: $E^{\text{Stone-Wales}}_{int,\text{graphene+H}_2}$ versus separation between hydrogen molecule and graphene plane with STONE-WALES-defect for eight distinct *hexagon-z* molecule configurations on the supercell as illustrated in Fig. 3.18. The numbers in the parenthesis represent the distance of the site to the vacancy defect

Push through of the hydrogen molecule Compared to the vacancy defect, when pushing the H_2 molecule through the plane, Fig. 3.19 clearly shows that for site **1** no local minimum is formed within the heptagon. The energy barrier of 8.319 eV is comparable to that of the adjacent hexagon site next to the vacancy (site **2** in Fig. 3.13). Therefore, in contrast to the vacancy, a STONE-WALES defect cannot act as a trap for the H_2 molecule, being pushed through the graphene. The energy barrier $E_{int}(r = 0)$ with increasing distance converges to a value of $\approx 12.4 - 12.9$ eV which is consistent with the values calculated for the vacancy

defect (see Fig. 3.6). Furthmore, comparing Fig. 3.19 with Fig. 3.14 reveals that the energy barrier converges faster to this limit value than it does for the vacancy defect. Tab. 3.7 and the detailed graph in Fig. 3.19 reveals that the adsorption energies vary only in a range of 3 meV ($0.068 - 0.071$ eV) and thus only slightly differ from perfect the graphene (69 meV).

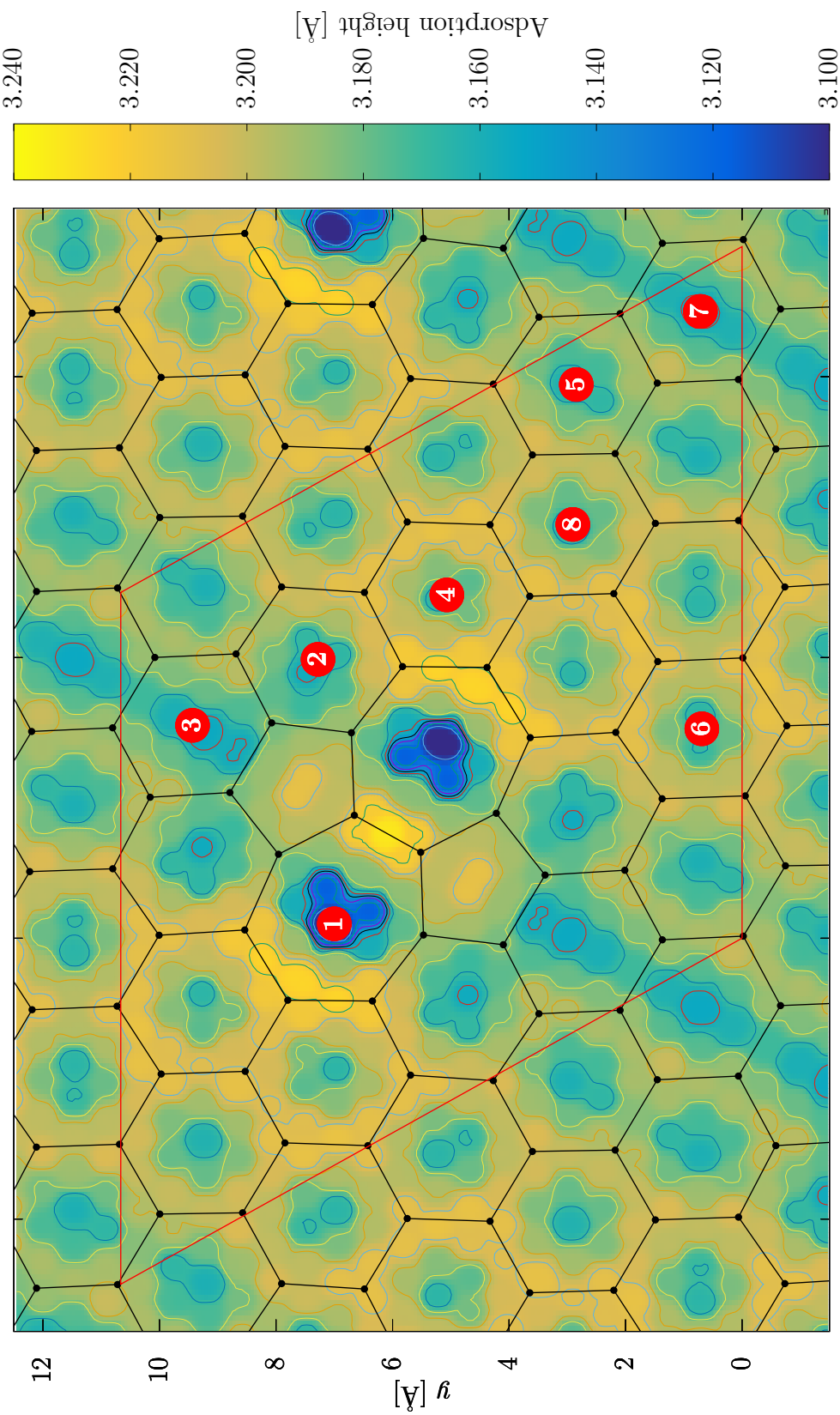

Figure 3.20: Adsoption height on $5 \times 5 \times 1$ Graphene supercell with a Stone-Wales defect

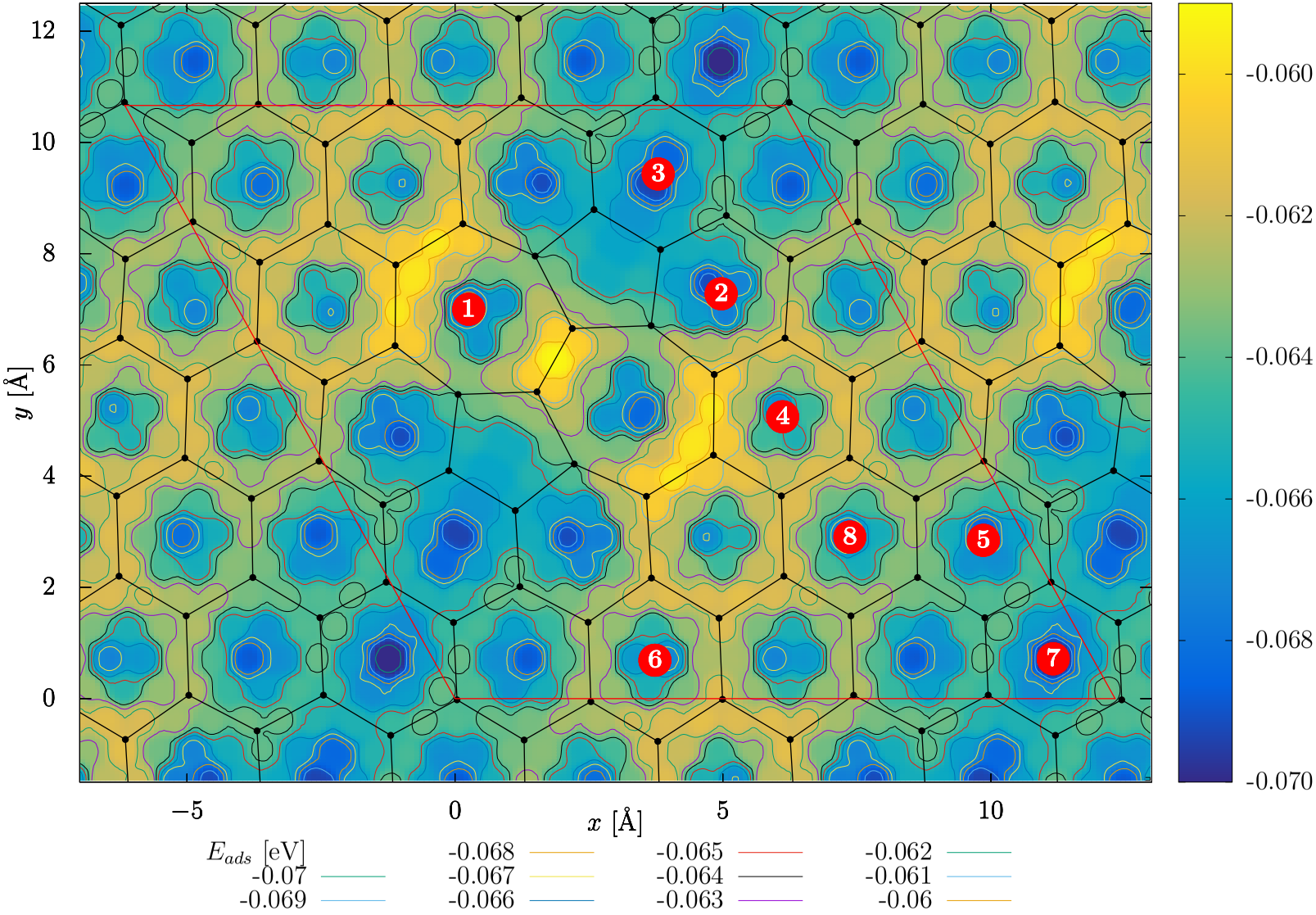

Figure 3.21: Adsoption energy on $5 \times 5 \times 1$ Graphene supercell with a STONE-WALES defect

3.3.4 Carbon-Nanotubes

The following section presents the adsorption energies for all molecule alignments, different carbon nanotube diameters and geometries.

3.3.4.1 Calculational setup

After generating tube unit cells with a *Python* script according to Sec. 2.1.2.1, a buffer vacuum of 20 Å was placed around the tube in the x and y directions (coordinate system as indicated in Fig. 3.22) so that the CNTs do no interact with their periodic images. Four different diameters were choosen for both armchair and zigzag chiralities, such that for each $(n-0)$ zigzag CNT exists a compareable $(n-n)$ armchair counterpart. In the first step, the unit cells of the CNTs were relaxed, because the initially generated tube model refers to a perfect CNT, therefore all atoms lie on the same cylinder. Because of different lengths of zigzag and armchair unit cells (see Tab. 3.2) in the tube axis direction, the number k-points of the Monkhorst-Pack mesh was set to have equal spacing in the reciprocal spacing (Tab. 3.2). For all calculations in this section we used tubes with a length of ≈ 10 Å to avoid interaction of the H_2 molecule with one of its periodic images along the z (tube axis) direction. Parallel to the stacking the relaxed geometry of the unit cell tubes, the resulting charge density was also stacked in the z direction and used as input guess for relaxing the whole tubes, to speed up the convergence of the DFT calculations.

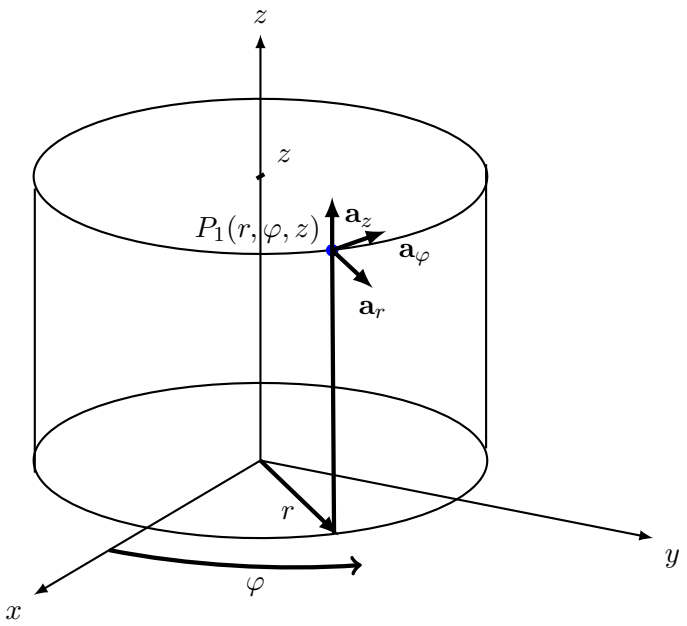

Figure 3.22: Definition of the cylindrical coordinates of a CNT. The cylinder represents the CNT with tube axis along the z direction. The origin is located in the center of the tube. P_1 is an atom on the CNT

The procedure now is principally the same as for calculating the adsorption energies on graphene. However, because a different coordinate system was introduced (Fig. 3.22), it is convenient to employ a different naming of the molecule alignments. The graphene z axis becomes the r axis, the x axis is the same as the CNT tube z axis, and finally the graphene y direction maps on the CNTs φ axis. The calculations of pure CNTs are fast because of their high symmetry. This dramatically changes when placing the H_2 molecule and thus significantly reducing the symmetry. To overcome this problem, a method (implemented in *Python*) was developed to add up two discrete charge density meshes (see Sec. A.2) while translating and rotating them relative to each other. By adding the charge densities of a CNT and the H_2 molecule, a good starting guess for the final charge density can be made, resulting in a significant decrease of the computing time (reduction of up to 75 %). The hydrogen molecule was placed above the CNTs at all sites and alignments, using the corresponding height above the graphene plane as a starting guess, and the hydrogen ion positions were relaxed (`ISIF=2`).

Analogous to the graphene case, the relaxed H_2 molecule geometry was shifted along the r direction to calculate the total energy (while keeping everything (all atom positions) fixed

(`ISIF=0`, `NSW=0`) to finally obtain the interaction energy versus distance curves.

$$E_{int,\mathrm{CNT+H_2}} = E_{tot,\mathrm{CNT+H_2}} - E_{tot,\mathrm{CNT}} - E_{tot,\mathrm{H_2}}(r_{min,\text{DFT-TS}}) \tag{3.14}$$

For $E_{int,\mathrm{CNT+H_2}}$, only the *hexagon-r* position was choosen because previous studies concluded it to be the most favourable adsorption site (*96*).

3.3.4.2 Results

Tab. 3.9 and Figs. 3.23, 3.24 show that the adsorption distance increases with increasing diameter for both *armchair* and *zigzag* and approaches the graphene value. Although the heights in Tab. 3.8 show good agreement with values of Krishnan *et al.* (*23*) again a shift to more negative values of E_{ads} is predicted similarly to the graphene case. However the adsorption energies for *hexagon-r* and *top-r* configuration Tab. 3.9 agree with values calculated by Han *et al.* with DFT-D3 (*97*). However, for both *armchair* (Fig. 3.23) and *zigzag* (Fig. 3.24) the tubes with small diameters show even closer spacing between the tube and the center of the H_2 molecule than graphene, although the adsorption energy is less negative. A closer look on Tabs. 3.9, 3.8 reveals that *zizag* tubes show a slightly lower adsorption energy, than *armchair* tubes. The dependence on the chiralitity, however, could not be observed by Zhou *et al.* (*21*). The discrepancy of h_{ads} and E_{ads} between the *hexagon-r* values in Tabs. 3.8, 3.9 is caused by the evaluation method. (direct optimisation versus the cubic spline fit to $E_{int,\mathrm{CNT+H_2}}$)

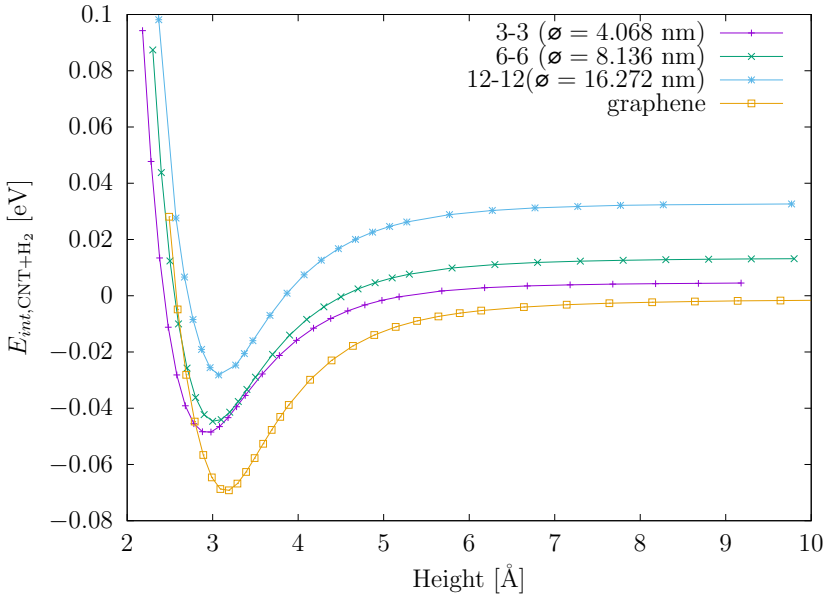

Figure 3.23: $E_{int,\mathrm{CNT+H_2}}$ for three different *armchair* CNTs with different diameters in the *hexagon-r* alignment compared with the corresponding graphene configuration

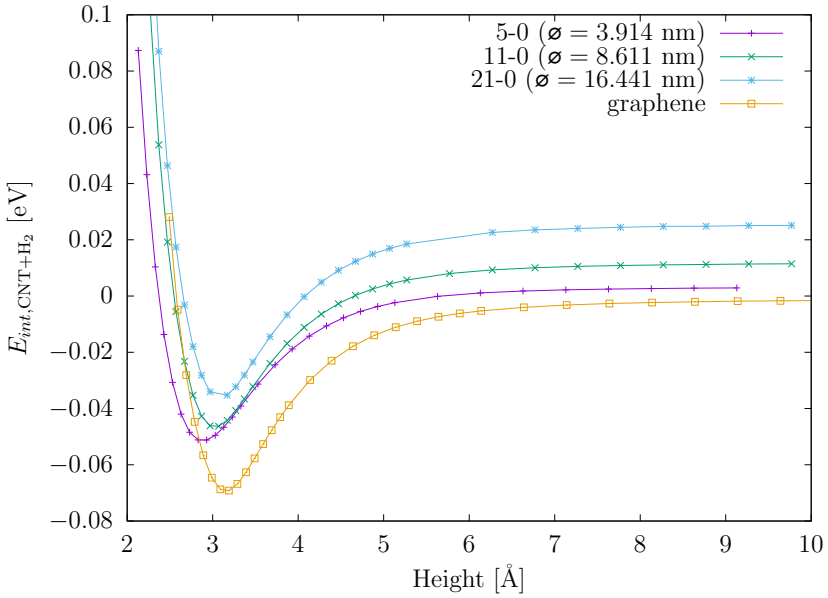

Figure 3.24: $E_{int,\mathrm{CNT+H_2}}$ for three different *zigzag* CNTs with different diameters in *hexagon-r* alignment compared to the corresponding graphene configuration

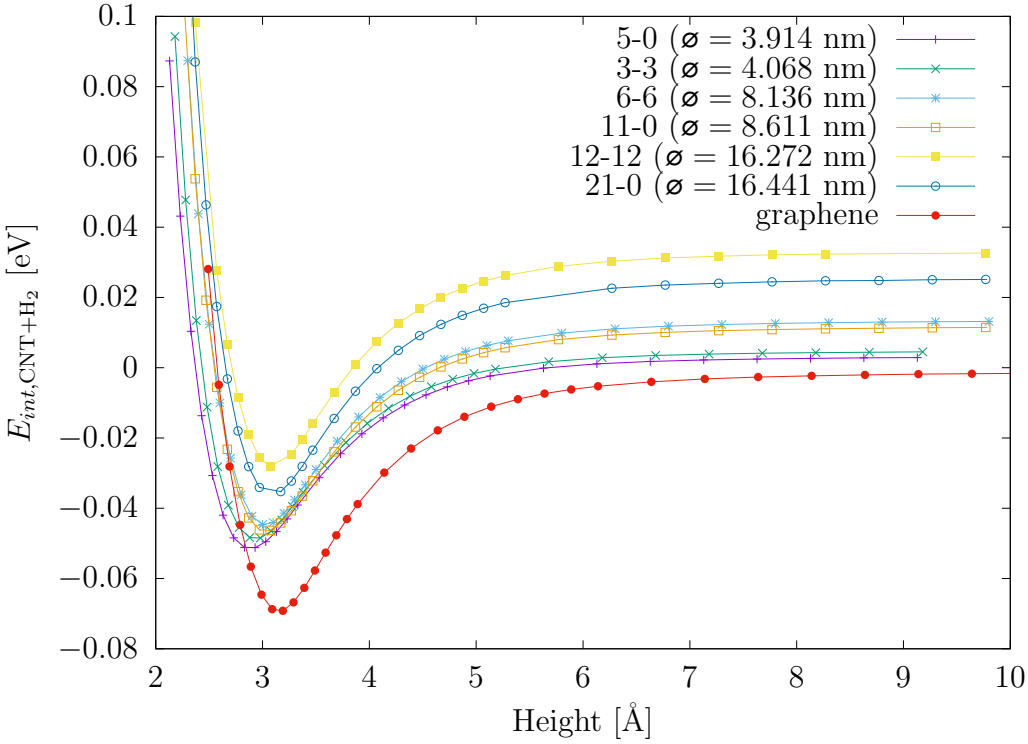

Figure 3.25: $E_{int,\mathrm{CNT+H_2}}$ for three different *zigzag* CNTs and *armchair* with different diameters in the *hexagon-r* alignment compared with the corresponding graphene configuration

With increasing the tube diameter, the adsorption energy E_{ads} decreases, which is contraintuitive since greater tube diameters refer to a more graphene like situation.

$n-m$	Type	⌀[Å]	r_{ads} [Å]	E_{ads} [eV]
5-0	zigzag	3.914	2.881	-0.051
3-3	armchair	4.068	2.933	-0.049
6-6	armchair	8.136	3.026	-0.045
11-0	zigzag	8.611	3.025	-0.047
12-12	armchair	16.272	3.097	-0.028
21-0	zigzag	16.441	3.086	-0.036
Graphene		∞	3.153	-0.069

Table 3.8: Adsorption energy E_{ads} and location of the adsorption minima, calculated by cubic spline interpolation using data from Fig. 3.25 for the H_2 *hexagon-r* alignment

The same trend of decreasing adsorption energy with increasing tube diameter is also underpinned by Tab. 3.9 since the CNT tube columns in Tab. 3.9 are sorted in ascending order by their diameter. Furthermore, the lowest energies, in contrast to graphene, can be observed for the *hexagon-z* alingment which qualitatively contradicts the literature results (*96*, *97*), however fits our own graphene results. Dissociaction of the molecule for the *bridge-φ* configuration could be observed, so that no reasonable result could be obtained.

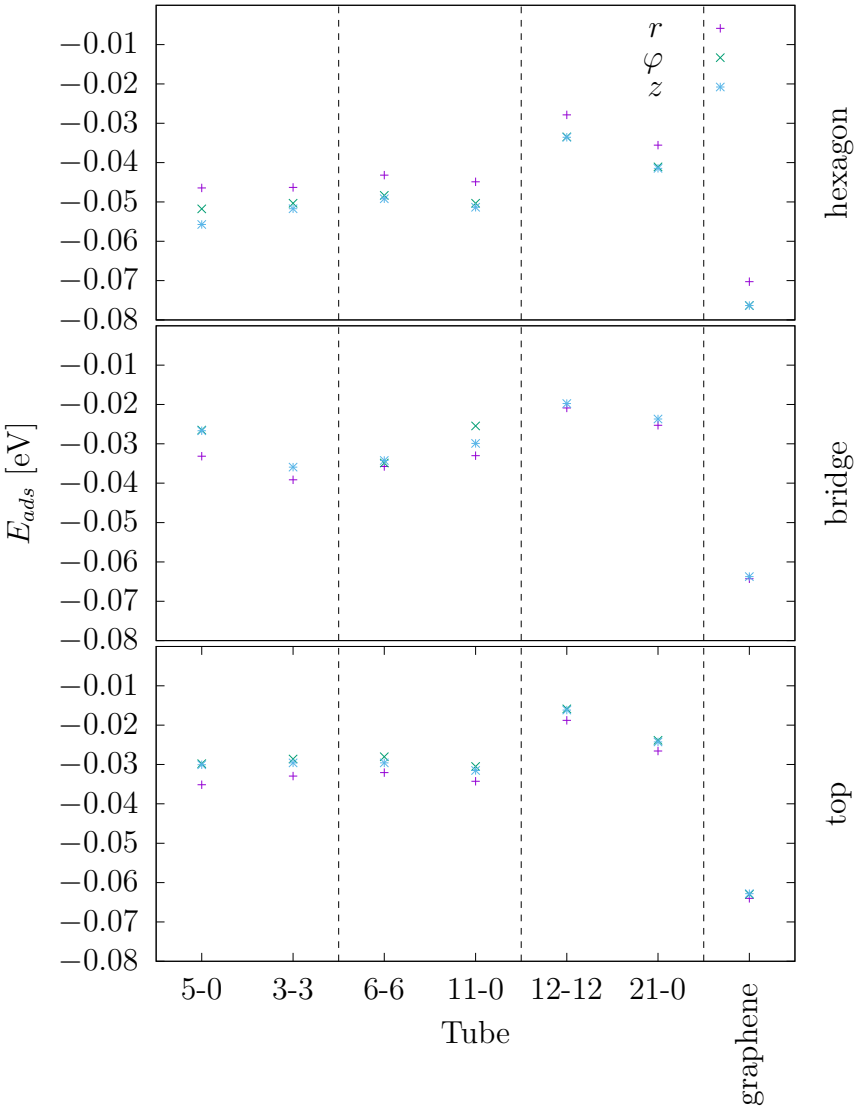

Figure 3.26: $E_{int,\mathrm{CNT+H_2}}$ for the r, φ and z alingments for all adsorption sites. The top panel shows *hexagon* the middle *bridge* and the bottom panel *top* position

For the adsorption energies of the different molecule configurations as shown in Fig. 3.26 and Tab. 3.9 no corresponding literature values could be found, at least not for the tube geometries used here. Qualitatively, our results tend to be in the same regime as experimental data (*98*, *99*) reporting values between 40 - 50 meV as well as calculated energies from different approaches (force-field) (*100*). Similarly, as reported for graphene, the molecular configuration at the hexagon site, where the H_2 axis is perpendicular (*hexagon-*z) or tangential (*hexagon-*φ) to the CNTs axis show again the lowest adsorption energies. All values in Tab. 3.9 are even less negative than the corresponding graphene values, but most importantly lie in the range between 16-56 meV which is one order of magnitude lower than the desired optimum value (estimated to be between 0.2 - 0.5 eV (*101*)).

Site	Alignment	Tube						
		5-0	3-3	6-6	11-0	12-12	21-0	Graphene
⌀[nm]		3.914	4.068	8.136	8.611	16.272	16.441	∞
Atoms in CNT		40	48	96	88	192	168	50
bridge	r	-0.033	-0.039	-0.036	-0.033	-0.021	-0.025	-0.064
	φ	-0.027	3.324	-0.035	-0.025	4.440	4.433	4.985
	z	-0.027	-0.036	-0.034	-0.030	-0.020	-0.024	-0.064
top	r	-0.035	-0.033	-0.032	-0.034	-0.019	-0.027	-0.064
	φ	-0.030	-0.029	-0.028	-0.030	-0.016	-0.024	-0.063
	z	-0.030	-0.030	-0.030	-0.032	-0.016	-0.024	-0.063
hexagon	r	-0.046	-0.046	-0.043	-0.045	-0.028	-0.036	-0.070
	φ	-0.052	-0.050	-0.048	-0.050	-0.033	-0.041	-0.076
	z	-0.056	-0.052	-0.049	-0.051	-0.034	-0.041	-0.076

Table 3.9: Adsorption energy E_{ads} for all considered molecule adsorption sites and alignments compared with corresponding configuration on graphene

3.4 Summary

This section summarizes the most important results of this thesis in brief. In the theoretical chapter the reader is comprehensively introduced to DFT and van-der-Waals correction to DFT. Moreover, the mathematical background of the atomic structure of SWCNT's is provided.

The result section starts with an extensive benchmark study of van-der-Waals correction methods applied to different carbon configurations (graphene, diamond, graphite). From this study we concluded to employ the TKATCHENKO-SCHÄFFLER dispersion correction method.

Interatomic potentials were calculated for the H_2 molecule, sp^2 and sp^3 bonded carbon. Furthermore, it was shown that common analytical pair potentials such as MOSRE, LENNARD-JONES or BUCKINGHAM do not provide a satisfactory description of those interactions.

The adsorption energies and heights were calculated for all high symmetry adsorption sites of graphene (*top*, *bridge*, and *hexagon*) and spatial molecule alignments (x, y and z). Our calculations suggest that the most favourable site is the *hexagon*, where especially *hexagon-x* and *hexagon-y* configurations are preferred by the H_2 molecule.

Additionally to the perfect graphene the potential surface of graphene supercells with a vacancy and a STONE-WALES defect were studied. Thus we could prove that these point defects have only short-ranged influence on the adsorption behaviour. For both defected supercells different hexagon sites were chosen to push the hydrogen through the graphene plane. The interaction energy versus distance curves revealed that the vacancy defect can possibly trap a hydrogen molecule, while a similar behaviour could not be observed for the STONE-WALES defect.

Finally, the adsoption energetics of the H_2 molecule configuration was studied for eight different SWCNTs (four *zigzag* and four *armchair*). In contrast to grahpene the *hexagon-r* configuration proved to be most favourable for CNTs. For the *hexagon-r* configuration, the interaction energy was calculated for six different SWCNT (three *zigzag* and three *armchair*) to study the influence of the CNT diameter on the adsorption behaviour. We could observe that all CNTs exhibit a smaller adsorption height and smaller adsorption energy. Moreover, CNTs with smaller diameter show a larger adsorption energy and smaller adsorption height than those with larger diameter.

Appendix A

Theoretical derivations

A.1 Self-consistent screening equation

The understanding of the TKATCHENKO-SCHÄFFLER method with the self consistent screening proved to be difficult. Exactly for this reason electric screening as well as the underlying mathematical conventions, such as interaction tensors are derived out in detail. The following derivations are adapted and taken from YAMAMOTO (*102*).

A.1.1 Charge-charge interaction

At first, one starts with the charge-charge interaction from classical electrodynamics. For a point charge at $\vec{r}_i$, the electrostatic potential is

$$\Phi(|\vec{r}-\vec{r}_i|)_C = \frac{Z_i e}{4\pi\epsilon_0}\frac{1}{|\vec{r}-\vec{r}_i|} \tag{A.1}$$

Therefore the electrostatic energy $E_{C\leftrightarrow C}$ for another point charge $Z_j e$ is given by

$$E_{C\leftrightarrow C} = Z_j e\Phi(|\vec{r}_j-\vec{r}_i|)_C = \frac{Z_i Z_j e^2}{4\pi\epsilon_0}\frac{1}{|\vec{r}_j-\vec{r}_i|} \tag{A.2}$$

A.1.2 Charge-dipole interaction

The charge dipole interaction can be approached in two ways. Either one thinks of an interaction of a charge with a dipole field, or one tries to describe the phenomenon as the interaction of a dipole with a charge field, where both lead, of course, to the same result. Consider a negative point charge at $\vec{r}_j$ interacting with a positive one at $\vec{r}_i$. Additionally, we add another point charge at point $\vec{r}_j + \vec{u}_j$ where $\vec{u}_j$ denotes the dipole axis. Since we are

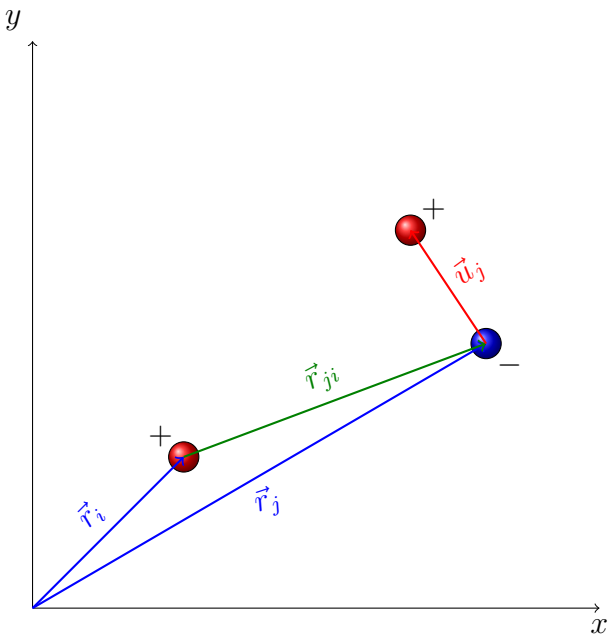

Figure A.1: Illustration of the charge-dipole interaction

studying long range phenomena, $|\vec{r}_j - \vec{r}_i| \gg \vec{u}_j$ holds true. If one has a closer look on Fig. A.1 it is obvious that the electrostatic energy term yields

$$E_{C\leftrightarrow D} = \frac{Z_i(-Z_j)e^2}{4\pi\epsilon_0}\frac{1}{|\vec{r}_j - \vec{r}_i|} + \frac{Z_i Z_j e^2}{4\pi\epsilon_0}\frac{1}{|\vec{r}_j + \vec{u}_j - \vec{r}_i|} \tag{A.3}$$

For convienience, following notations are introduced $\vec{r}_j - \vec{r}_i \equiv \vec{r}_{ji}$ and $|\vec{r}_j - \vec{r}_j| \equiv r_{ji}$, which allow to rewrite Eq. A.3 as

$$E_{C\leftrightarrow D} = -\frac{Z_i Z_j e^2}{4\pi\epsilon_0}\left[\frac{1}{r_{ij}} - \frac{1}{\sqrt{r_{ji}^2 + 2\vec{r}_{ji}\vec{u}_j + u_j^2}}\right] \tag{A.4}$$

By factorising and approximating the second term with binomial series of a form $(1+x)^\alpha = \sum_{k=0}^{\infty}\binom{\alpha}{k}x^k$, the equation above can be approximated to $(\alpha = -\frac{1}{2} \rightarrow (1+x)^{-\frac{1}{2}} \simeq 1 - \frac{x}{2} + \frac{3}{8}x^2 + \mathcal{O}(x^3))$

$$E_{C\leftrightarrow D} = -\frac{Z_i Z_j e^2}{4\pi\epsilon_0 r_{ji}} \left[1 - \frac{1}{\sqrt{1 + \frac{2\vec{r}_{ji}\vec{u}_j}{r_{ji}^2} + \frac{u_j^2}{r_{ij}^2}}} \right] \tag{A.5}$$

$$\simeq -\frac{Z_i Z_j e^2}{4\pi\epsilon_0 r_{ji}} \left[1 - 1 + \frac{1}{2}\frac{2\vec{r}_{ji}\vec{u}_j}{r_{ji}^2} + \frac{1}{2}\frac{u_j^2}{r_{ji}^2} - \frac{3}{8}\left(\frac{2\vec{r}_{ji}\vec{u}_j}{r_{ji}^2} + \frac{u_j^2}{r_{ji}^2} \right)^2 \right] \tag{A.6}$$

By neglecting small terms $|\vec{r}_j - \vec{r}_i| \gg \vec{u}_j$ one ends up with

$$E_{C\leftrightarrow D} = -\frac{Z_i Z_j e^2}{4\pi\epsilon_0}\frac{\vec{r}_{ji}\vec{u}_j}{r_{ji}^3} = \frac{Z_i Z_j e^2}{4\pi\epsilon_0} \tag{A.7}$$

Now let $\vec{p}_j$ be the electric dipole moment of the dipole j, which is by definition $\vec{p}_j \equiv Z_j e\vec{u}_j$. Therefore, for the electric field of the charge $\vec{E}_C^i$ at position $\vec{r}_i$ one obtains

$$E_{C\leftrightarrow D} = \vec{E}_C^i(\vec{r}_j)\vec{p}_j = \vec{E}_C^i(\vec{r}_j) Z_j e\vec{u}_j \Leftrightarrow \vec{E}_C^i(\vec{r}) = \frac{Z_i e}{4\pi\epsilon_0}\frac{\vec{r} - \vec{r}_i}{|\vec{r} - \vec{r}_i|^3} \tag{A.8}$$

A.1.3 Dipole-dipole interaction

The route to obtain an analytical formula for the dipole-diole is the same as before except for the enhancement that another charge is placed at position $\vec{r}_i + \vec{u}_i$ as illustrated in Fig. A.2. $\vec{u}_i$ and $\vec{u}_j$ denote the dipole axes of the dipoles i and j respectively.

Analogously as in the previous section one arrives at the following formula for the energy

$$E_{D\leftrightarrow D} = \frac{e^2}{4\pi\epsilon_0}\left[\frac{(-Z_i)(-Z_j)}{|\vec{r}_j - \vec{r}_i|} + \frac{(-Z_i)Z_j}{|\vec{r}_j + \vec{u}_j - \vec{r}_i|} + \frac{(-Z_j)Z_i}{|\vec{r}_j - \vec{u}_i - \vec{r}_i|} + \frac{Z_j Z_i}{|\vec{r}_j + \vec{u}_j - \vec{u}_i - \vec{r}_i|} \right] \tag{A.9}$$

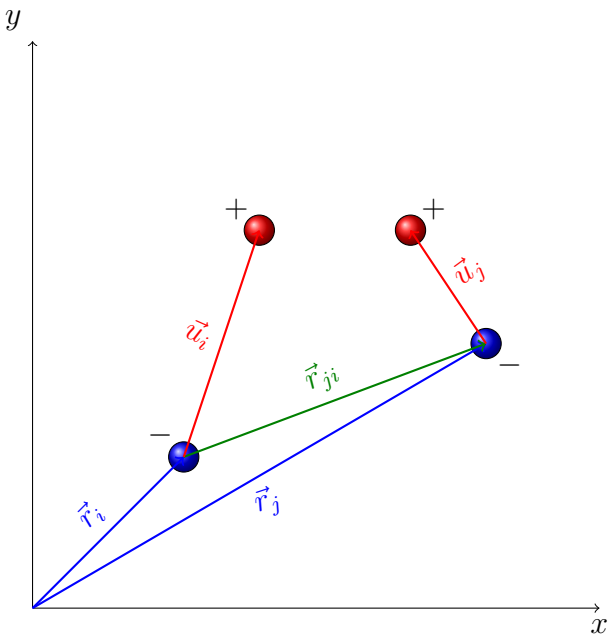

Figure A.2: Illustration of the dipole-dipole interaction

Rewriting Eq. A.9 (as done in with Eq. A.4 in Eq. A.6)

$$
\begin{aligned}
E_{D\leftrightarrow D} &= \frac{Z_i Z_j e^2}{4\pi\epsilon_0}\left[\frac{1}{r_{ji}} - \frac{1}{\sqrt{r_{ji}^2 + 2\vec{r}_{ji}\vec{u}_j + u_j^2}} - \frac{1}{\sqrt{r_{ji}^2 - 2\vec{r}_{ji}\vec{u}_i + u_i^2}}\right. \\
&\qquad \left. + \frac{1}{\sqrt{r_{ji}^2 - 2\vec{r}_{ji}\vec{u}_i + 2\vec{r}_{ji}\vec{u}_j - 2\vec{p}_i\vec{p}_j + u_j^2 + u_i^2 + p_j^2 + p_i^2}}\right] \\
&= \frac{Z_i Z_j e^2}{4\pi\epsilon_0 r_{ji}}\left[1 - \frac{1}{\sqrt{1 + \frac{2\vec{r}_{ji}\vec{u}_j}{r_{ji}^2} + \frac{u_j^2}{r_{ji}^2}}} - \frac{1}{\sqrt{1 - \frac{2\vec{r}_{ji}\vec{u}_i}{r_{ji}^2} + \frac{u_i^2}{r_{ji}^2}}}\right. \\
&\qquad \left. + \frac{1}{\sqrt{1 - \frac{2\vec{r}_{ji}\vec{u}_i}{r_{ji}^2} + \frac{2\vec{r}_{ji}\vec{u}_j}{r_{ji}^2} - \frac{2\vec{u}_i\vec{u}_j}{r_{ji}^2} + \frac{u_j^2}{r_{ji}^2} + \frac{u_i^2}{r_{ji}^2} + \frac{p_j^2}{r_{ji}^2} + \frac{p_i^2}{r_{ji}^2}}}\right]
\end{aligned}
\tag{A.10}
$$

Again expanding the equation into the binomial series leads to the following expression

$$\begin{aligned}
E_{D\leftrightarrow D} \simeq \frac{Z_i Z_j e^2}{4\pi\epsilon_0 r_{ij}} \Bigg[& 1 - 1 + \frac{1}{2}\frac{2\vec{r}_{ij}\vec{u}_j}{r_{ij}^2} + \frac{1}{2}\frac{u_j^2}{r_{ij}^2} - \frac{3}{8}\left(\frac{2\vec{r}_{ij}\vec{u}_j}{r_{ij}^2} + \frac{u_j^2}{r_{ij}^2}\right)^2 \\
& - 1 + \frac{1}{2}\frac{-2\vec{r}_{ij}\vec{u}_i}{r_{ij}^2} + \frac{1}{2}\frac{u_i^2}{r_{ij}^2} - \frac{3}{8}\left(\frac{-2\vec{r}_{ij}\vec{u}_i}{r_{ij}^2} + \frac{u_i^2}{r_{ij}^2}\right)^2 \\
& + 1 - \frac{1}{2}\frac{-2\vec{r}_{ij}\vec{u}_i}{r_{ij}^2} - \frac{1}{2}\frac{2\vec{r}_{ij}\vec{u}_j}{r_{ij}^2} - \frac{1}{2}\frac{u_i^2}{r_{ij}^2} - \frac{1}{2}\frac{u_j^2}{r_{ij}^2} + \frac{1}{2}\frac{2\vec{u}_i\vec{u}_j}{r_{ij}^2} \\
& + \frac{3}{8}\left(\frac{-2\vec{r}_{ij}\vec{u}_i}{r_{ij}^2} + \frac{-2\vec{r}_{ij}\vec{u}_j}{r_{ij}^2} + \frac{u_j^2}{r_{ij}^2} + \frac{u_i^2}{r_{ij}^2} - \frac{2\vec{u}_i\vec{u}_j}{r_{ij}^2}\right)^2 \Bigg] \\
= \frac{Z_i Z_j e^2}{4\pi\epsilon_0 r_{ij}^3} & \left[\vec{u}_i\vec{u}_j - 3\frac{(\vec{r}_{ij}\vec{u}_i)(\vec{r}_{ij}\vec{u}_j)}{r_{ij}^2}\right] \\
= \frac{1}{4\pi\epsilon_0 r_{ij}^3} & \left[\underbrace{Z_i e\vec{u}_i}_{\vec{p}_i}\underbrace{Z_i e\vec{u}_j}_{\vec{p}_j} - 3\frac{(\vec{r}_{ij}\overbrace{Z_i e\vec{u}_i}^{\vec{p}_i})(\vec{r}_{ij}\overbrace{Z_i e\vec{u}_j}^{\vec{p}_j})}{r_{ij}^2}\right] \\
= \frac{1}{4\pi\epsilon_0 r_{ij}^3} & \left[\vec{p}_i\vec{p}_j - 3\frac{(\vec{r}_{ij}\vec{p}_i)(\vec{r}_{ij}\vec{p}_j)}{r_{ij}^2}\right]
\end{aligned} \tag{A.11}$$

where $\vec{p}_i$ and $\vec{p}_j$ represent the corresponding dipole moments. Again, one continues to find electric $\vec{E}_D^i(\vec{r})$ field from i^{th} dipole the same way as in Eq. A.8 and thus obtains

$$\vec{E}_D^i(\vec{r}) = \frac{1}{4\pi\epsilon_0|\vec{r}-\vec{r}_i|^3}\left[\vec{p}_i - 3\frac{\vec{p}_i(\vec{r}-\vec{r}_i)(\vec{r}-\vec{r}_i)}{|\vec{r}-\vec{r}_i|^2}\right] \tag{A.12}$$

A.1.4 Mathematical unified description

For convenience in mathematical notation, let $q_i = eZ_i$ be the charge of the i^{th} dipole and $\vec{p}_i = (p_{ix}, p_{iy}, p_{iz})$ again the corresponding dipole momentum. Now consider a general system built up by N dipoles. The total energy can be written as

$$\begin{aligned}
4\pi\epsilon_0 E_{tot} = \sum_i^N \sum_{j>i}^N \Bigg(& \underbrace{q_i r_{ij}^{-1} q_j}_{C\leftrightarrow C} - \underbrace{q_i r_{ij}^{-3}\left[r_{ij,x}p_{jx} + r_{ij,y}p_{jy} + r_{ij,z}p_{jz}\right]}_{C\leftrightarrow D} + \underbrace{q_j r_{ij}^{-3}\left[r_{ij,x}p_{ix} + r_{ij,y}p_{iy} + r_{ij,z}p_{iz}\right]}_{D\leftrightarrow C} \\
& + \underbrace{r_{ij}^{-5}\left[3p_{ix}r_{ij,x}^2 p_{jx} + \ldots + 3p_{ix}r_{ij,x}r_{ij,y}p_{jy} + \ldots - 3r_{ij}^2\right]}_{D\leftrightarrow D}\Bigg)
\end{aligned} \tag{A.13}$$

However, this can be done much smarter using interaction tensors. Therefore let $\mathcal{T}_{ij}$ be the *interaction tensor* and $\nabla_\alpha = \dfrac{\partial}{\partial r_{ij,\alpha}}$ where $\alpha = \{x, y, z\}$ represent the spatial direction. Now by defining $\mathcal{T}_{ij}$ as

$$\mathcal{T}_{ij} = \frac{1}{r_{ij}} \tag{A.14}$$

$$\mathcal{T}_{ij}^{\alpha} = \nabla_\alpha \mathcal{T}_{ij} = -r_{ij,\alpha} r_{ij}^{-3} \tag{A.15}$$

$$\mathcal{T}_{ij}^{\alpha\beta} = \nabla_\alpha \otimes \nabla_\beta \mathcal{T}_{ij} = (3 r_{ij,\alpha} r_{ij,\beta} - r_{ij}^2 \delta_{\alpha\beta}) r_{ij}^{-5} \tag{A.16}$$

$$\mathcal{T}_{ij}^{\alpha\beta\gamma} = \nabla_\alpha \otimes (\nabla_\beta \otimes \nabla_\gamma \mathcal{T}_{ij}) = -\left[15 r_{ij,\alpha} r_{ij,\beta} r_{ij,\gamma} - 3 r_{ij}^2 (r_{ij,\alpha}\delta_{\gamma\beta} + r_{ij,\beta}\delta_{\alpha\gamma} + r_{ij,\gamma}\delta_{\beta\alpha})\right] r_{ij}^{-7} \tag{A.17}$$

Eq. A.13 can be simplified to

$$4\pi\epsilon_0 E_{tot} = \sum_{i}^{N} \sum_{j>i}^{N} \left(\underbrace{q_i \mathcal{T}_{ij} q_j}_{C\leftrightarrow C} - \underbrace{q_i \sum_{\alpha} \mathcal{T}_{ij}^{\alpha} p_{j,\alpha}}_{C\leftrightarrow D} + \underbrace{\sum_{\alpha} p_{i,\alpha} \mathcal{T}_{ij}^{\alpha} q_j}_{D\leftrightarrow C} - \underbrace{\sum_{\alpha}\sum_{\beta} p_{i,\alpha} \mathcal{T}_{ij}^{\alpha\beta} p_{j,\beta}}_{D\leftrightarrow D} \right) \tag{A.18}$$

A.1.5 Polarization

After having introduced all neccessary mathematical notations, we consider an atom i in a solid. The electric field $\vec{E}(\vec{r}_i)$ can be represented as the sum of the electric fields of the other charges $\vec{E}_C^j$ plus the electric field of the other dipoles $\vec{E}_D^j$

$$\vec{E}(\vec{r}_i) = \sum_{i\neq j} \vec{E}_C^j(\vec{r}_i) + \vec{E}_D^j(\vec{r}_i). \tag{A.19}$$

Furthermore, the dipole moment for a certain direction of the atom under consideration can be denoted as

$$p_{i,\alpha} = p_{i,\alpha}^{static} + p_{i,\alpha}^{ind} \simeq p_{i,\alpha}^{ind} \tag{A.20}$$

since one assumes $p_{i,\alpha}^{static} \approx 0$. By applying the knowledge from the previous sections, the electric field expands to

$$\vec{E}(\vec{r}_i) = \frac{1}{4\pi\epsilon_0}\sum_{i\neq j}\left(Z_j e\frac{\vec{r}_i-\vec{r}_j}{|\vec{r}_i-\vec{r}_j|^3} - \frac{1}{|\vec{r}_i-\vec{r}_j|^3}\left[\vec{p}_i - 3\frac{\vec{p}_i(\vec{r}_i-\vec{r}_j)(\vec{r}_i-\vec{r}_j)}{|\vec{r}_i-\vec{r}_j|^2}\right]\right) \tag{A.21}$$

$$= \frac{1}{4\pi\epsilon_0}\sum_{i\neq j}\sum_{\alpha}\left(-\mathcal{T}^{\alpha}_{ij}q_j + \sum_{\beta}\mathcal{T}^{\alpha\beta}_{ij}p^{ind}_{j,\beta}\right). \tag{A.22}$$

Now, the polarizability of an atom is defined as $\vec{p} = \alpha\vec{E}$ where $\vec{p}$ is the dipole moment, α the polarizability and $\vec{E}$ the electric field. Since we deal with vector quantities, the relation is

$$\vec{p}^{\,\mathrm{ind}}_i = (\alpha_i \mathbf{1})\vec{E}_i \tag{A.23}$$

where $\mathbf{1}$ represents the unity matrix and α_i the polarizability of the i^{th} atom. Finally, one arrives at the *self-consistent screening* equation by putting Eq. A.22 and Eq. A.23 together

$$p^{ind}_{i,\alpha} = \frac{\alpha_i}{4\pi\epsilon_0}\sum_{i\neq q}\left(-\mathcal{T}^{\alpha}_{ij}q_j + \sum_{\beta}\mathcal{T}^{\alpha\beta}_{ij}p^{ind}_{j,\beta}\right). \tag{A.24}$$

A.2 Superposition of charge densities

Since DFT codes calculate the real space distribution of charge density , codes like VASP can also start a calculation with a given pre-converged charge density which may significantly reduce the time a calculation needs. This is especially significant for big systems, such as the 21-0 nanotubes. Therefore, it is senseful to create routines to add up charge densities from different systems.

A.2.1 Coordinate transformation

Consider a system with periodic boundary conditions with lattice parameters a, b, c, α, β and γ (blue) with a charge density $\rho(\vec{r})$ to which the charge density $\rho'(\vec{r})$ of a second system with lattice parameters a', b', c', α', β' and γ' (red) should be added, as shown in Fig. A.3. However, the charge density is only given at the points of a regular discrete mesh. The amount of points in each direction is given by VASP's FFT grid parameters `NGX`, `NGY` and `NGZ`.

Thus all the fractional coordinates at which a value of the charge density is given for the cells are therefore

$$\vec{x}_{ijk}^{\text{frac}} = \left\{ \left[\frac{i}{\texttt{NGX}}, \frac{j}{\texttt{NGY}}, \frac{k}{\texttt{NGZ}} \right] \middle| \, i \in \{0, \ldots \texttt{NGX}\} \text{ and } j \in \{0, \ldots, \texttt{NGY}\} \text{ and } k \in \{0, \ldots, \texttt{NGZ}\} \right\}. \tag{A.25}$$

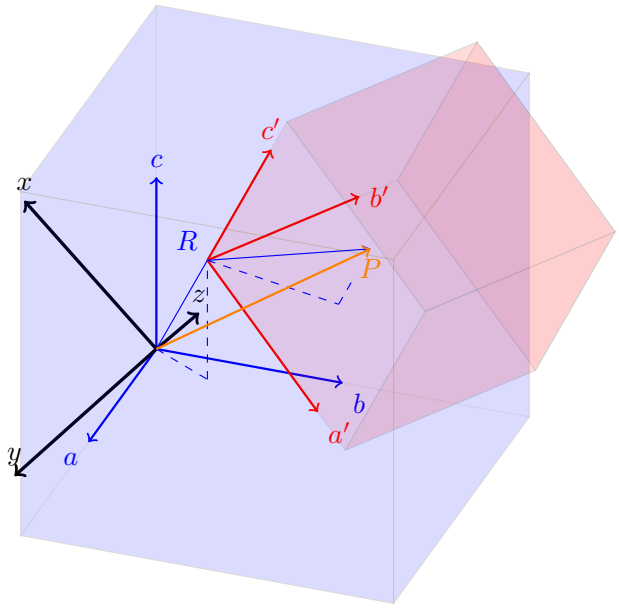

Figure A.3: Schematic setup for adding the charge densities of two simulation cells

To convert this fractional coordinates to the global cartesian coordinates, a conversion matrix must be applied

$$\begin{aligned} \vec{x}_{ijk}^{\text{cart}} &= \mathbf{G} \cdot \vec{x}_{ijk}^{\text{frac}} \\ \mathbf{G} &= \begin{bmatrix} a & b\cos(\gamma) & c\cos(\beta) \\ 0 & b\sin(\gamma) & \frac{c}{\sin(\gamma)}\left(\cos(\alpha) - \cos(\beta)\cos(\gamma)\right) \\ 0 & 0 & \frac{V}{ab\sin(\gamma)} \end{bmatrix} \\ V &= abc\sqrt{1 - \cos^2(\alpha) + 2\cos(\alpha)\cos(\beta)\cos(\gamma) - \cos^2(\beta) - \cos^2(\gamma)} \end{aligned} \tag{A.26}$$

where V is the volume of the unit cell and $\mathbf{G}$ the conversion matrix(*103*, *104*). The orientation relationship between the two charge densities is specified by an arbitrary point $\vec{P}$ from

which the fractional coordinates in both systems $\vec{P}^{\text{frac}}$ and $\vec{P}'^{,\text{frac}}$ are known. Consequently the translation vector between the two coordinate systems $\vec{T}$ can be computed by

$$\vec{T} = \mathbf{G} \cdot \vec{P}^{\text{frac}} - \mathbf{G}' \cdot \vec{P}'^{,\text{frac}}. \tag{A.27}$$

However, additionally to uniquely specify any arbitrary geometrical relationship, the three EULER tilt angles ϕ, χ and ψ need to be specified. In the following section a simple way to find those is given.

A.2.2 Finding rotation angles between two systems

To find a rotation matrix between two vectors the RODRIGUES' rotation formula is employed (*105*). Assuming that a given unit vector $\vec{u}$ is known and given in the global coordinates. The task it to map it onto a different unit vector $\vec{v}$. Therefore, a rotation matrix $\mathbf{R}$ can be constructed as

$$\begin{aligned} \mathbf{R} &= \mathbf{1} + \mathbf{A} + (\mathbf{A} \cdot \mathbf{A}) \cdot \frac{1 - \vec{u} \cdot \vec{v}}{||\vec{u} \times \vec{v}||^2} \\ \vec{k} &= \vec{u} \times \vec{v} \\ \mathbf{A} &= \begin{bmatrix} 0 & -k_3 & k_2 \\ k_3 & 0 & -k_1 \\ -k_2 & k_1 & 0 \end{bmatrix} \end{aligned} \tag{A.28}$$

Furthermore, we know that the rotation matrix for any arbitrary EULER angles is

$$\tilde{\mathbf{R}} = \begin{bmatrix} \cos(\chi)\cos(\psi) & \sin(\phi)\sin(\chi)\cos(\psi) - \sin(\psi)\cos(\phi) & \sin(\phi)\sin(\psi) + \sin(\chi)\cos(\phi)\cos(\psi) \\ \sin(\psi)\cos(\chi) & \sin(\phi)\sin(\chi)\sin(\psi) + \cos(\phi)\cos(\psi) & -\sin(\phi)\cos(\psi) + \sin(\chi)\sin(\psi)\cos(\phi) \\ -\sin(\chi) & \sin(\phi)\cos(\chi) & \cos(\phi)\cos(\chi) \end{bmatrix} \tag{A.29}$$

By simply solving $\mathbf{R} = \tilde{\mathbf{R}}$ the corresponding EULER angles ϕ, χ and ψ as illustrated in Fig. A.4 can be found.

Now, since the exact orientation angles between the two coordinate systems are known the charge densities can be added up. At first a regular grid interpolator with nearest neighbor interpolation (*82*) constructs a continous function $\rho(\vec{x})'_{\text{int}}$ for all datapoints $\vec{x}'^{,\text{frac}}_{ijk}$

(red box). All values $\vec{x}_{ijk}^{\text{frac}}$ must be transformed into the fractional coordinates of the target cell (red) which is done with the following transformation rule

$$\vec{x}_{ijk}^{\text{trans}} = \mathbf{G}'^{-1} \cdot \underbrace{(\mathbf{R} \cdot (\overbrace{\mathbf{G} \cdot \vec{x}_{ijk}^{\text{frac}} - \vec{P}^{\text{frac}}}^{\text{tranlation to P}}))}_{\text{rotation)}} \tag{A.30}$$

where $\mathbf{G}'^{-1}$ is the conversion matrix which transforms cartesian to fractional coordinates. Plugging all values of $\vec{x}_{ijk}^{\text{trans}}$ into the interpolated charge density $\rho'(\vec{x})_{\text{int}}$ will yield the desired charge densities which can than be added to the intitial discrete set of charge densities (blue box). Thus we arrive at the final result

$$\rho(\vec{x})^{\text{added}} = \underbrace{\rho(\vec{x}_{ijk}^{\text{frac}})}_{\text{initial charge density values (blue)}} + \underbrace{\rho'(\vec{x}_{ijk}^{\text{trans}})_{\text{int}}}_{\text{int. charge density}} \tag{A.31}$$

For all $\vec{x}_{ijk}^{\text{trans}}$ which are outside of the (red) cell, 0 was used as a default fill value. Alternatively periodic boundary conditions could be applied.

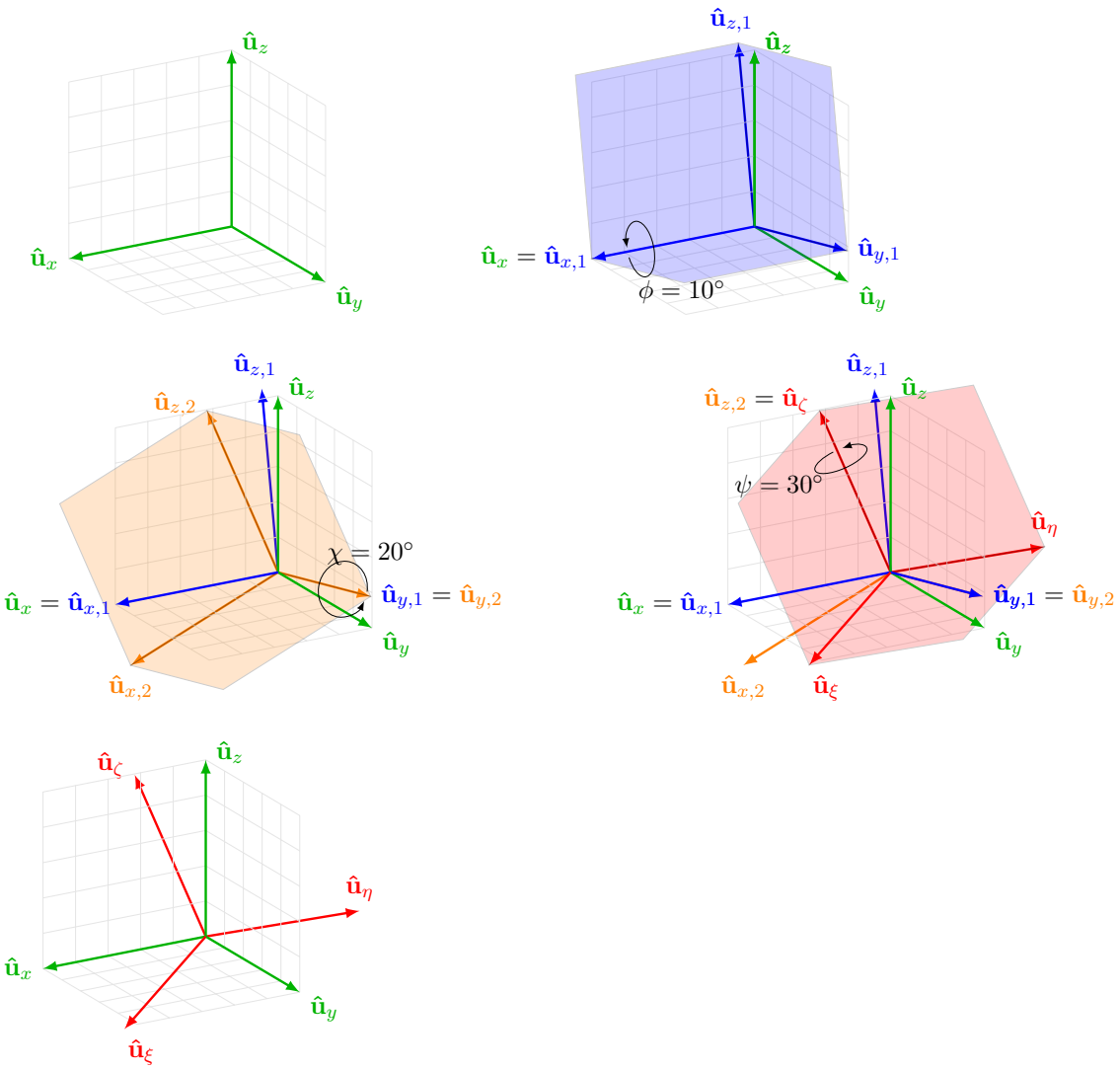

Figure A.4: The rotation matrix $\tilde{\vec{r}}$ (Eq. A.29) represents three chained rotations. ϕ around x-axis, χ around y-axis and ψ around z-axis. $\tilde{\mathbf{R}} = \vec{R}_x(\phi) \cdot \mathbf{R}_y(\chi) \cdot \mathbf{R}_z(\psi)$

List of Figures

List of Tables

Bibliography

1. Y.-H. P. Zhang, B. R. Evans, J. R. Mielenz, R. C. Hopkins, M. W. Adams, *PLoS ONE* **2**, ed. by A. Melis, e456 (May 2007) (cit. on p. 1).
2. Y. Yan *et al.*, *Chemical Communications*, 1025 (2009) (cit. on p. 1).
3. S. S. Hla, M. D. Dolan, *IOP Conference Series: Materials Science and Engineering* **297**, 012027 (Jan. 2018) (cit. on p. 2).
4. A. K. Geim, K. S. Novoselov, *Nature Materials* **6**, 183–191 (Mar. 2007) (cit. on pp. 2, 3).
5. M. Sevilla, R. Mokaya, *Energy Environ. Sci.* **7**, 1250–1280 (2014) (cit. on p. 2).
6. T. S. Blankenship, R. Mokaya, *Energy & Environmental Science* **10**, 2552–2562 (2017) (cit. on p. 2).
7. T. S. B. II, N. Balahmar, R. Mokaya, *Nature Communications* **8**, `https://doi.org/10.1038/s41467-017-01633-x` (Nov. 2017) (cit. on p. 2).
8. D. B. Boyd, Z. Slanina, *Journal of Molecular Graphics and Modelling* **19**, 181–184 (Apr. 2001) (cit. on p. 3).
9. H. W. Kroto, J. R. Heath, S. C. O'Brien, R. F. Curl, R. E. Smalley, *Nature* **318**, pages (Nov. 14, 1985) (cit. on pp. 3, 4).
10. N. D. Mermin, H. Wagner, *Physical Review Letters* **17**, 1133–1136 (Nov. 1966) (cit. on p. 3).
11. A. Fasolino, J. H. Los, M. I. Katsnelson, *Nature Materials* **6**, 858–861 (Sept. 2007) (cit. on p. 3).
12. K. S. Novoselov, *Science* **306**, 666–669 (Oct. 2004) (cit. on p. 3).
13. C. Lee, X. Wei, J. W. Kysar, J. Hone, *Science* **321**, 385–388 (July 2008) (cit. on p. 3).
14. A. H. C. Neto, F. Guinea, N. M. R. Peres, K. S. Novoselov, A. K. Geim, *Reviews of Modern Physics* **81**, 109–162 (Jan. 2009) (cit. on p. 3).

15. Z. Zhu, Q. Zheng, Z. Wang, Z. Tang, W. Chen, *International Journal of Hydrogen Energy* **42**, 18465–18472 (July 2017) (cit. on p. 3).

16. E. Rangel, E. Sansores, *International Journal of Hydrogen Energy* **39**, 6558–6566 (Apr. 2014) (cit. on p. 3).

17. I. A. Baburin, A. Klechikov, G. Mercier, A. Talyzin, G. Seifert, *International Journal of Hydrogen Energy* **40**, 6594–6599 (June 2015) (cit. on p. 3).

18. I. K. Petrushenko, K. B. Petrushenko, *International Journal of Hydrogen Energy* **43**, 801–808 (Jan. 2018) (cit. on p. 3).

19. S. Iijima, *Nature* **354**, pages (Nov. 7, 1991) (cit. on p. 4).

20. S. Ghosh, V. Padmanabhan, *Diamond and Related Materials* **59**, 47–53 (Oct. 2015) (cit. on p. 4).

21. Z. Zhou *et al.*, *The Journal of Physical Chemistry B* **110**, 13363–13369 (July 2006) (cit. on pp. 4, 62).

22. M. Rubes, O. Bludsky, *ChemPhysChem* **10**, 1868–1873 (Aug. 2009) (cit. on pp. 4, 42).

23. S. Krishnan, R. Vadapoo, K. E. Riley, J. P. Velev, *Physical Review B* **84**, `https://doi.org/10.1103/physrevb.84.165408` (Oct. 2011) (cit. on pp. 4, 42, 62).

24. M. D. Ganji, S. M. Hosseini-khah, Z. Amini-tabar, *Physical Chemistry Chemical Physics* **17**, 2504–2511 (2015) (cit. on pp. 4, 42).

25. M. Dresselhaus, G. Dresselhaus, P. Eklund, in *Science of Fullerenes and Carbon Nanotubes* (Elsevier, 1996), pp. 756–869, `https://doi.org/10.1016/b978-012221820-0/50019-8` (cit. on pp. 5, 6).

26. C. Teichert, *Skriptum zur Vorlesung Halbleiterwerkstoffe*, 2016 (cit. on p. 5).

27. K. Burke, *The ABC of DFT, http://dft.uci.edu/book/gamma/g1.pdf*, `http://dft.uci.edu/book/gamma/g1.pdf` (cit. on p. 8).

28. M. Born, R. Oppenheimer, *Annalen der Physik* **389**, 457–484 (1927) (cit. on p. 9).

29. W. Ritz, *Journal für die reine und angewandte Mathematik* **135**, 1–61 (1908) (cit. on p. 9).

30. V. Fock, *Zeitschrift für Physik A Hadrons and Nuclei* **61**, 126–148 (Jan. 1930) (cit. on p. 9).

31. L. H. Thomas, *Mathematical Proceedings of the Cambridge Philosophical Society* **23**, 542–548 (1927) (cit. on p. 9).

32. P. Hohenberg, W. Kohn, *Phys. Rev.* **136**, B864–B871 (3B Nov. 1964) (cit. on p. 10).

33. H. Toffoli, *Lecture notes on Hohenberg-Kohn theorems*, 2012 (cit. on p. 10).

34. W. Kohn, L. J. Sham, *Phys. Rev.* **140**, A1133–A1138 (4A Nov. 1965) (cit. on pp. 12, 14).

35. R. Stowasser, R. Hoffmann, *Journal of the American Chemical Society* **121**, 3414–3420 (Apr. 1999) (cit. on p. 12).

36. J. C. Slater, *Phys. Rev.* **81**, 385–390 (3 Feb. 1951) (cit. on p. 12).

37. P. A. M. Dirac, *Mathematical Proceedings of the Cambridge Philosophical Society* **26**, 376 (July 1930) (cit. on p. 14).

38. E. Wigner, *Physical Review* **46**, 1002–1011, ISSN: 0031899X (1934) (cit. on p. 14).

39. M. Gell-Mann, K. A. Brueckner, *Physical Review* **106**, 364–368, ISSN: 0031899X (1957) (cit. on p. 14).

40. J. Hubbard, *Proceedings of the Royal Society A: Mathematical, Physical and Engineering Sciences* **244**, 199–211, ISSN: 1364-5021 (1958) (cit. on p. 14).

41. J. P. Perdew, A. Zunger, *Physical Review B* **23**, 5048–5079, ISSN: 0163-1829 (1981) (cit. on p. 14).

42. J. P. Perdew, *Electronic Structure of Solids*, 11–20 (1991) (cit. on p. 15).

43. J. P. Perdew, K. A. Jackson, M. R. Pederson, D. J. Singh, C. Fiolhais, *Physical Review B* **46**, 6671, ISSN: 0163-1829 (1992) (cit. on p. 15).

44. A. D. Becke, *The Journal of Chemical Physics* **38**, 3098–3100, ISSN: 00219606 (1988) (cit. on p. 15).

45. J. P. Perdew, M. Ernzerhof, K. Burke, *Physical Review Letters* **77**, 3865–3868, ISSN: 10797114 (1996) (cit. on pp. 15, 25).

46. J. P. Perdew, K. Burke, M. Ernzerhof, *Physical Review Letters* **78**, 1396, ISSN: 0031-9007 (1997) (cit. on p. 15).

47. S. Grimme, *Journal of Computational Chemistry* **25**, 1463–1473, ISSN: 01928651 (2004) (cit. on p. 16).

48. F. London, *Zeitschrift für Physik* **63**, 245–279, ISSN: 0044-3328 (Mar. 1, 1930) (cit. on p. 16).

49. Y. Liu, W. A. I. Goddard, *Materials Transactions* **50**, 1664–1670 (2009) (cit. on p. 16).

50. Q. Wu, W. Yang, *The Journal of Chemical Physics* **116**, https://doi.org/10.1063/1.1424928 (2002) (cit. on p. 16).

51. S. Grimme, *Journal of computational chemistry* **30**, 1545–1614, ISSN: 1096-987X (2009) (cit. on pp. 16, 17).

52. J. D. Chai, M. Head-Gordon, *Physical Chemistry Chemical Physics* **10**, 6615–6620, ISSN: 14639076 (2008) (cit. on p. 17).

53. S. Grimme, J. Antony, S. Ehrlich, H. Krieg, *Journal of Chemical Physics* **132**, ISSN: 00219606, arXiv: 0405167 (cond-mat) (2010) (cit. on pp. 17, 18).

54. J. Muto, *Proceedings of the Physico-Mathematical Society of Japan* **17**, 629 (June 1943) (cit. on p. 18).

55. B. M. Axilrod, E. Teller, *The Journal of Chemical Physics* **11**, 299–300 (June 1943) (cit. on p. 18).

56. M. Lein, J. F. Dobson, E. K. U. Gross, *Journal of Computational Chemistry* **20**, 12–22, ISSN: 1096-987X (1999) (cit. on p. 18).

57. A. J. Thakkar, H. Hettema, P. E. Wormer, *The Journal of Chemical Physics* **97**, 3252–3257, ISSN: 00219606 (1992) (cit. on p. 18).

58. G. Starkschall, R. G. Gordon, *The Journal of Chemical Physics* **56**, 2801–2806, ISSN: 0021-9606 (1972) (cit. on p. 18).

59. A. Tkatchenko, M. Scheffler, *Physical Review Letters* **102**, 6–9, ISSN: 00319007 (2009) (cit. on pp. 18, 21).

60. H. B. G. Casimir, D. Polder, *Phys. Rev.* **73**, 360–372 (4 Feb. 1948) (cit. on p. 19).

61. X. Chu, A. Dalgarno, *The Journal of Chemical Physics* **121**, 4083–4088 (Sept. 2004) (cit. on p. 19).

62. T. Brinck, J. S. Murray, P. Politzer, *The Journal of Chemical Physics* **98**, 4305–4306, ISSN: 00219606 (1993) (cit. on p. 19).

63. F. L. Hirshfeld, *Theoretica chimica acta* **44**, 129–138, ISSN: 1432-2234 (June 1, 1977) (cit. on p. 20).

64. T. Bučko, S. Lebègue, J. Hafner, J. G. Ángyán, *Journal of Chemical Theory and Computation* **9**, 4293–4299, ISSN: 15499618 (2013) (cit. on p. 22).

65. T. Bučko, S. Lebègue, J. G. Ángyán, J. Hafner, *Journal of Chemical Physics* **141**, ISSN: 00219606 (2014) (cit. on p. 22).

66. A. Tkatchenko, R. A. Distasio, R. Car, M. Scheffler, *Physical Review Letters* **108**, 1–5, ISSN: 00319007 (2012) (cit. on p. 22).

67. G. Kresse, J. Furthmüller, M. Marsman, *VASP the GUIDE*, `http://cms.mpi.univie.ac.at/vasp/vasp.pdf` (cit. on pp. 22, 23).

68. A. D. Becke, E. R. Johnson, *The Journal of Chemical Physics* **127**, 154108 (Oct. 2007) (cit. on p. 23).

69. A. D. Becke, E. R. Johnson, *The Journal of Chemical Physics* **124**, 014104 (Jan. 2006) (cit. on p. 23).

70. A. D. Becke, E. R. Johnson, *The Journal of Chemical Physics* **123**, 154101 (Oct. 2005) (cit. on p. 23).

71. S. N. Steinmann, C. Corminboeuf, *The Journal of Chemical Physics* **134**, 044117 (Jan. 2011) (cit. on p. 23).

72. S. N. Steinmann, C. Corminboeuf, *Journal of Chemical Theory and Computation* **7**, 3567–3577 (Nov. 2011) (cit. on p. 23).

73. K. T. Tang, J. P. Toennies, *The Journal of Chemical Physics* **80**, 3726–3741 (Apr. 1984) (cit. on p. 23).

74. H.-J. Böhm, R. Ahlrichs, *The Journal of Chemical Physics* **77**, 2028–2034 (Aug. 1982) (cit. on p. 23).

75. É. Brémond, N. Golubev, S. N. Steinmann, C. Corminboeuf, *The Journal of Chemical Physics* **140**, 18A516 (May 2014) (cit. on p. 24).

76. S. Gautier, S. N. Steinmann, C. Michel, P. Fleurat-Lessard, P. Sautet, *Physical Chemistry Chemical Physics* **17**, 28921–28930 (2015) (cit. on p. 24).

77. G. Kresse, J. Hafner, *Phys. Rev. B* **47**, 558–561 (1 Jan. 1993) (cit. on p. 25).

78. G. Kresse, J. Furthmüller, *Phys. Rev. B* **54**, 11169–11186 (16 Oct. 1996) (cit. on p. 25).

79. G. Kresse, D. Joubert, *Phys. Rev. B* **59**, 1758–1775 (3 Jan. 1999) (cit. on p. 25).

80. H. J. Monkhorst, J. D. Pack, *Phys. Rev. B* **13**, 5188–5192 (12 June 1976) (cit. on p. 25).

81. A. Jain *et al.*, *APL Materials* **1**, 011002, ISSN: 2166532X (2013) (cit. on p. 26).

82. E. Jones, T. Oliphant, P. Peterson, *et al.*, *SciPy: Open source scientific tools for Python*, [Online; accessed ¡today¿], 2001–, `http://www.scipy.org/` (cit. on pp. 26, 76).

83. S. P. Ong *et al.*, *Computational Materials Science* **68**, 314–319, ISSN: 0927-0256 (2013) (cit. on p. 26).

84. K. Momma, F. Izumi, *Journal of Applied Crystallography* **44**, 1272–1276 (Dec. 2011) (cit. on p. 26).

85. J. Lennard-Jones, *Proceedings of the Royal Society of London A: Mathematical, Physical and Engineering Sciences* **106**, 463–477, ISSN: 0950-1207 (1924) (cit. on p. 27).

86. R. Buckingham, *Proceedings of the Royal Society of London A: Mathematical, Physical and Engineering Sciences* **168**, 264–283, ISSN: 0080-4630 (1938) (cit. on p. 29).

87. P. M. Morse, *Physical Review* **34**, 57–64 (July 1929) (cit. on p. 29).

88. Y. Okamoto, Y. Miyamoto, *The Journal of Physical Chemistry B* **105**, 3470–3474 (May 2001) (cit. on p. 42).

89. V. Tozzini, V. Pellegrini, *The Journal of Physical Chemistry C* **115**, 25523–25528 (Dec. 2011) (cit. on p. 42).

90. S. Patchkovskii *et al.*, *Proceedings of the National Academy of Sciences* **102**, 10439–10444 (July 2005) (cit. on p. 42).

91. L. Van Winkle, *Interpolating in a Triangle* (2016; `https://codeplea.com/triangular-interpolation`) (cit. on p. 44).

92. A. Stone, D. Wales, *Chemical Physics Letters* **128**, 501–503 (Aug. 1986) (cit. on p. 52).

93. P. Thrower, *Chemistry and Physics of Carbon* **5**, 217–320 (1969) (cit. on p. 52).

94. T. Björkman *et al.*, *Scientific Reports* **3**, `https://doi.org/10.1038/srep03482` (Dec. 2013) (cit. on p. 52).

95. J. Kotakoski *et al.*, *Physical Review B* **83**, `https://doi.org/10.1103/physrevb.83.245420` (June 2011) (cit. on p. 52).

96. J. S. Arellano, L. M. Molina, A. Rubio, M. J. López, J. A. Alonso, *The Journal of Chemical Physics* **117**, 2281–2288 (Aug. 2002) (cit. on pp. 62, 65).

97. S. S. Han, H. M. Lee, *Carbon* **42**, 2169–2177, ISSN: 00086223 (2004) (cit. on pp. 62, 65).

98. G. Vidali, G. Ihm, H.-Y. Kim, M. W. Cole, *Surface Science Reports* **12**, 135–181 (Jan. 1991) (cit. on p. 66).

99. H. Schimmel *et al.*, *Materials Science and Engineering B* **108**, 124–129 (Apr. 2004) (cit. on p. 66).

100. M. K. Kostov, H. Cheng, A. C. Cooper, G. P. Pez, *Physical Review Letters* **89**, https://doi.org/10.1103/physrevlett.89.146105 (Sept. 2002) (cit. on p. 66).

101. A. Chambers, C. Park, R. T. K. Baker, N. M. Rodriguez, *The Journal of Physical Chemistry B* **102**, 4253–4256 (May 1998) (cit. on p. 66).

102. M. Yamamoto, *Lecture notes on charge-charge, charge-dipole, dipole-charge, dipole-dipole interaction*, Dec. 2008 (cit. on p. 68).

103. B. Rupp, *Coordinate system transformation* (2016; http://www.ruppweb.org/Xray/tutorial/Coordinate%20system%20transformation.htm) (cit. on p. 75).

104. CCDC, *Mercury manual* (2016; https://web.archive.org/web/20081004101125/http://www.ccdc.cam.ac.uk/support/documentation/mercury_csd/portable/mercury_portable-4-70.html) (cit. on p. 75).

105. J. E. Mebius, 1–7 (2007) (cit. on p. 76).